Spring 2001

Coherent Differential Absorption Lidar for Combined Measurement of Wind and Trace Atmospheric Gases

Grady James Koch
Old Dominion University

COHERENT DIFFERENTIAL ABSORPTION LIDAR FOR COMBINED MEASUREMENT OF WIND AND TRACE ATMOSPHERIC GASES

by

Grady James Koch
B.S. May 1991, Virginia Polytechnic Institute and State University
M.S. January 1995, University of Illinois at Urbana-Champaign

A Dissertation submitted to the Faculty of
Old Dominion University in Partial Fulfillment of the
Requirements for the Degree of

DOCTOR OF PHILOSOPHY

ELECTRICAL AND COMPUTER ENGINEERING

OLD DOMINION UNIVERSITY
May 2001

Approved by:

_____
Amin N. Dharamsi (Director)

_____
Carl Holden (Member)

_____
Ravindra P. Joshi (Member)

_____
Karl H. Schoenbach (Member)

ABSTRACT

COHERENT DIFFERENTIAL ABSORPTION LIDAR FOR COMBINED MEASUREMENT OF WIND AND TRACE ATMOSPHERIC GASES

Grady James Koch
Old Dominion University, 2001
Director: Dr. Amin N. Dharamsi

A lidar system was developed for making combined range-resolved measurements of wind speed and direction, water vapor concentration, and carbon dioxide concentration in the atmosphere. This lidar combines the coherent Doppler technique for wind detection and the differential absorption lidar (DIAL) technique to provide a multifunctional capability. DIAL and coherent lidars have traditionally been thought of and implemented as separate instruments, but the research reported here has shown a demonstration of combining the coherent and DIAL techniques into a single instrument using solid-state lasers. The lasers used are of Ho:Tm:YLF, which operates at a wavelength of 2 μm. This wavelength is a further advantage to the lidar, as this wavelength offers a much higher level of eyesafety than shorter wavelengths conventionally used for DIAL.

Two generations are lidars are described, with the first design making combined measurement of wind and water vapor. Wind speed measurements are shown of a precision better than 1 m/s, making it useful for many meteorological applications. Water vapor concentration measurements were of 86% accuracy, requiring improvement for scientific applications. This preliminary experiment revealed the largest source of error in concentration measurement to be a lack of stability in the wavelength of the laser. This problem was solved by implementing a means to precisely control the continuous-wave laser that injection seeds a pulsed laser. The finely tunable Ho:Tm:YLF laser was

stabilized to absorption lines of both carbon dioxide and water vapor using a wavelength modulation technique. Long-term stabilization to within 13.5 MHz of absorption line center is shown, representing the first frequency-stabilized laser at or within 500 nm of 2-μm wavelength. Results are presented on injection seeding a pulsed Ho:Tm:YLF laser to impart the tunability and stabilization to the pulsed laser output.

The stabilized laser system was incorporated into a second-generation coherent DIAL to make a combined measurement of wind and carbon dioxide concentration. The DIAL measurement accuracy of concentration was improved to 29%, and designs are suggested for a further reduction in error. The absorption lines around 2-μm have recently become of great interest for a high-accuracy measurements of carbon dioxide for studies in the global carbon cycle, and the lidar demonstration and laser technology presented here are enabling first steps to meet scientific needs for carbon dioxide profiling.

This work is dedicated to Melissa and Kirsten for providing the things in life that matter the most: faith, love, and laughter.

ACKNOWLEDGMENTS

The work described in this dissertation is an example of electro-optical systems integration, which is a sophisticated way to say that I've borrowed technology from many sources and stood on the shoulders of many giants. Among these giants is Dr. Amin Dharamsi who taught me about wavelength modulation spectroscopy and molecular motion, and in general helped me to become a better engineer. Mulugeta Petros spent countless hours with me in the lab and built the pulsed laser and injection seeding circuit described in Chapter 6. Richard Davis provided an endless stream of HITRAN analyses, enthusiastically sharing his expertise on the particulars of atmospheric absorption. Carl Mills , Dr. Les Britt, and Carroll Lytle developed the real-time signal processing and display programs to make visualizations of wind fields. Anthony Cook and Terry Mack built the photodetectors used in these lidars and taught me the intricacies of polarization-maintaining optical fiber. Dr. Jirong Yu and Dr. Norman Barnes have pushed the maturity of 2-μm lasers to the point where lidars based on them are now feasible. Colleen Fitzgerald programmed the control loop for frequency stabilization described in Chapter 5. Several managers at NASA Langley Research Center, including James Barnes, Steven Sandford, Leonard McMaster, Ben Barker, and Dr. Upendra Singh, gave me time and encouragement as I chased a few strange ideas. My thanks are extended to Dr. Carl Holden, Dr. Ravindra Joshi, Dr. Karl Schoenbach, and Dr. Linda Vahala for serving on my graduate committee.

Several institutions came together to make this research possible including Sanders—Lockheed Martin, Inc., which built the lasers used in Chapter 2, the Defense Advanced Research Projects Agency which funded these initial lasers, and the US Air Force which loaned said lasers to NASA. NASA Langley Research Center gave me the time to work on this degree through the Full-Time Graduate Study Program and funding for this research through the Director's Discretionary Fund.

My family has my thanks for providing me my early education. My parents Wayne and Frances Koch gave me, among many other things, an optics kit when I was twelve years old. The spirit of this science toy carried over to my current work--my toys

are just more expensive now. My brother Walter showed me my first laser, the light from which became focused to a career choice.

Having the sky for a laboratory is a wondrous experience, best described in the Bible:

He loads the clouds with moisture; he scatters his lightning through them. At his direction they swirl around over the face of the whole earth to do whatever He commands them. Job 37:11-12

The wind blows wherever it pleases. You hear its sound, but you cannot tell where it comes from or where it is going. John 3:8

TABLE OF CONTENTS

LIST OF TABLES

LIST OF FIGURES

CHAPTER 1

INTRODUCTION: COHERENT DIFFERENTIAL ABSORPTION LIDAR

The purpose of this research is to develop a solid-state lidar that can measure gas concentrations and wind in the Earth's atmosphere. Lidar, an acronym for light detection and ranging, involves transmitting a pulsed laser into the atmosphere and collecting the light reflected by aerosols and gaseous molecular constituents of the atmosphere.[1] These atmospheric constituents exhibit a rich interplay with laser light, including Rayleigh scattering, Mie scattering, Raman scattering, absorption, fluorescence, and Doppler shifting. These optical phenomena can be exploited to measure a wide range of atmospheric characteristics such as aerosol concentration, trace gas concentration, temperature, and wind. Two lidar techniques are addressed in this research: coherent lidar for measurement of wind and differential absorption lidar (DIAL) for measurement of gaseous constituent profiles. These two techniques have been combined to develop a multifunctional instrument capable of performing both coherent and DIAL measurements, tasks that have traditionally been implemented as separate instruments.

The lidar described in this research was first built as a wind sensor used to track the turbulent wake vortices trailing behind landing aircraft.[2] This application of Doppler lidar has since matured into an operational field instrument deployed at airports to profile wind and track wakes.[3] Wind measurements have many other applications in meteorology and aviation safety including detection of clear air turbulence ahead of flying aircraft, detection of wind shear, and projectile targeting.[4,5,6] Global-scale measurement of tropospheric winds has been identified as the biggest missing component of data for weather forecasting,

---

The journal model for this work is Applied Optics.

and Doppler lidar has been under development for several years to provide measurements from an orbiting satellite.[7,8]

A combined coherent/DIAL system was then built, this being the first solid-state lidar capable of both wind and gas measurement.[9] Coherent DIAL similar in concept to the research described in this dissertation has been the subject of theoretical studies and simulations, but had not been implemented into a working insturment.[10,11] A coherent DIAL has been demonstrated, however, and put into field use based on CO_2 lasers at 10 μm wavelength.[12,13] The disadvantages of this 10-μm wavelength system are that it involves a pressurized gas as a gain medium and that the 10-μm wavelength region is characterized by a continuum of absorption. A motivation thus exists to build a coherent DIAL using a reliable laser material at a different wavelength.

Solid-state lasers use a small crystalline material as the lasing medium, as opposed to gas lasers which use cumbersome pressurized gases. Solid-state lasers are desirable because of their small size, rugged construction, light weight, and simple maintenance needs. The lasers used in this research are Ho:Tm:YLF—an activator of holmium and a sensitizer of thulium in a host of yttrium lithium fluoride. This laser has the additional benefit of a high level of eye safety due to its output wavelength at 2 μm.[14] This infrared wavelength is absorbed by the damage-resistant cornea, rather than being imaged onto the sensitive retina. Other researchers are studying coherent DIAL based on a solid-state laser of Nd:YAG at a wavelength of 1.1 μm, but this approach suffers from a lack of eyesafety.[15]

In this research coherent DIAL measurements were made of water vapor, a trace gas of great importance in atmospheric processes. Although water vapor typically makes up only 1% of the Earth's atmosphere it has a profound impact on the dynamics of the

atmosphere.[16] Phase changes of water vapor are accompanied by large latent heat changes which add or subtract heat from the atmosphere. Transport of water vapor by wind and subsequent phase transformations are thus a major component of heat transfer in the atmosphere. Water vapor is also a greenhouse gas, making it critical to studies of climate change. Spatially resolved measurements of water vapor are therefore important to climatology. Weather forecasting also benefits from tracking water vapor in the prediction of cloud formation, precipitation, and storms.

Water vapor profiles are currently measured for use in weather and climate models by a network of weather balloons released twice daily throughout the populated regions of the world.[17] These radiosonde measurements have many disadvantages. First, the temporal resolution is much too coarse, with 12 hours between samples. Second, the geographic coverage is insufficient with a typical spacing between sampling sites in North America of 400 km. Measurements over other continents can be even more sparse, and there is almost no data taken over the oceans. Satellite observations are also made of water vapor by infrared and microwave radiometers, but with insufficient vertical resolution.[18,19] Sensing of water vapor by lidar is thus of interest because it can offer high vertical resolution and continuous global coverage if it were deployed on a satellite. Desired spatial resolution is 200 km horizontally and 1 km vertically from the ground to the tropopause. An accuracy in concentration measurement of less than 20% is required.[19]

This lidar was also used to measure concentrations of carbon dioxide, another trace gas highly influential on the atmosphere. The concentration of atmospheric carbon dioxide influences global temperatures as a greenhouse gas, indicates rates of plant photosynthesis, determines the composition of marine sediments, and indicates the oxidation state of the atmosphere.[16] Carbon is exchanged, primarily in the form of carbon dioxide, between the

atmosphere, biosphere, oceans, and lithosphere in a complex cycle that is critical to the support of life. Many questions have arisen about the effects of increasing concentrations of carbon dioxide placed into the air by fossil fuel combustion.

In particular, carbon dioxide concentration measurements are needed over large geographic areas with very high accuracy—better than 1% accuracy over 10 km horizontal samples.[21] Observation from a satellite is thus desired to achieve this spatial coverage. However, the only existing technology to measure carbon dioxide concentrations are infrared spectrometers which draw in a sample of gas to test. This in situ sensor is inappropriate for the required data. DIAL is a promising solution for remote sensing of carbon dioxide, and the research presented in this dissertation is the first use of DIAL for detection of carbon dioxide.

The following sections of this chapter describe the theory of coherent DIAL, commencing with an explanation of the coherent and DIAL techniques separately. In Chapter 2 the design and experimental results are presented of lidar measurements of wind and water vapor. While this preliminary demonstration of the coherent DIAL lidar was successful with good wind results, the accuracy with which water vapor content was measured must be improved for scientific or meteorological purposes. The primary source of the water vapor measurement error was the laser's drift in frequency over time. This drift took the laser off of absorption line center, creating errors in the absorption cross-section to use in DIAL calculations. Research was then aimed at eliminating this drift by stabilizing the lasers by referencing to a sample of gas in a small pressurized cell. The first step in accomplishing this was to redesign the continuous wave (CW) laser used to control the spectral properties of the output pulse to allow the precise tunability required to resolve the center of an absorption line. The design and implementation of this laser is the subject

of Chapter 3. Chapter 4 describes wavelength modulation spectroscopy, which is the basis for the laser stabilization scheme described in Chapter 5. Chapter 6 then describes the integration the of the stabilized CW laser with a pulsed laser. The next generation implementation of the Doppler DIAL is discussed in Chapter 7, with results presented on the measurement of carbon dioxide.

1.1 Coherent Lidar

The idea behind coherent lidar is summarized in Figure 1.1. A pulse of light is transmitted into the atmosphere and a telescope collects a portion of the light scattered by aerosols. Range to the target portion of the atmosphere is calculated by noting the time of the atmospheric return with respect to the time the pulse was transmitted. Range is then calculated by

$$R = \frac{(t_{ret} - t_{xmit})c}{2} \quad , \quad (1.1)$$

where t_{ret} is the time of the atmospheric return signal, t_{xmit} is the time at which the pulse was transmitted, and c is the speed of light. The motion of the aerosols, from which the laser light scatters, Doppler shifts the laser frequency. This Doppler shift is the parameter of interest here and is demodulated from the return signal by a heterodyne process described later. The Doppler shift is given by

$$\Delta\upsilon = \frac{2v}{\lambda} \quad , \quad (1.2)$$

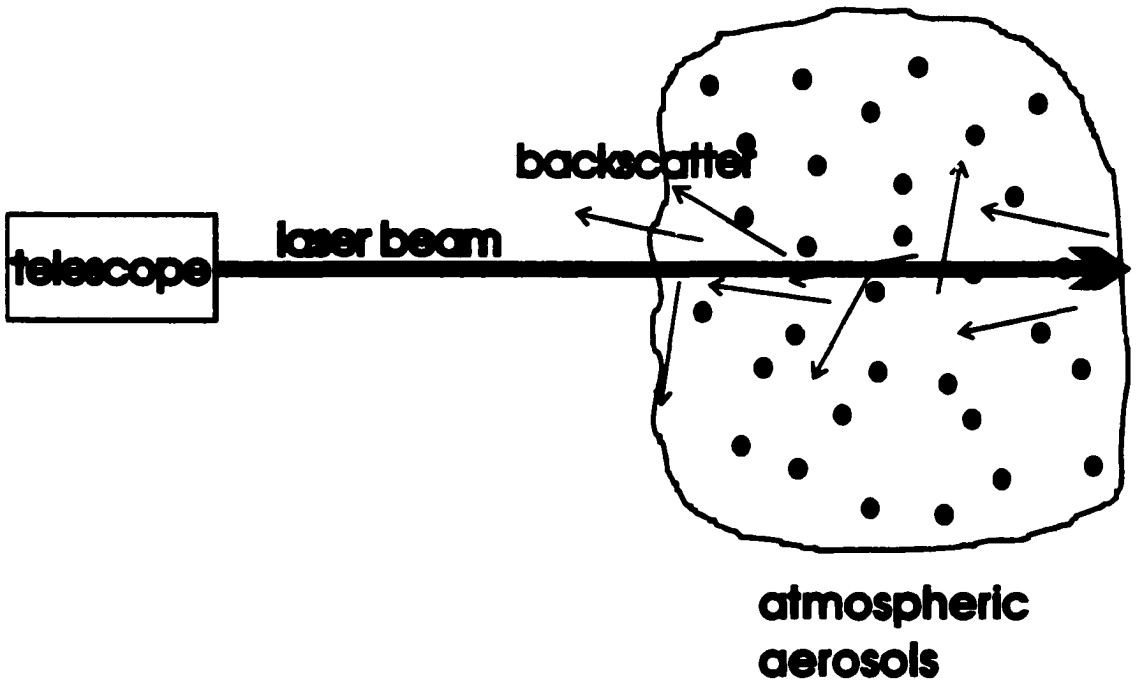

Figure 1.1: The principle of operation of coherent lidar. A telescope serves as both a transmitter for the laser beam and as a receiver for the atmospheric backscatter.

where v is the velocity of the aerosols and λ is the wavelength of the laser.

The range resolution and velocity resolution of a coherent lidar measurement can be analyzed by noting that the temporal width of the laser pulse creates some ambiguity in range. That is

$$\Delta R = c\frac{\Delta \tau}{2} \quad . \qquad (1.3)$$

Where ΔR is the range resolution, c is the speed of light, and $\Delta\tau$ is the pulse width of the laser. Similarly, the spectral width of the laser pulse creates some ambiguity in determining the velocity:

$$\Delta v = \lambda\frac{\Delta f}{2} \quad . \qquad (1.5)$$

Where Δv is the velocity resolution and Δf is the laser spectral width. Combining Equations (1.3) and (1.4) yields.

$$\Delta R \Delta v = c\lambda \frac{\Delta \tau \Delta f}{4} \quad . \quad (1.5)$$

Δτ and Δf are, however, related by an inverse proportionality for a single-frequency spectrum. For a gaussian pulse

$$\Delta \tau \approx \frac{1}{\Delta f} \quad . \quad (1.6)$$

So Equation (1.5) reduces to

$$\Delta R \Delta v = \frac{c\lambda}{4} \quad . \quad (1.7)$$

Equation (1.7) indicates that there is a trade off between range resolution and velocity resolution. To improve the measured velocity resolution, a greater extent of range must be sampled, and vice versa. The wavelength of the lidar could be decreased to enhance optimize this trade off, but lower wavelengths are disadvantageous for eye-safety concerns.

The strength of the atmospheric backscatter collected by the telescope can be calculated by following the analysis of Targ et al.[5] This modeling is based on analyzing the signal-to-noise ratio, SNR, for a coherent lidar atmospheric return as a function of range, R:

$$SNR(R) = \frac{E\eta\beta\lambda\pi D^2}{8(1+f)hBR^2} \exp[-2\int_0^R \alpha(R')dR'] \quad , \quad (1.8)$$

where E is the laser pulse energy, β is the backscatter coefficient, λ is the wavelength, D is the telescope diameter, f is the amount of amplifier noise as a fraction of total noise, B in the processing filter bandwidth, α is the one-way atmospheric attenuation, and η is an efficiency parameter. The exponential term accounts for attenuation in the atmosphere by absorption, quantified by an absorption coefficient α. The efficiency parameter η represents several losses to the signal:

$$\eta = \frac{0.4\eta'}{1+[1-(R/F)]^2(\pi 0.372D^2/4\lambda R)^2+(D/2S_o)^2} \quad , \qquad (1.9)$$

where η' is the two-way optical efficiency due to losses in the transmitter/receiver optics, and F is the range at which the telescope is focused.

The denominator of Equation (1.9) accounts for loss of signal by two phenomena. In the second term of the denominator geometrical optical effects are shown involving the size of the illuminated target and the associated wavefront mismatch with the receiver telescope. Also in this term, effects have been included by the truncation of the gaussian laser beam by the aperture of the receiver—this leads to the constant 0.372. The third term in the denominator shows the effects of refractive turbulence, which causes an expansion of the transmitted beam and a loss of coherence of the backscattered field. The coherence of the atmosphere is quantified by a transverse coherence length:

$$S_o = \left[2.9\frac{2\pi}{\lambda}\int_0^R C_n^2(R')\left(1-\frac{R'}{R}\right)^{5/3} dR'\right]^{-3/5} \quad , \qquad (1.10)$$

where C_n^2 is the refractive index structure of the atmosphere, indicating the strength of turbulence in the atmosphere. Turbulence has the effect of shrinking the size of the coherence length of the atmosphere as seen by the negative exponent in Equation (1.10). Turbulence features, which can be envisioned as rolling spheres of wind, occur in a range of diameters exhibiting a 5/3 roll off, called the Kolmogorov spectrum.[22] The factor 2.9 in Equation (1.10) is called the Kolmogorov constant, and is generated in the integration over the spectrum of turbulence diameters.[23]

The absorption coefficient α is the key to the DIAL technique described in the following section, and can further be quantified as

$$\alpha(R) = n(R)\sigma(R) \quad , \quad (1.11)$$

where n(R) is the number density of the gas of interest and σ(R) is the absorption cross-section of the gas.

By assuming parameters associated with Equations (1.8) to (1.11) the range capability of a Doppler lidar can be simulated. The results of such a simulation are presented in Figure 1.2 based on the parameters of Table 1.1. Two features of the atmosphere, backscatter β and turbulence C_n^2, are highly variable, and Figure 1.2 includes a variation of these parameters that might be encountered in the lower troposphere. For example, the β value used ranges from a 10^{-6} m^{-1} sr^{-1} of a hazy day to a 10^{-8} of very clear skies. C_n^2 is used varying from a 10^{-13} $m^{-2/3}$ typical of a cold winter night to 10^{-11} of a hot summer afternoon.

Within the range capability suggested by Figure 1.2, in which the signal-to-noise ratio is greater than 0 dB, information can be derived about the wind. Wind

E = 5 mJ
η' = 20%
λ = 2050 nm
D = 10 cm
f = 0.1
F = 3 km
$C_n^2 = 10^{-13}$ to 10^{-11} $m^{-2/3}$
$\beta = 10^{-7}$ to 10^{-6} m^{-1} sr^{-1}
Atmosphere = U.S. Standard Atmosphere, 1976[24]

Table 1.1: Laser and atmospheric parameters used in the simulation of SNR.

speed is encoded in the atmospheric backscatter in the form of a Doppler shift, which is extracted by a heterodyne process. Just an in a radio receiver, heterodyning produces a signal at the difference in frequency between the received signal and the local oscillator. In the optical domain heterodyning is accomplished on the surface of a photodiode exhibiting a square law detection characteristic, thereby converting an optical frequency difference into an electronic signal. Since aerosol motion Doppler shifts the atmospheric return the heterodyne signal is correspondingly shifted in frequency by an amount described by Equation (1.2). These frequency shifts are in the radio frequency domain. If the outgoing pulse and local oscillator are at the same frequency, a positive or negative Doppler shift would produce the same heterodyne signal. To distinguish between positive and negative velocities, that is wind going toward or away from the observer, the frequency difference between the local oscillator and outgoing pulse is set at an intermediate frequency.

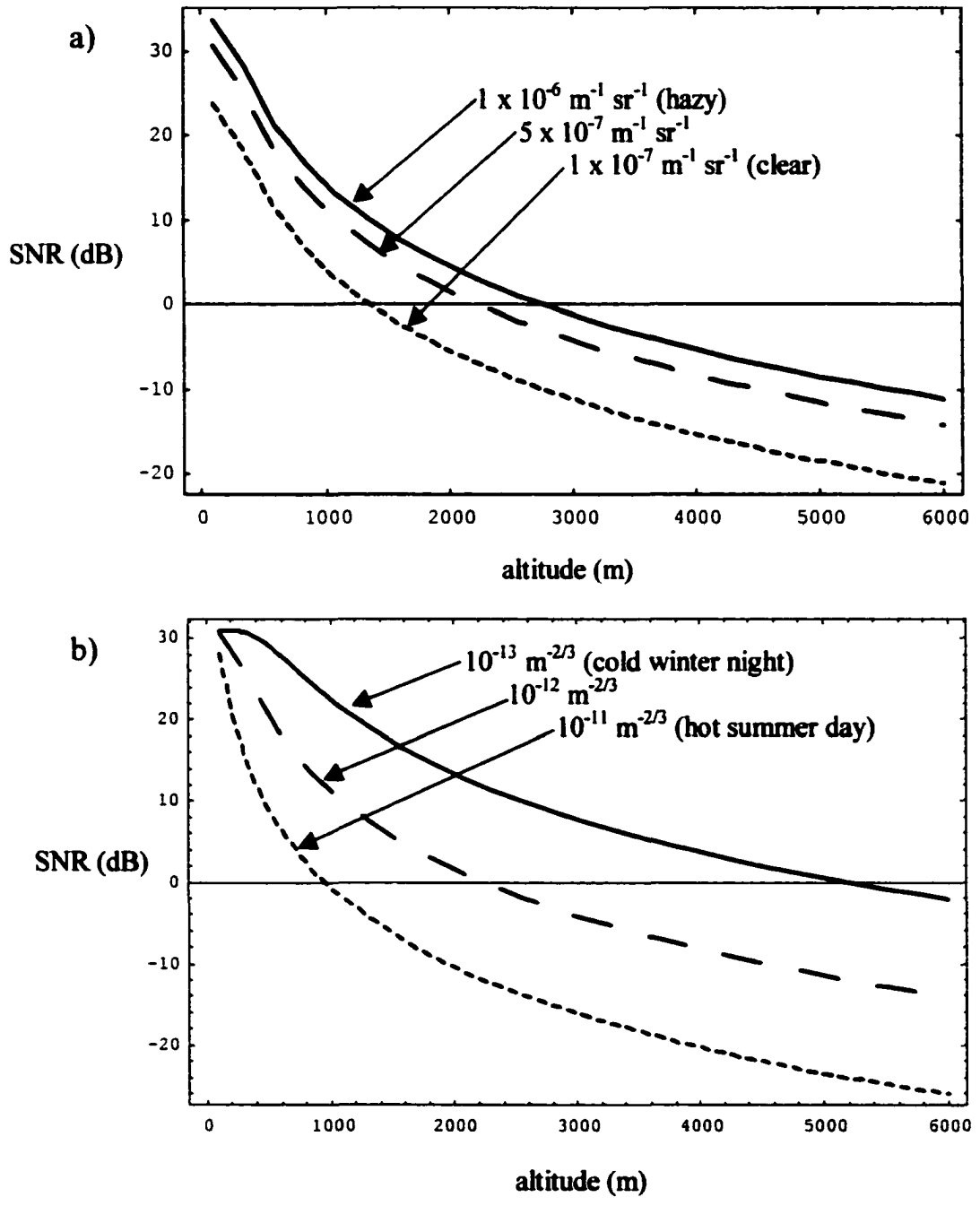

Figure 1.2: Simulation of coherent lidar signal-to-noise ratio as a function of range. Lidar beam is directed vertically assuming parameters of Table 1.1. In a) the level of backscatter has been varied with turbulence held constant at $C_n^2 = 1 \times 10^{-12}$ $m^{-2/3}$. In b) the level of turbulence has been varied with backscatter kept constant at 5×10^{-7} m^{-1} sr^{-1}.

The atmospheric return signal is partitioned into blocks of time, corresponding to different range bins. Spectral estimation techniques such as Fourier transforms are applied to the heterodyne signal to calculate wind velocity in each range bin.

1.2 Differential Absorption Lidar (DIAL)

DIAL provides a measurement of atmospheric gas concentration by taking advantage of the fact that molecules have distinct absorption features associated with them. Figure 1.3 shows the absorption lines in the atmosphere between the wavelength of 2049 to 2054 nm. Two important trace gases, water vapor and carbon dioxide, have absorption lines within this range that matches the capability of the Ho:Tm:YLF laser. The DIAL measurement works by recording the atmospheric backscatter with the laser alternately tuned on and off an absorption peak of the gas under study.

The scatter from the on-line pulse will be attenuated with range at a faster rate than the off-line pulse because of the difference in absorption. Comparing the rate of attenuation between the on-line and off-line pulses allows a determination of the concentration of gas as a function of range. Specifically, gas concentration can be calculated by considering the ratio of the on-line signal to the off-line signal:

$$\frac{S_{on}(R)}{S_{off}(R)} = \frac{\exp[-2\int_0^R n(R')\sigma_{on}dR']}{\exp[-2\int_0^R n(R')\sigma_{off}dR']} \quad . \qquad (1.12)$$

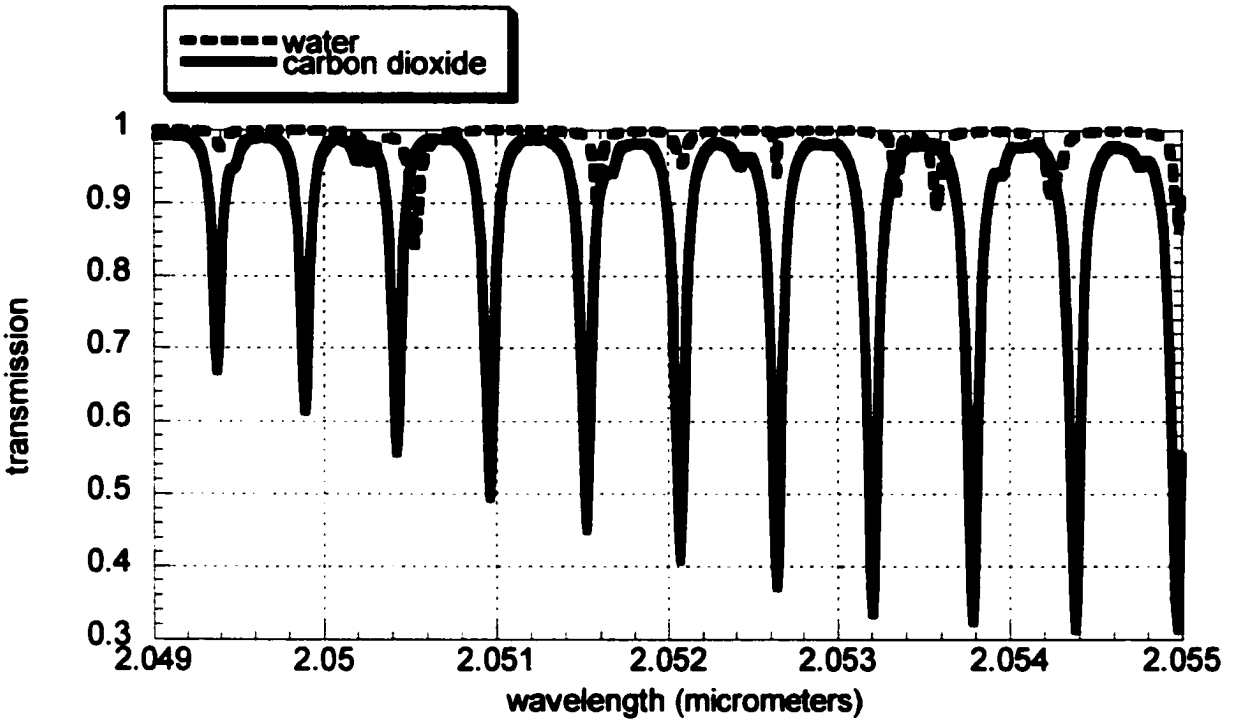

Figure 1.3: Absorption features of the atmosphere within the tuning range of the Ho:Tm:YLF laser as recorded in the HITRAN atmospheric database.[25] Absorption is over I km vertical path starting from the ground in a 1976 Standard Atmosphere.

This ratioing allows the concentration measurement to be self-normalizing. That is, the variables in backscatter, turbulence, pulse energy, telescope diameter, etc., of Equation (1.8) have been canceled out. Rewriting Equation (1.12):

$$\frac{S_{on}(R)}{S_{off}(R)} = \exp[-2\int_0^R n(R')\Delta\sigma dR'] \quad . \qquad (1.13)$$

Where $\Delta\sigma = \sigma_{on}-\sigma_{off}$, a differential absorption cross section. The interest is in calculating n(R), so solving Equation (1.13) yields

$$n(R) = \frac{1}{2\Delta\sigma}\frac{d}{dR}\ln\left[\frac{S_{off}(R)}{S_{on}(R)}\right] \quad . \qquad (1.14)$$

Approximating the derivative gives

$$n = \frac{1}{2\Delta\sigma(R_2 - R_1)}\ln\left[\frac{S_{on}(R_1)S_{off}(R_2)}{S_{on}(R_2)S_{off}(R_1)}\right] \quad , \qquad (1.15)$$

where R_1 is the closer range and R_2 is the farther range.

A key feature in the design of a DIAL system is the selection of an absorption line which offers an absorption cross-section that is neither too strong nor too weak. Absorption that is too weak will not show a distinguishing difference between the on-line and off-line signals. The differential absorption would then not be pronounced enough to make a precise measurement of gas concentration. On the other hand, an absorption feature that is too strong will swallow the on-line probe energy within a short range, so that useful gas measurements can only be made within a range very close to the lidar.

The modeling of SNR and range capability derived by Equations (1.8) to (1.11) allow a means to determine if a particular absorption line offers this optimum balance for DIAL. As an example, the performance using two lines is presented in Figure 1.4 for a water vapor line and a carbon dioxide line which were used for actual lidar tests. The on-line performance for both cases is compared to an off-line wavelength that was used for the simulation presented in Figure 1.2. These lines are shown in the tuning range of Figure 1.3: the water vapor absorption is centered at 2050.532 nm (absorption cross-section of 9.1 x 10^{-24} cm^2 molecule at ground level) and the carbon dioxide line is centered at 2050.428 nm (absorption cross-section of 7 x 10^{-22} cm^2 molecule at ground level). As this HITRAN data shows, there is a significant difference in the absorption strength of these two lines. This difference in strength is also reflected in Figure 1.4 as seen by comparing their rates of attenuation relative to the off-line signal.

The DIAL performance capability for these two simulations can be evaluated by observing two requirements. First, the SNR of both the on-line and off-line signal must be above 3 dB—signals overwhelemed by noise are useless. Second, there should be greater than 2 dB ratio between the on-line and off-line signals for a distinct differential absorption. Hence the useful range for the water vapor DIAL of Figure 1.4 is between 1900 and 3400 m, and the useful range for the carbon dioxide DIAL is between 400 and 2000m. These two absorption lines will work for DIAL, but each is effective only at a certain range.

A further consideration in analyzing DIAL performance is that gas concentration measurements will be more accurate with a stronger SNR on which to base the DIAL calculation of Equation (1.15). As an example, the case of Figure 1.4b would be more desirable than Figure 1.4a. A stronger absorption feature also offers more flexibility in

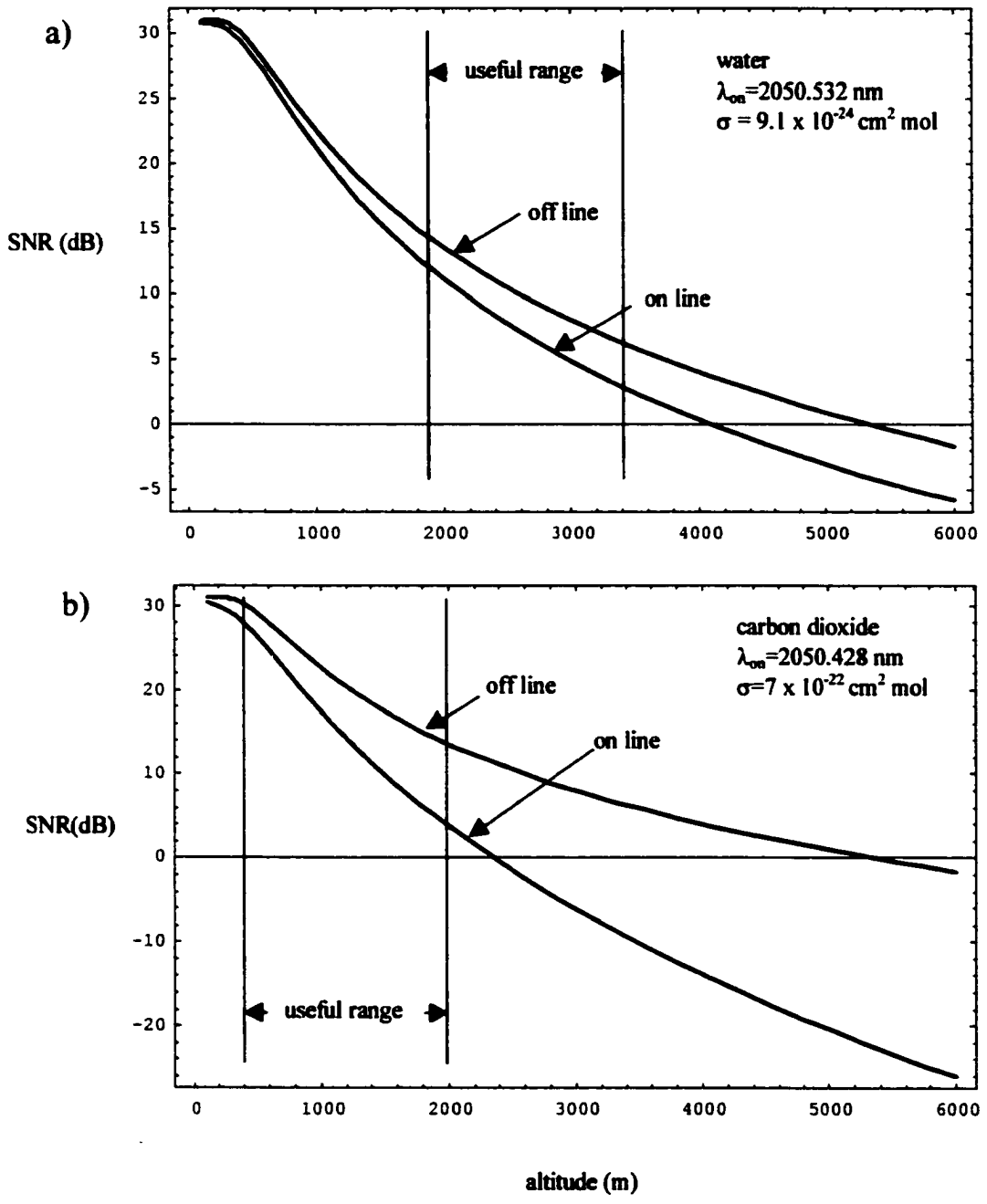

Figure 1.4: Comparison of range performance for on-line for (a) water vapor at 2050.532 nm and (b) carbon dioxide at 2050.428 nm. Laser and atmospheric parameters used are summarized in Table 1.1 with $\beta = 5 \times 10^{-7}$ m^{-1} sr^{-1} and $C_n^2 = 10^{-13}$ m$^{-2/3}$.

that the DIAL measurement can be made with the laser tuned onto the side of an absorption line.

In Chapter 2 the theory behind coherent DIAL will be put into practice with a demonstration of a Ho:Tm:YLF-based lidar system used to make measurements of both wind and water vapor concentration.

CHAPTER 2

DEMONSTRATION OF A COHERENT DIFFERENTIAL ABSORPTION LIDAR

In Chapter 1 the theory behind coherent DIAL was explored, while in this chapter the results are presented on a laboratory demonstration of the technique. Measurements were made of both wind and water vapor concentration, representing the first coherent DIAL implementation using a solid-state laser.[9] This lidar was first built solely as a coherent lidar for measuring wind fields based on Ho:Tm:YLF laser developed by Sanders—Lockheed Martin, Inc., and loaned to NASA from the US Air Force with the concurrence of the Defense Advanced Research Projects Agency, which funded the laser development. As is described in this chapter, these lasers were modified to include a means to injection seed the pulsed laser to produce single-frequency output pulses. Receiver optics were then added to complete the coherent lidar. Sample wind measurements are presented in Section 2.1. A DIAL capability was later added, as is described in Section 2.2.

Figure 2.1 shows a block diagram of the coherent lidar design. Two Ho:Tm:YLF lasers are involved in this design, both drawn within dashed boxes. The larger dashed box encloses a pulsed laser, which produces 4.5 mJ of energy in a 180 ns long pulse at a 20 Hz repetition rate. Two arrays of diode lasers serve as the pump source for the laser crystal. The laser resonator is implemented in a bow-tie shaped ring configuration, with a Q-switch shortening the pulse to 180 ns. Left to run by itself this laser would oscillate on multiple longitudinal modes, generating a spectrally broadened pulse unsuitable for measurements of Doppler shift. A technique called injection seeding, described in detail in Chapter 6, is used to force the pulsed laser to operate on a single longitudinal mode.[26]

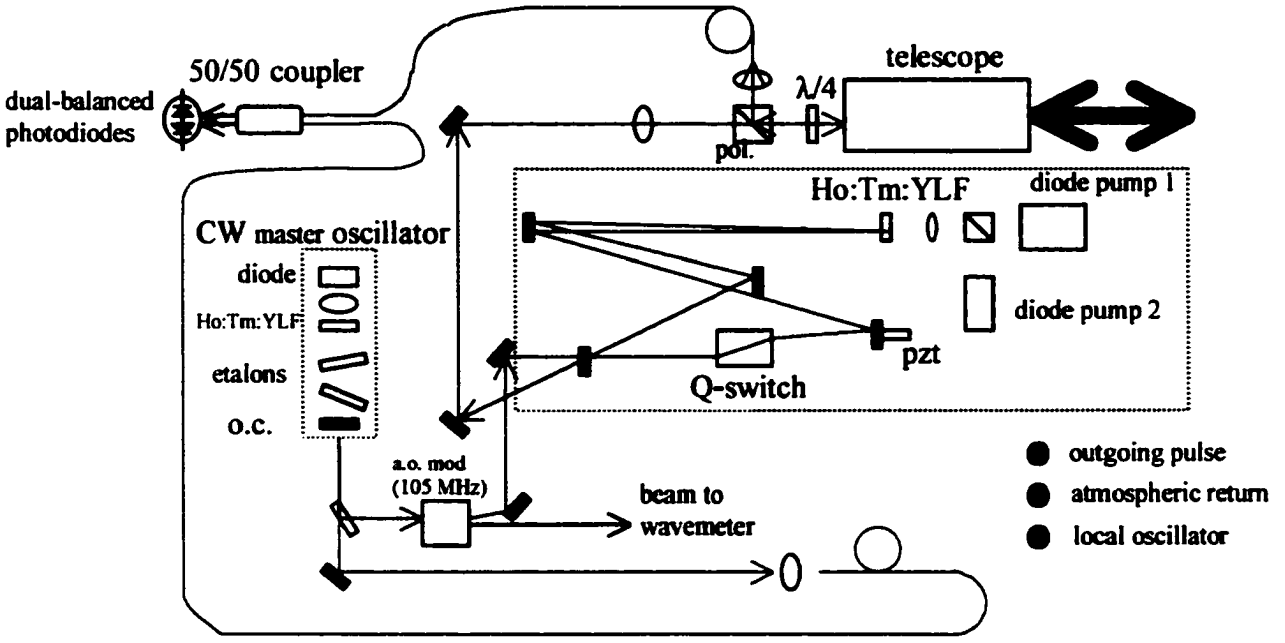

Figure 2.1: layout of coherent lidar.

Injection seeding works by introducing a sample of spectrally pure light into the pulsed laser cavity during the pulse build-up time. Laser oscillation builds up on this seed light, favoring the pulsed laser longitudinal mode closest in wavelength to the seed. However, to make this seed take hold the pulsed cavity mode resonance must correspond to the wavelength of the injection seed.[27] To accomplish this match the pulsed laser cavity length is ramped during the pumping cycle, and a condition of resonance is monitored by a photodiode. When a cavity resonance is detected the Q-switch is fired. Ramping of the pulsed laser cavity length is performed with a piezo-electric translator (PZT) pushing a cavity mirror. Figure 2.2 summarizes the signals and timing involved in the ramp-and-fire resonance matching.

The injection seed light is provided by another Ho:Tm:YLF laser in the system called the continuous-wave (CW) master oscillator, described in detail in Chapter 3. The CW master oscillator is made to operate with a narrow single-frequency spectrum by a pair of etalons inside the linear laser cavity. A part of the output of the CW master oscillator is coupled into the pulsed laser cavity after passing through an acousto-optic modulator. For reasons to be described later, the acousto-optc modulator shifts the frequency of the seed beam, and therefore of the pulsed laser output, by 105 MHz. Another part of the CW master oscillator is focused into an optical fiber for use as a local oscillator in a heterodyne process.

The output of the pulsed laser is steered toward a telescope which serves to expand the laser beam diameter by a factor of twenty. Atmospheric backscatter is also collected by the same telescope and focused into an optical fiber. The transmitted and received paths are separated by a polarization scheme—the linear polarization of the

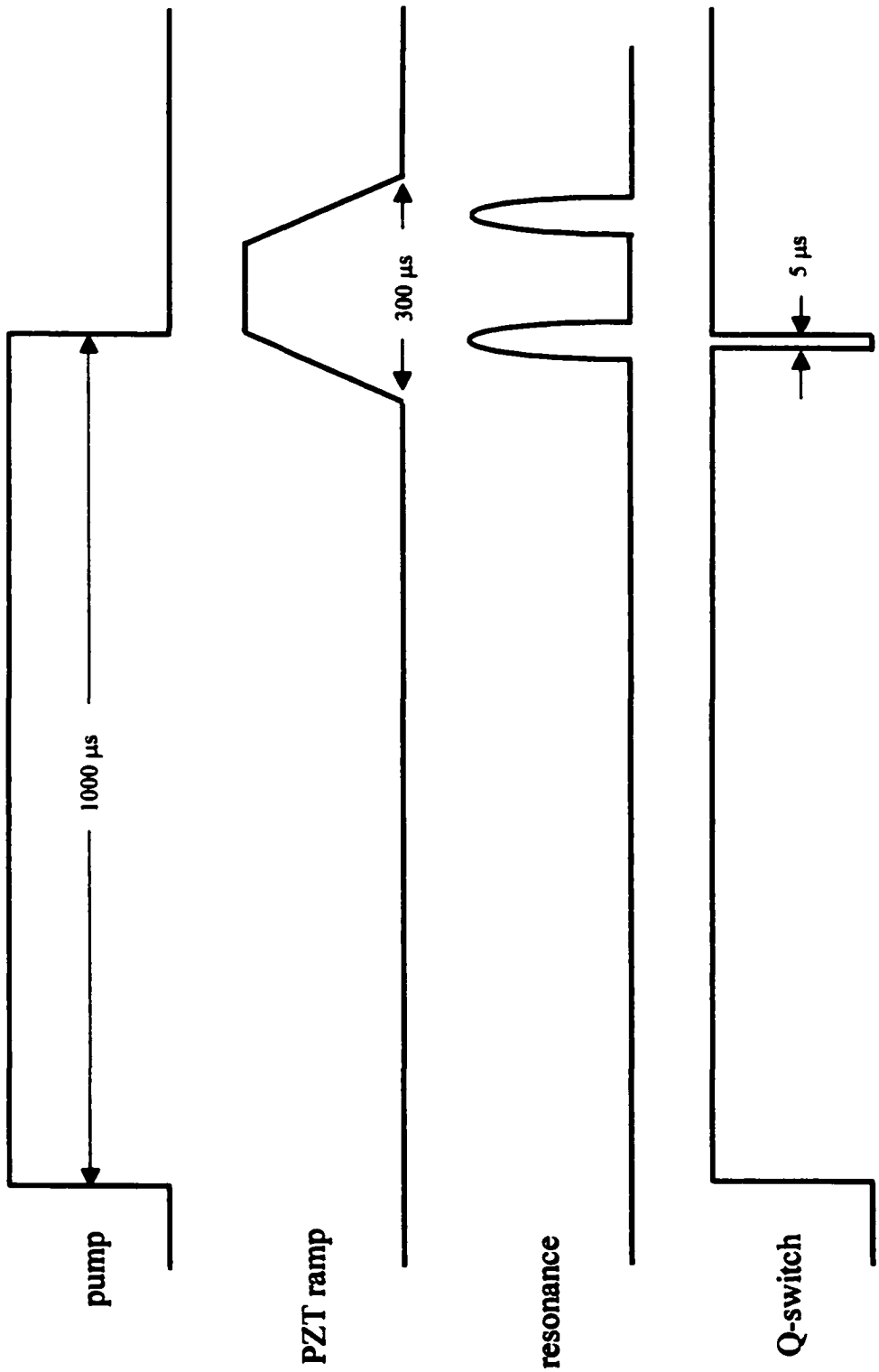

Figure 2.2: Signals associated with ramp-and-fire resonance matching.

output pulse is passed by a polarizing beam splitter and then made circular by a quarter-wave plate. The atmospheric aerosols reflect the light in an opposite sense polarization, which the quarter-wave plate makes linear, but rotated 90 degrees with respect to the outgoing polarization. The polarizing beam splitter then turns the atmospheric return toward the optical fiber.

Doppler shift information is extracted from the atmospheric return by heterodyning with the local oscillator. Just as in the design of a radio receiver, heterodying produces a signal at the difference in frequency between the received signal and the local oscillator. In the optical domain heterodyning is accomplished on the surface of a photodiode exhibiting a square law detection characteristic, thereby converting an optical frequency difference into an electronic frequency difference. Since aerosol motion Doppler shifts the atmospheric return the heterodyne signal shifts are in the radio frequency range. If the outgoing pulse and local oscillator are at the same frequency, a positive or negative Doppler shift would produce the same heterodyne signal. To distinguish between positive and negative velocities, that is wind going toward or away from the observer, the frequency difference between the local oscillator and outgoing pulse is set at an intermediate frequency. This is the function of the acousto-optic modulator described earlier. The beam transmitted from the telescope is directed into a scanning device based on rotating mirrors. Computer-controlled encoders within the scanner indicate the orientation of the laser beam so that the direction of the output pulse is known.

The photodetector consists of a InGaAsP PIN photodiode connected to a preamplifier, which is AC coupled to a 50 Ω output. Figure 2.3 and 2.4 show sample

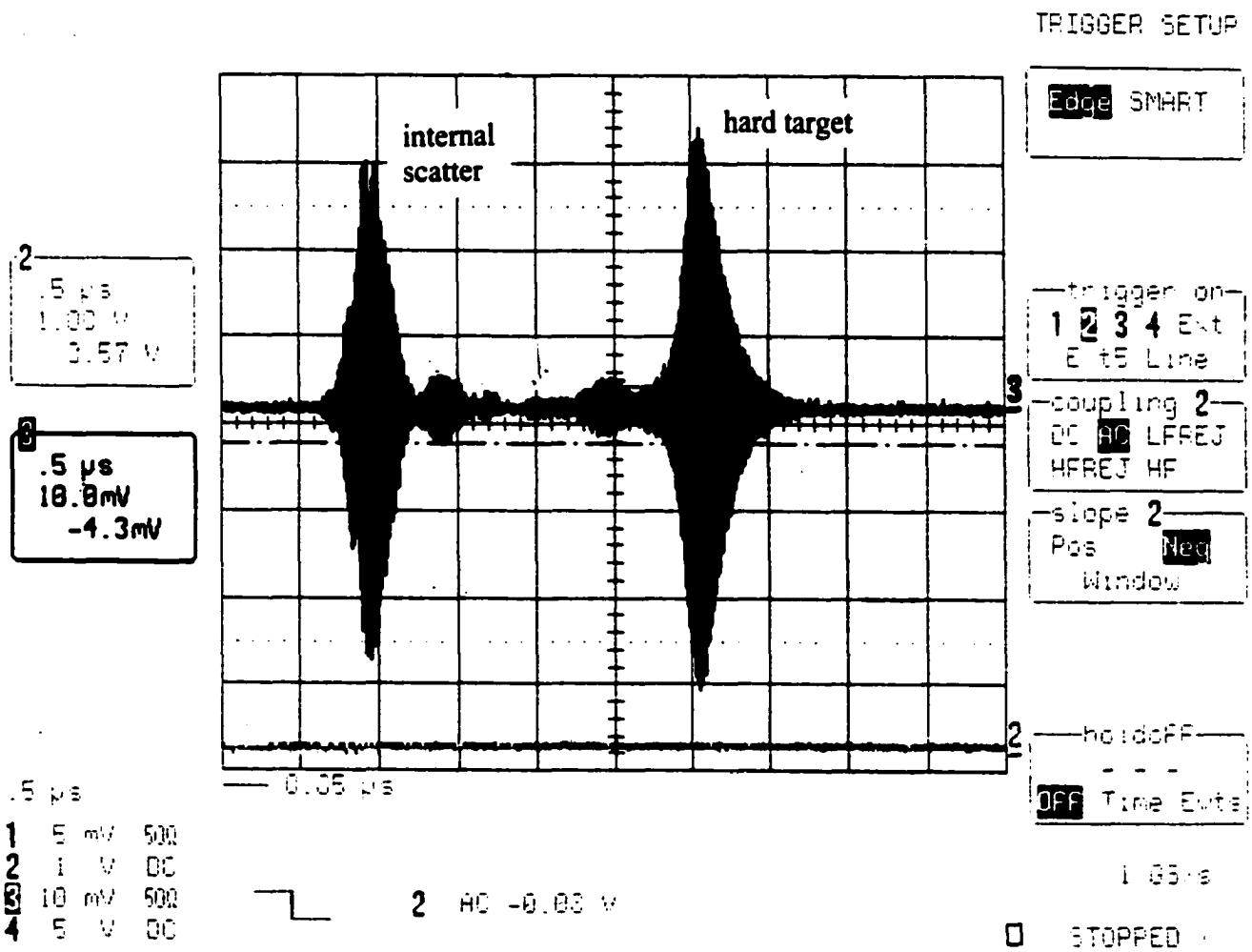

Figure 2.3: Heterodyne signal output from photodiode/preamp. Strong features are observed at time zero (scatter from optics and telescope) and at 2.125 µs later (return from a tree 318 m away). Scatter from aerosols is seen before hitting the hard target.

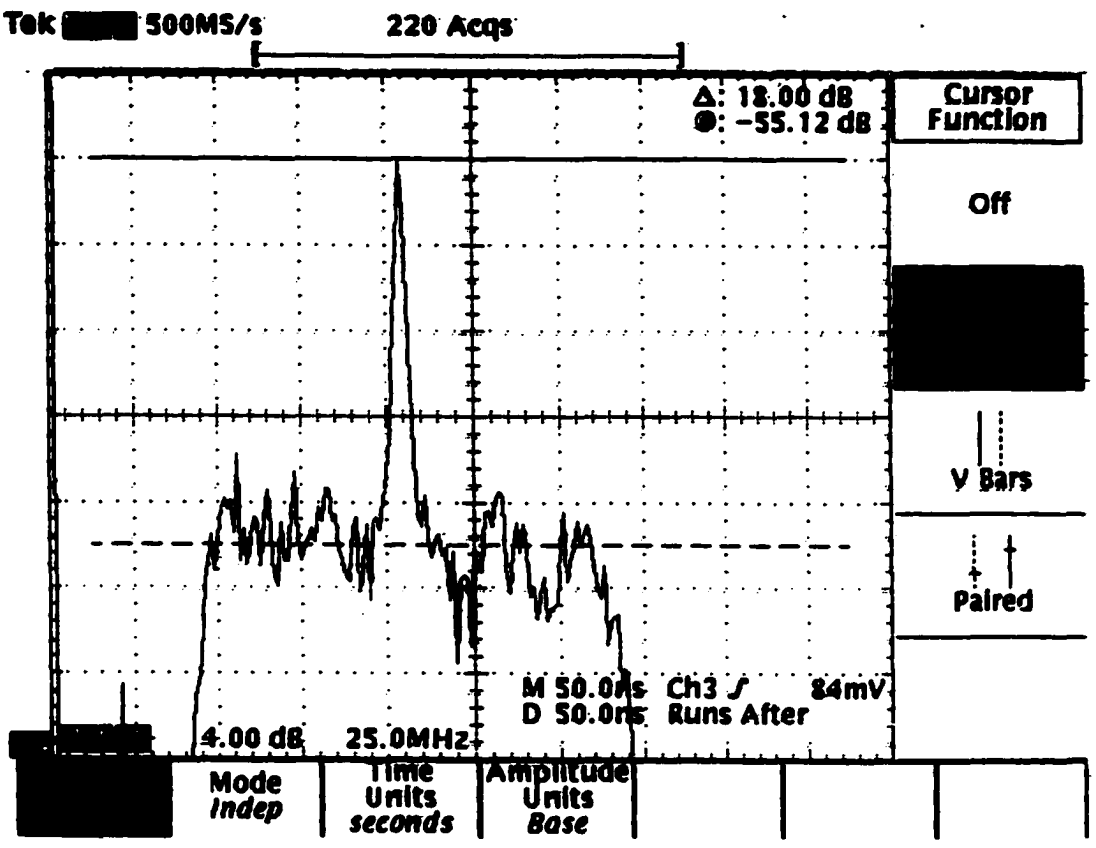

Figure 2.4: Fast Fourier transform (FFT) of atmopheric return signal. The FFT is taken over 500 points and averaged over 10 laser pulses. The corresponding range is from 435 to 585 m.

heterodyne signals at the output of this preamplifier—Figure 2.3 is in the time domain and Figure 2.4 is in the frequency domain. The output laser pulse appears in the time domain signal of Figure 2.3 as a 105 MHz sine wave within the envelope of the gaussian laser pulse shape. Since the photodetector is AC coupled this signal has a bipolar characteristic. This scatter of the output pulse from the optics of the lidar blinds the lidar from viewing the aerosol scatter until the scatter pulse dissipates. While this blinding is an unfortunate side effect, the internal scatter pulse is monitored to mark the zero position in both time and Doppler offset. All range and timing calculations are based on the peak of the internal scatter pulse by referencing to the peak of this signal. The sine wave contained within the gaussian enveloped is also measured for frequency, as this frequency marks an intermediate frequency corresponding to zero Doppler shift. Doppler effects created by aerosols in motion will shift the laser wavelength about this intermediate frequency. The intermediate frequency has been nominally fixed in this lidar design at 105 MHz by a modulation of the injection seed beam. However, the ramping of the pulsed laser cavity can cause MHz order shifts of the intermediate frequency. Hence, the intermediate frequency must be monitored on every shot by observing the internal scatter.

Figure 2.3 also shows a strong signal return as the laser pulse struck a tree located 318 m away from the lidar. This pulse is a copy of the internal scatter, since the tree is not in motion. If the hard target scatter were from a moving object, then the sine wave inside the gaussian envelope would be Doppler shifted from the intermediate frequency. Scattering from hard targets is useful for alignment of the receiver optics; such was the case when the data of Figure 2.3 was recorded. The signal of primary interest is that from aerosols, which can be seen in the region between the internal scatter and hard

target. The signal level from aerosols from a particular range changes from shot to shot due to a random phase distribution of the scattering. This error phenomenon, called speckle, can only be reduced by averaging.

Viewing the heterodyne signal in the frequency domain, as presented in Figure 2.4, offers a better visualization of the lidar signal. A noise floor is seen extending from 45 MHz to 165 MHz, created by a bandpass filter, from which extends a strong signal centered near 105 MHz. This signal indicates two important features about the aerosols residing between 435 to 585 m range: the motion of the aerosols and the concentration of the aerosols. The motion of the aerosols will Doppler shift the center frequency about the intermediate frequency. In the case of Figure 2.4 the center frequency shows a shift of 1 MHz, corresponding to a line-of-sight wind speed of 1 m/s. The second feature, the concentration of aerosols, is manifested in the amplitude of this frequency domain feature, as indicated by the cursors in Figure 2.4. A higher concentration of aerosols will result in stronger backscatter, and the amplitude of the spectral feature of Figure 2.3 would increase in amplitude. Measurement of this amplitude is the basis of DIAL.

Reduction of the raw data signals portrayed in Figures 2.3 and 2.4 requires substantial processing to create a measurement of wind velocity or water vapor concentration. The basic idea behind this processing is to digitize the heterodyne signal of Figure 2.3, determine the zero reference in time and Doppler shift, partition the atmospheric return into bins, and analyze the frequency shift or power within each bin. The processing of the heterodyne signal is presented in Section 2.1with regard to wind measurement and in Section 2.2. with regard to DIAL.

2.1 Wind Measurement

The electronics to accomplish the real-time processing of the wind signal is shown as a block diagram in Figure 2.5. The signals represented by Figure 2.3 and 2.4 are those that would be seen after the bandpass filter of Figure 2.5. This raw signal is amplified by a circuit which applies a different gain for two time sections of the backscatter signal. A lower level of gain is applied to the internal scatter pulse than to the aerosol return because the aerosol return is expected to be a much lower signal level. The timing over which these two different gains is applied is referenced to a trigger signal indicating when the laser pulse is fired. This attention to gain is necessary in order to keep the signal within the dynamic range of a digitizer, which samples the signal at 500 Ms/s with 8 bit representation. The sample rate of 500 Ms/s was selected to ensure that no aliasing occurs in the digitization. With the upper edge of the bandpass filter at 165 MHz, which corresponds to a 60 m/s Doppler shift, 500 Ms/s offers a comfortable margin above the Nyquist frequency. A unique aspect of this digitizer is that is flows its samples out in real-time, allowing them to be quickly captured by the digital signal processor (DSP).

The DSP consists of sixteen Texas Instruments C-40 chips integrated onto four cards. The DSP is programmed to break its task into chunks of range called bins. Each bin is typically 256 samples long, corresponding to a section of range 76.8 m long. However, the first range bin is made longer, typically 512 samples, to catch the internal scatter pulse. This first bin is analyzed for the peak of the pulse envelope, marking the time reference for range calculations, and frequency content, marking the Doppler reference for velocity calculations. Range bins containing the aerosol scatter are

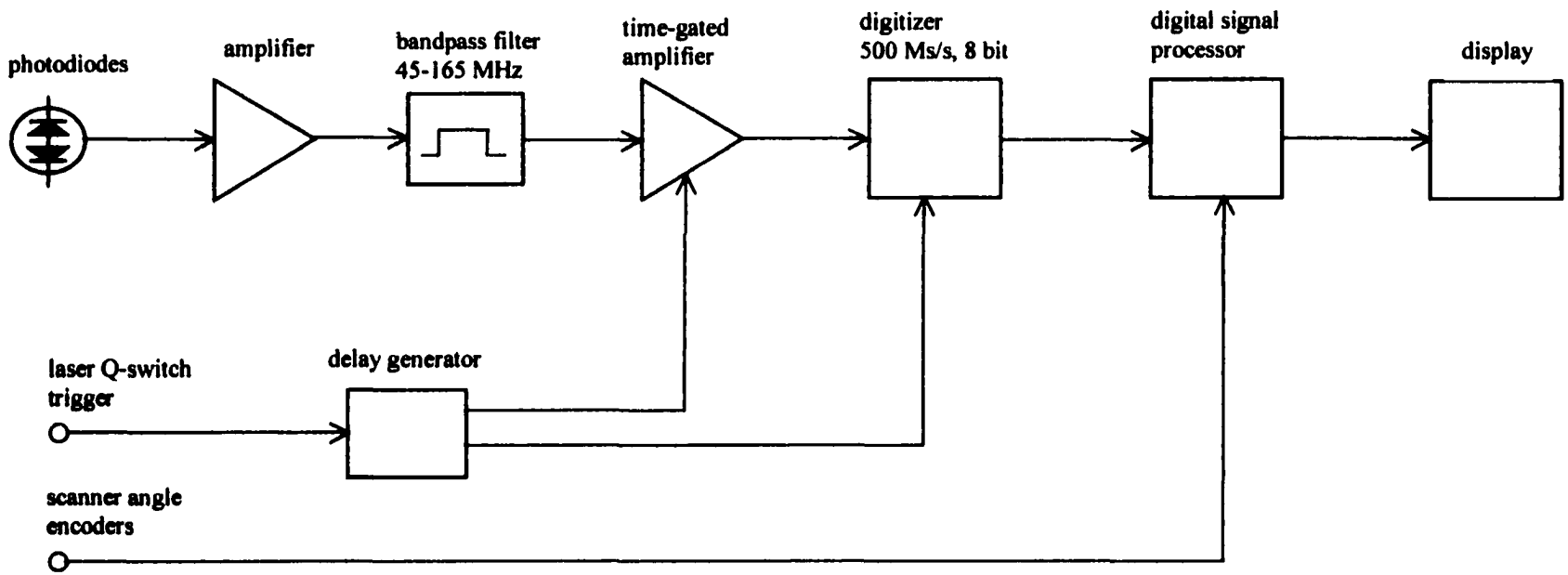

Figure 2.5: Block diagram of real-time wind processing.

processed with an FFT of the samples in the bin. The peak frequency indicated by the FFT is subtracted by the Doppler reference frequency, and velocity is calculated by Equation (1.2). The velocity in each bin is typically averaged over several pulses to reduce the effects of speckle fluctuation. Each pulse of velocity versus range calculation is tagged with an indication of the scanner orientation so that they can be plotted on a computer display.

Figure 2.6 is a sample display of a wind field as the lidar beam is scanned in elevation from 1° (horizontal) to 10°. Wind speed is shown in color code with the negative bias indicating a wind direction toward the lidar. Much structure is found in the wind on this particular day, characterized by strong gusts. As a general trend, the wind speed is seen to be increasing with altitude. This is an expected occurrence as friction with the ground tends to impede wind flow. Two interesting turbulent features are detected, which illustrate the sensitivity and utility of coherent lidar. First, at 600 m range near ground level a swirl of wind is detected that is caused by the wake of a landing C-130 aircraft that flew through the area being scanned. Second, at 800 m range turbulence is caused by the wind blowing over the roof of a single-story building is observed. The wind blowing over the roof curls back toward the building.

2.2 DIAL Measurement of Water Vapor

During development of the coherent lidar, the presence of absorption lines was recognized with regard to keeping the laser wavelength away from strong absorption that would limit range capability. The research described in this section was initiated to turn these absorption features to an advantage by a DIAL technique. The first problem to face

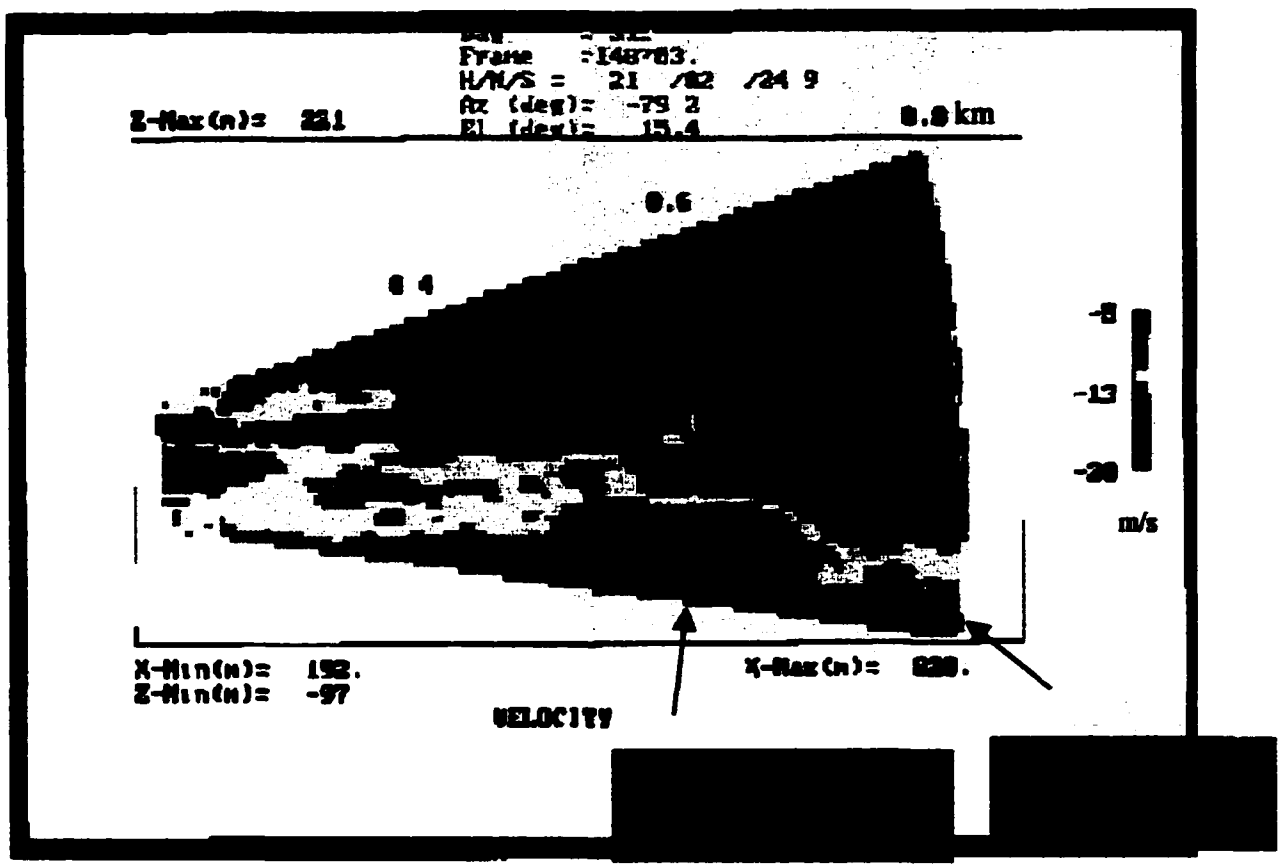

Figure 2.6: Velocity profile as lidar beam is scanned in elevation over runway at Langley Air Force Base. Wind speed is shown by a color code in meters per second. The wind speed on this particular day was rather strong, and two unusual turbulence features were identified.

was that of tuning the laser output onto the water vapor absorption line centered at 2050.532 nm. Control over wavelength resides in the CW master oscillator of Figure 2.1, and the two etalons included in this laser cavity offer some tunability by rotating the etalons. The wavelength was measured during this tuning by a wavemeter, which offers a precision of 1 pm but at an accuracy suspected to be off by as much as 25 pm.

After much experimentation with the etalon tuning, it was found that the desired wavelength could be hit within 3.5 pm. Accomplishing this was extremely tedious, taking about an hour of etalon adjustments. A need became obvious for a more precise method of control, which is developed in Chapter 3. Furthermore the laser would quickly drift away from it set point, which will later be seen as a significant source of error in the DIAL measurement.

Another problem that arose in making a DIAL measurement with the coherent lidar was in processing the atmospheric return signal. The basis of the processing is to measure the power in the atmospheric return—the amplitude of the spectral feature shown in Figure 2.4. The real-time wind processor of Figure 2.5 did not have a capability to measure power, so an alternate design was conceived based on an RF spectrum analyzer as shown in Figure 2.7. The spectrum analyzer, a common laboratory instrument for characterizing electronic signals, was used as a means to detect power within a narrow spectral range. The center of this spectral range was set at 105 MHz, the intermediate frequency of the heterodyne signal, with a passband of 3 MHz. One disadvantage of this technique is that velocity shifts can push the heterodyne signal out of the passband. This problem was avoided by either directing the beam perpendicular to the wind direction or by directing the beam vertically. In either of these cases, the line-of-sight velocity is zero, so there is no Doppler shift. The amplitude measured by the

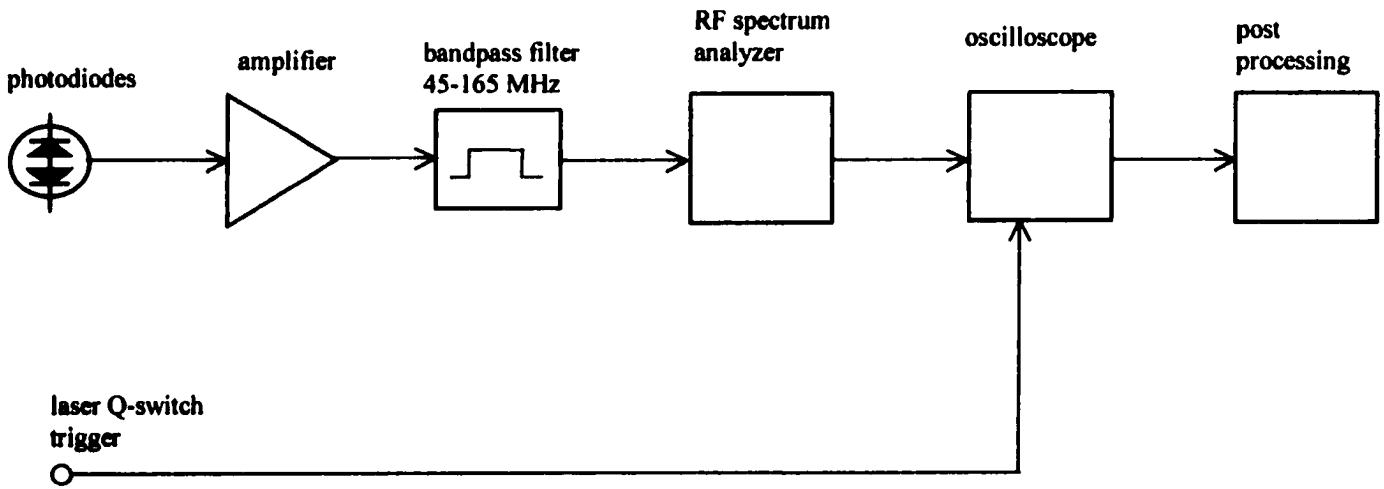

Figure 2.7: Block diagram of DIAL data acquisition.

spectrum analyzer is fed into an oscilloscope. By triggering the oscilloscope with the laser pulse, a plot of atmospheric return versus range results. Data from the oscilloscope was then transferred to a personal computer where DIAL calculations were made.

The procedure for making a DIAL measurement began with tuning the CW master oscillator as close as possible to absorption line center. The atmospheric returns from 100 laser pulses were then averaged and recorded. As quickly as possible, but still requiring several minutes to accomplish, the laser was tuned off line by tilting the etalons of the master oscillator. The resulting wavelength was 2051.934 nm. One hundred shots were again averaged and recorded to create the off-line measurement. In this initial testing of DIAL performance it was desired to probe an atmosphere of known water vapor concentration. A vertical measurement was thus ruled out, since water vapor content varies strongly with altitude. A horizontal profile is a better choice as the water vapor concentration should be approximately uniform with range, and if made near the ground could be compared with conventional single-point humidity and temperature measurements at weather stations. It should be noted that a horizontal lidar measurement would ordinarily be considered hazardous, as people could encounter the beam and suffer ocular injury. However, due to the 2 μm wavelength and pulse characteristics of this lidar, there is no potential for such damage. This laser safety consideration was reviewed and approved by protocols established at NASA Langley Research Center, where these measurements were made.

Two problems were encountered in attempting to make a correlative lidar/weather-station measurement. First, a horizontal path was not possible due to trees located about 320 m away. The lidar beam was instead elevated at 15° above horizontal to clear the tree tops. Second, the nearest correlative measurement weather station was located at Norfolk

International Airport, some 25 miles distant from the laboratory. Some variation in humidity is to be expected over such a long distance.

Figure 2.8 shows the results of the DIAL measurement. Data before 200 m range is not displayed since the detector is still saturated by the internal scatter pulse. Both the on-line and off-line returns drop off with range, as expected from the simulation of Figure 1.2. But the on-line return falls at a faster rate than the off-line return, as is expected from the simulation of Figure 1.4. This difference in attenuation rate contains the information on water vapor concentration. These return signals are both characterized by jagged features associated with the variation of aerosol concentration with range. Ideally both the on-line and off-line returns would have the same peaks and valleys. But this is not the case of Figure 2.8 because there is a long time, about five minutes, between the on and off measurements. During this time the aerosol distribution in the atmosphere changes.

In an attempt to average out these differences the backscatter profiles of Figure 2.8 were smoothed. Figure 2.9 shows these smoothed profiles out to a range of 1500 m, at which point the signals levels have decayed well into background noise. The ordinate units of Figure 2.9 have changed from those of Figure 2.8 because linear units lend themselves to the DIAL calculation presented in Equation 1.15. Four points indicated on Figure 2.9 were used for a DIAL calculation with the resulting water vapor concentration found to be 5.2×10^{17} molecules/cm^3; the concentration based on weather station measurements of 21.1°C and 45% relative humidity is 2.8×10^{17} molecules/cm^3. If the weather station data is accepted as truth then the DIAL measurement has an 86% error.

A lack of geographical proximity between the lidar and weather station account for some of this error, but three major problems within the lidar that would limit DIAL

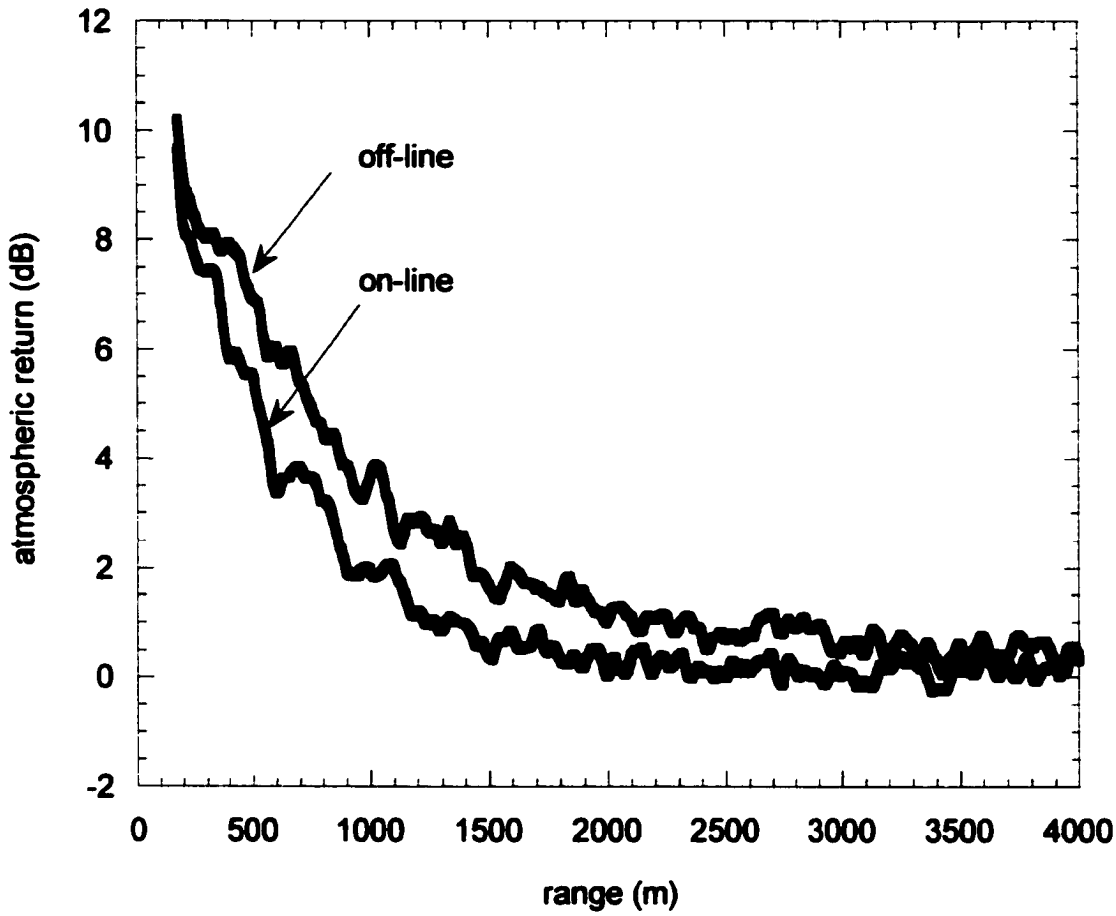

Figure 2.8: Water vapor DIAL measurements.

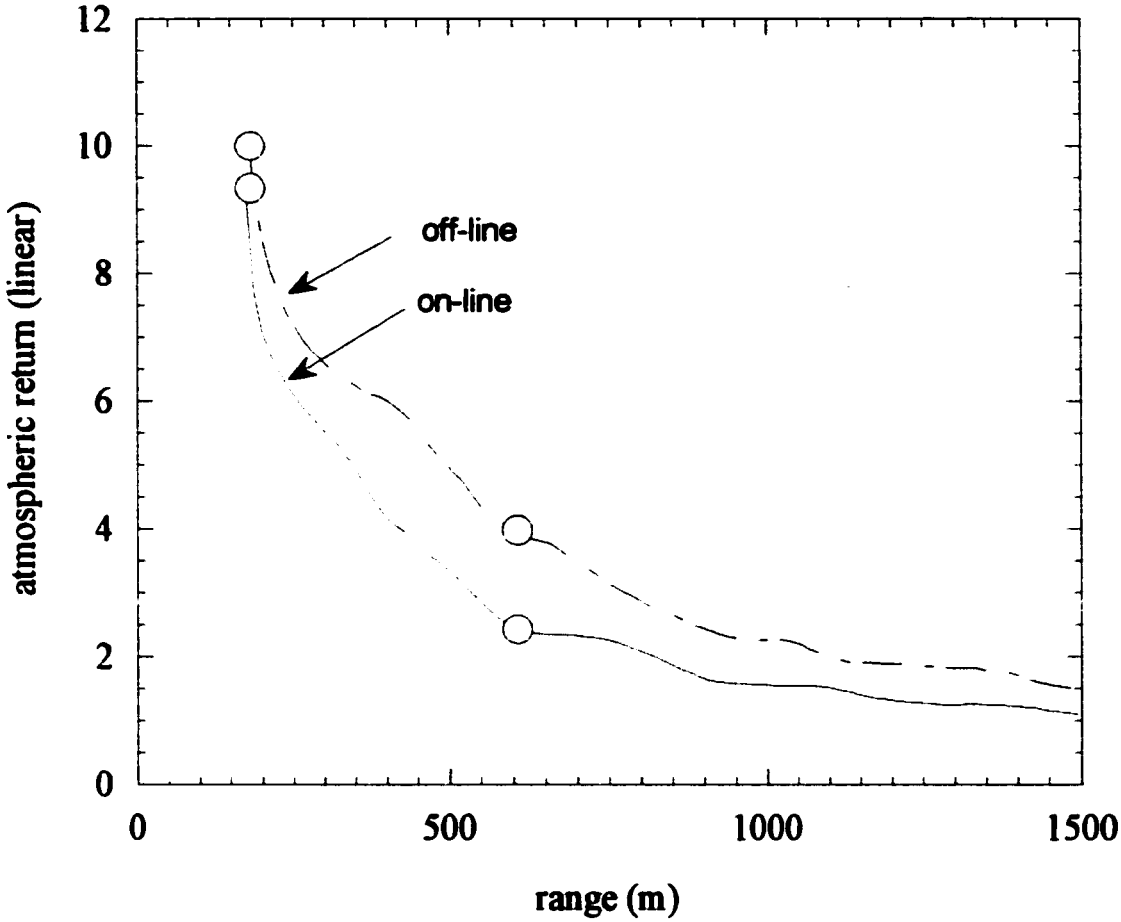

Figure 2.9: Smoothed water vapor DIAL measurement. The four points indicated were used for a DIAL calculation.

measurement accuracy became apparent in the course of this experiment. First, a higher SNR would allow for a less ambiguous determination of signal strength to use in the DIAL calculation. SNR could be increased with a stronger pulse energy or more sensitive receiver. The second problem encountered was a long time interval between the on-line and off-line measurements, during which time the atmosphere changed conditions. The solution to this problem is to develop a means to quickly switch from one wavelength to the other. Ideally the on-line and off-line wavelength would be alternated with every laser pulse, interleaving on and off-line measurements for 200 pulses. The alternate pulse would be separated by the data acquisition system for averaging and subsequent calculation. The third problem faced was that of wavelength uncertainty and drift.

Wavelength uncertainty and drift is believed to the biggest error source. The laser was judged to be on line center by measuring its wavelength on a wavemeter, which may have an error of up to 25 pm. The tunability of the CW master oscillator was also not fine enough to tune onto the peak absorption of the line—tuning only as close as 2.5 pm was achieved. Furthermore, the laser could easily have drifted as much as 2 pm over the time during which the measurement was made. All of these uncertainties could make the laser wavelength as much as 30.5 pm away from where it was thought to be. The calculation of concentration from Figure 2.9, however, assumes a differential absorption cross-section with the laser tuned to the peak absorption. At 30.5 pm away from line center, the absorption strength is almost at the half-maximum of the absorption line, as indicated by the data of Figure 1.3. As a result, the uncertainty and drift in wavelength can cause a 50% over estimation of the water vapor concentration. The solution to this problem requires that a fine control be established over the CW master oscillator and that

a technique be developed for stabilizing the laser wavelength onto line center. A summary of the CW master oscillator requirements is presented in Table 2.1.

The following chapter describes the re-design of the CW master oscillator to meet these requirements. Chapters 4 and 5 then describe how the laser is stabilized to absorption lines of both carbon dioxide and water vapor. The rest of this dissertation describes a second-generation lidar based on this improved master oscillator, in which improvements will be shown in DIAL accuracy performance.

Coarse Tuning: Range > 2 nm and including absorption line of gas of interest. Resolution < 10 pm
Fine Tuning Range > 10 pm Resolution < 1 pm
Spectrum: single frequency
Linewidth < 1 MHz
Power > 20 mW
Frequency Stability: less than 1 pm over 1 hour.

Table 2.1: Continuous-wave master oscillator requirements.

CHAPTER 3

MASTER OSCILLATOR LASER DESIGN AND CHARACTERIZATION

This chapter describes how the CW master oscillator of Chapter 2 was redesigned to be precisely tunable over the narrow spectral width of absorption lines. The basic idea behind this design is to get a better understanding of the etalon-based coarse tuning and to add a piezo-electric translator (PZT) to make small changes in the laser cavity length for fine tuning. But in order to make these modifications successful, the laser design must be considered in its entirety. A detailed design is presented in this chapter, beginning with the physical properties of Ho:Tm:YLF in Section 3.1 and its spectroscopic properties in Section 3.2. Section 3.3 describes the cavity design of the master oscillator, and Section 3.4 presents the laboratory characterization of the laser.

The first reported study of holmium toward use as a laser material was a spectroscopic evaluation in 1962 by Johnson et al. of a Ho:$CaWO_4$ crystal.[28] The first report of laser action of holmium in a yttrium lithium flouride host was by Remski in 1969, using flashlamp pumping and liquid nitrogen cooling of the crystal to 77K.[29] Laser performance was improved in the 1970s with advances in higher power output and tunability.[30] In the 1980s further improvements were realized with pumping by semiconductor diode lasers and running the lasers with thermo-electric cooling close to room temperature. The first reported diode-pumped near room temperature Ho:Tm:YLF laser was made by Hemmati in 1989.[31] Taczak and Killinger developed a tunable Ho:Tm:YLF laser than could be continuously scanned over 6 cm^{-1} centered in a spectral range that includes carbon dioxide and water vapor.[32] While these recent advances offered

a desirable tunability, none of them are of a single-frequency spectrum required for coherent lidar.

Single-frequency Ho:Tm:YLF lasers have been developed for coherent lidar applications, such as the master oscillator described in the previous chapter, but lacking the tunability required for DIAL. Aside from the etalon-narrowed design discussed in Chapter 2, single-frequency Ho:Tm:YLF lasers have also been demonstrated in a microchip configuration that could be finely tuned by temperature.[33] This design, however, lacked a coarse tunability so that its fine tuning range could be centered over an absorption line. Similarly, both Hale et al. and McGuckin et al. developed PZT-tuned etalon-narrowed Ho:Tm:YLF lasers that could be finely tuned but not coarsely tuned over absorption lines.[34,35] The goal of this chapter is to synthesize all of the required traits for single-frequency spectrum, wide tunability to the center of absorption lines, and fine tunability across the narrow width of these lines.

It should also be noted that holmium and thulium can be used in other host materials such as YAG and LuAG.[36,37] Furthermore, thulium in YLF and other hosts will also lase at wavelengths around 2 μm. None of these alternate configurations, though, has met the requirements for a coherent DIAL application. Ho:Tm:YLF is preferred over these other configurations as it has the most promise for high-energy pulsed operation.

3.1 Physical Characteristics of Ho:Tm:YLF

The Ho:Tm:YLF laser crystal is based on a lattice host of yttrium lithium flouride, whose properties will be discussed in this section. The elements holmium and thulium are substituted into some of the YLF lattice sites, hence YLF is called the host material.

Holmium, a rare earth element, is the laser gain medium with the energy levels allowing the two micron wavelength. Holmium unfortunately does not possess energy levels of wavelengths convenient for optical pumping, so thulium is included to facilitate pumping. Thulium has strong absorption characteristics at wavelengths amenable to pumping with diode lasers. Thulium then transfers energy to the holmium in a process discussed in the following section.

Most of the physical properties of the Ho:Tm:YLF crystal are those of the undoped YLF crystal, since the doping levels are not very high. For example, the CW master oscillator described in Chapter 2 has a doping of 6% of the crystal lattice sites replaced by thulium and 0.3% of the sites replaced by holmium. YLF is of tetragonal scheelite crystalline structure (diagrammed in Figure 3.1), placing it in the C_{4h} point group.[38] This crystal structure is uniaxial, so different properties can be expected for the two orthogonal crystal axes, referred to as a and c.

The general properties of the YLF crystal are given in Table 3.1. YLF makes a good laser host material because these properties imply good performance optically and mechanically. For example, the hardness, moduli, and thermal conductivity are favorable for handling a high level of pump energy. The optical properties in absorption loss, scattering, and index of refraction also make YLF a good laser material. Another characteristic of a good host material is ease of crystal growth and processing. The Ho:Tm:YLF crystals are grown in the form of a boule by Czochralski techniques similar to growing silicon or gallium arsenide for semiconductor applications.[40]

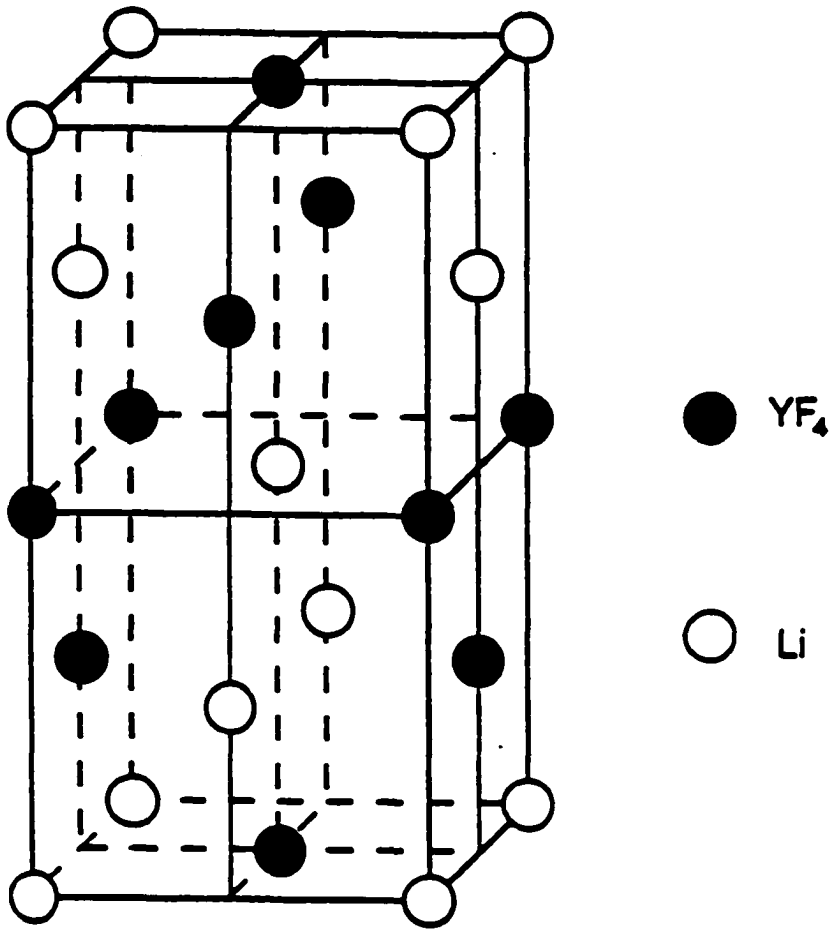

Figure 3.1: Crystal structure of yttrium lithium fluoride. The unit cell dimensions are a = 5.2 A and c = 10.7 A. From Shaw.[39]

Crystal System/Space Group:	Unit Cell Dimensions (A)	Molecular Weight	Density (g/cm^3)
Tetragonal	a = 5.175	171.84	3.968

Room Temperature Elastic Constants

subscripts of stiffness (s)(Gpa) or compliance (c)(Tpa^{-1})

	11	12	13	16	33	44	66
c	121	60.9	52.6	-7.7	156	40.9	17.7
s	12.8	-6.0	-2.3	8.16	7.96	24.4	63.3

Mechanical Properties

Moduli (Gpa)

Elastic	85
Shear	32
Bulk	81
Poisson's Ratio	0.32
Flexure strength	35
Knoop Hardness (kg/mm^2)	300

Thermal Properties

Melt Temperature 1092 K

Heat Capacity 0.79 J/g K

Thermal Expansion (10-6/K) 13.3 parallel to a
8.3 parallel to c

Thermal Conductivity 6.3 W/m K at 300 K

Optical Properties

Transparency

UV 0.18 mm

IR 6.7 mm

Refractive Index (n) 1.447
1.469

Thermo-Optic Coefficients (10^{-6}/K)

λ (μm)	dn/dT
0.436	-0.54 (o)
	-2.44 (e)
0.546	-0.54 (o)
	-2.44 (e)
0.578	-0.54 (o)
	2.44 (e)

Dispersion Formula (λ in μm)

Valid range: λ = 0.23 to 2.6 μm

$$n_o^2 = 1.38757 + \frac{0.70577\lambda^2}{\lambda^2 - 0.00931} + \frac{0.18849\lambda^2}{\lambda^2 - 50.99741}$$

$$n_e^2 = 1.31021 + \frac{0.84903\lambda^2}{\lambda^2 - 0.00876} + \frac{0.53607\lambda^2}{\lambda^2 - 134.9566}$$

Table 3.1: Mechanical, thermal, and optical properties of yttrium lithium flouride (YLF).[41]

3.2 Spectroscopic Properties of Ho:Tm:YLF

While the physical properties of Ho:Tm:YLF are largely determined by the host material, the spectroscopic and laser gain properties are determined by the activator, holmium, and sensitizer, thulium. The host does, however, influence the spectrum of the laser gain. The host crystal lattice imposes an electric field to which the dopants are subjected, causing the pump and laser energy levels to split into a manifold by the Stark effect. Different crystal hosts such as YAG, YLF, or LuAG have different crystal properties which Stark split the energy levels in different ways. The result is that the selection of the host can shift the wavelength range of the laser transition. For example, Ho:Tm:YLF offers laser gain between 2047 and 2070 nm, while Ho:Tm:YAG offers gain between 2088 and 2105 nm.[42]

Laser action in Ho:Tm is complicated to analyze when compared to its more commonly encountered rare earth cousin neodymium. In a neodymium laser the same atom both absorbs the pump energy and provides stimulated emission, but in Ho:Tm the thulium atoms absorb the pump and the holmium atoms provide stimulated emission. As will be shown in this section, pump excitation is transferred from the thulium to holmium by several mechanisms. Neodymium makes a good laser material because it is a so-called four level system in which its lower laser level is well above the ground state and decays very quickly. This is in contrast to the Ho:Tm system in which the lower level is a ground state manifold that has a significant thermal population. Hence, cooling the Ho:Tm:YLF increases the laser power output by depopulating the upper levels of the lower state manifold.

The energy levels associated with Ho:Tm are shown in Figure 3.2. These levels are actually manifolds, which Ashurov et al. studied spectroscopically to determine the range of energies within each manifold.[43] Pumping occurs from the thulium $^3H_6$ ground state to the $^3H_4$ level, at a wavelength that can be effectively matched by a diode laser pump source in the 790 nm range. After pump energy is transferred to holmium, laser action takes place between the holmium $^5I_7$ to $^5I_8$ level. Several mechanisms are involved in the transfer of pump energy to the holmium $^5I_7$ upper laser level.

The first process to consider is quenching of the thulium $^3H_4$ level which has accepted the pump excitation. Quenching is a process by which the pump excitation decays toward lower levels which will hopefully fill the upper laser level. Decay from the $^3H_4$ level occurs among pairs of thulium atoms that are coupled together by their close proximity in the crystal lattice, resulting in a mechanism called cross relaxation.[44] One form of cross relaxation takes place with one thulium atom in the $^3H_4$ manifold and the other in the $^3H_6$ ground state. As the quantum in the $^3H_4$ state relaxes the quantum in the $^3H_6$ becomes excited, with the result that both atoms have a quantum in the $^3F_4$ manifold. This presents a curious phenomenon where there is a quantum efficiency of two—one excited quantum in $^3H_4$ results in two excited quanta in $^3F_4$. Cross relaxation also feeds the $^3F_4$ level after decay of the $^3H_4$ level to $^3H_5$.

The second energy transfer process to consider is how the $^5I_7$ upper laser manifold becomes populated. The primary mechanism for filling the $^5I_7$ level is by energy transfer from the thulium $^3F_4$ state. A secondary process also occurs in a cross relaxation from thulium to holmium atoms, in which a thulium atom relaxes from $^3H_4$ to $^3H_5$. During this thulium relaxation a nearby holmium atom receives a promotion from $^5I_8$ to $^5I_7$.

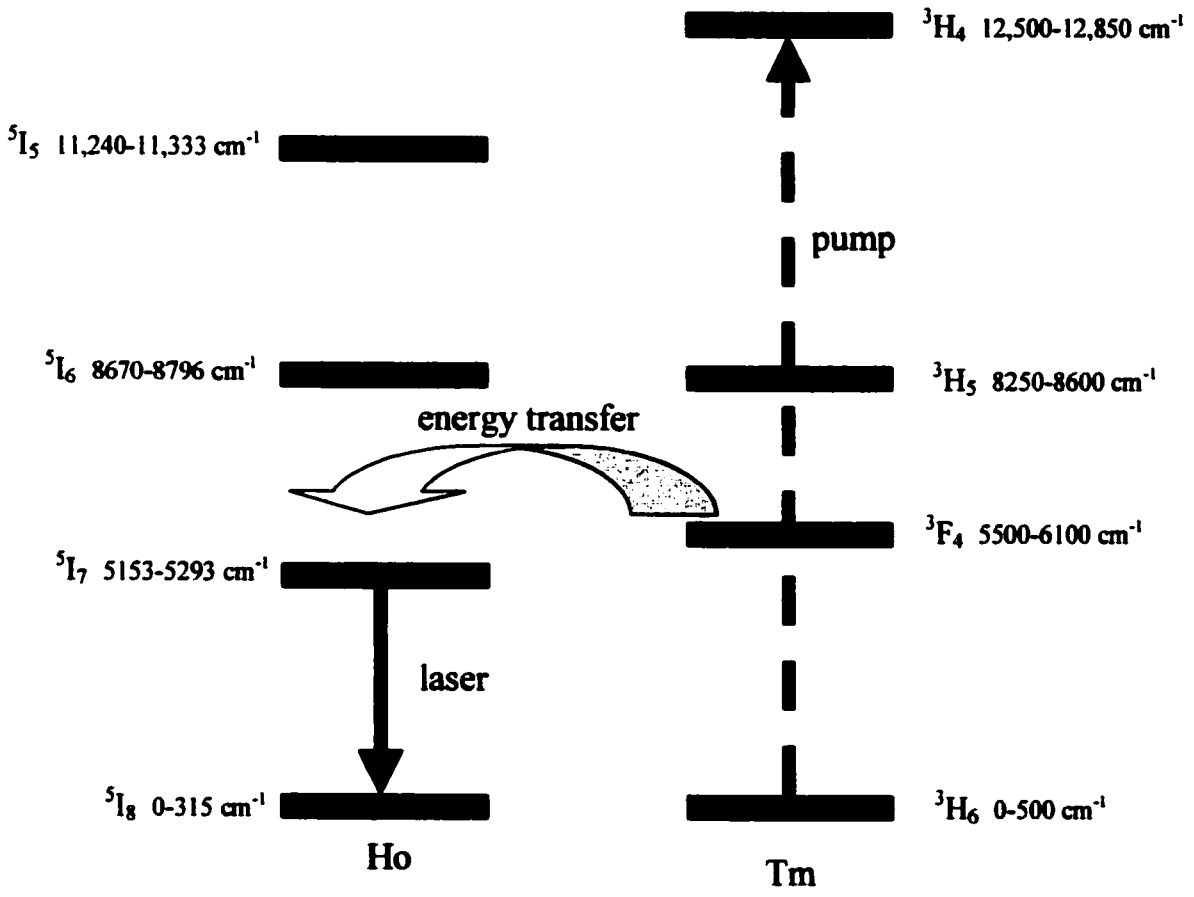

Figure 3.2: Energy levels and transitions associated with laser action in Ho:Tm:YLF.

The third energy process involved is a loss mechanism called up conversion that depletes the $^5I_7$ upper laser level. Cross relaxation was seen to be beneficial in quenching the upper laser level pumping, but it has deleterious consequences in up conversion. Up conversion starts with the relaxation of a thulium atom in $^3F_4$ to $^3H_6$ with a concomitant promotion of a nearby holmium atom from $^5I_7$ to $^5I_5$. A quantum in the upper laser level has been lost, which may or may not return to $^5I_7$. No loss to the population would occur if the $^5I_5$ state undergoes a reverse process back to $^5I_7$. But a loss does occur if the $^5I_5$ state decays to $^5I_6$ and subsequently cross relaxes with thulium levels. The transition from $^5I_5$ to $^5I_6$ is radiative at a visible yellow-green wavelength.

An analysis of laser action in the Ho:Tm system can be made by considering it as a four-level system, as diagrammed in Figure 3.3. Even through the lower laser level is in the ground state, the assumption of a four-level laser is reasonable based on the fact that cooling of the laser crystal is employed to reduce the Boltzman distribution to the lower levels of the manifold.[43] Analysis of the spectroscopic results of Ashurov et al. indicate that the laser transitions of interest around 2.05 μm terminate for energies above 275 cm^{-1} in the $^5I_8$ manifold. The temperature of the laser makes the lower laser level largely unpopulated. That is, the thermal population is at

$$E = kT \quad , \quad (3.1)$$

with corresponding wavelength

$$\lambda < \frac{hc}{kT} \quad . \quad (3.2)$$

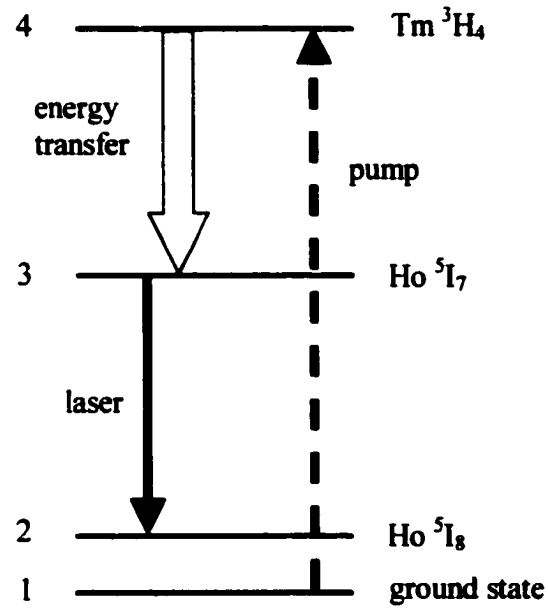

Figure 3.3: Four-level laser representation of the Ho:Tm system.

In Equation (3.1) and (3.2) k is Boltzman's constant, h is Planck's constant, c is the speed of light, and T is the temperature of the crystal. For the –39°C temperature maintained for the laser the associated wavelength is less than 162 cm^{-1}. Hence, it can be assumed that the lower laser level is well above the thermal population of the lower state within the $^5I_8$ manifold.

A set of representative rate equations can be written to investigate laser performance:

$$\frac{dN_4}{dt} = -\frac{N_4}{\tau_4} + R_p(N_1 - N_4) \quad , \qquad (3.3)$$

$$\frac{dN_3}{dt} = \frac{N_4}{\tau_{43}} - \frac{N_3}{\tau_3} \quad , \qquad (3.4)$$

$$\frac{dN_2}{dt} = \frac{N_4}{\tau_{42}} + \frac{N_3}{\tau_{32}} - \frac{N_2}{\tau_{21}} \quad , \qquad (3.5)$$

$$\frac{dN_1}{dt} = \frac{N_2}{\tau_{21}} - R_p(N_1 - N_4) \quad , \qquad (3.6)$$

where N_i represents the population density of the ith level, τ_{jk} is the decay time from level j to level k, and τ_m represents the total decay time from level m. For example

$$\frac{1}{\tau_4} = \frac{1}{\tau_{41}} + \frac{1}{\tau_{42}} + \frac{1}{\tau_{43}} \quad . \qquad (3.7)$$

In this analysis the laser is operating at a steady-state condition above threshold, and the populations of the four levels do not change. The rate equations then become:

$$N_4 = \frac{R_p \tau_4}{1 + R_p \tau_4} N_1 \quad , \quad (3.8)$$

$$N_3 = \frac{\tau_3}{\tau_{43}} N_4 \quad , \quad (3.9)$$

$$N_2 = \tau_{21}\left(\frac{N_4}{\tau_{42}} + \frac{N_3}{\tau_{32}}\right) \quad , \quad (3.10)$$

$$N_1 = \frac{N_2}{\tau_{21} R_p} + N_4 \quad . \quad (3.11)$$

Following the approach of Siegman, two useful dimensionless quantities can be defined.[44] First, a quantity is assigned as

$$\beta = \frac{\tau_{21}}{\tau_{32}} + \frac{\tau_{43}\tau_{21}}{\tau_{42}\tau_3} \quad . \quad (3.12)$$

In a good laser material the excitation in the pumped level will mostly go toward filling the upper laser level. That is, τ_{42} goes to a value that makes the second term in Equation (3.12) negligible compared to the first, making

$$\beta \approx \frac{\tau_{21}}{\tau_{32}} \quad . \quad (3.13)$$

Another attribute of a good laser gain material is that the lower laser level will decay more quickly than the upper laser level is filled. For example in the Ho:Tm system τ_{32} is approximately 5 ms and τ_{21} is less than 1 μs. This desirable condition makes $\beta << 1$. The second quantity suggested by Siegman is called the fluorescent quantum efficiency:[44]

$$\eta = \frac{\tau_4}{\tau_{43}} \frac{\tau_3}{\tau_{32}} \quad . \quad (3.14)$$

Manipulation of Equations (3.8) through (3.14) gives an expression for the population inversion:

$$\frac{N_3 - N_2}{N} = \frac{(1-\beta)\eta R_p \tau_{32}}{1 + \left(1 + \beta + \frac{2\tau_{43}}{\tau_{32}}\right)\eta R_p \tau_{32}} \quad , \qquad (3.15)$$

where an additional relationship has been brought in describing the total population density:

$$N = N_1 + N_2 + N_3 + N_4 \quad . \qquad (3.16)$$

Further simplification is facilitated by assuming that good laser characteristics make τ_{43} very small and β approach zero. Equation (3.15) then reduces to

$$\frac{N_3 - N_2}{N} \approx \frac{R_p \tau_{32}}{1 + R_p \tau_{32}} \quad . \qquad (3.17)$$

With a relationship established for the population inversion, an analysis can be made of the intensity output expected from the laser. Following the approach of Verdeyen for a standing-wave high-Q resonator, the laser output intensity can be written as[45]

$$I_{out} = \frac{I_s}{2}\left[(1 - R_2)\left(\frac{\gamma \ell}{\alpha} - 1\right)\right] \quad . \qquad (3.18)$$

I_s is the saturation intensity

$$I_s = \frac{h\upsilon}{\sigma_{se}\tau_{32}} \quad , \qquad (3.19)$$

where hν is the photon energy, and σ_{se} is the stimulated emission cross section. R_2 in Equation (3.18) represents the reflectivity of the output coupler. The fraction $\gamma\nu/\alpha$ shows the competition between gain and loss in the cavity with crystal length l. The numerator and denominator of this ratio can be calculated by

$$\alpha = \ln\left(\frac{1}{R_1 R_2}\right) \quad , \qquad (3.20)$$

$$\ell = (N_3 - N_2)\sigma_{se}\ell_g \quad , \qquad (3.21)$$

where R_1 is the reflectivity of mirror 1, usually a high reflector. In this analysis no other losses are represented in the cavity, such as a transmission loss at the facets of the laser crystal. Equation (3.15) can be combined with Equation (3.17) for a representation of the laser output intensity:

$$I_{out} = \frac{h\nu}{2\sigma_{se}\tau_{32}}\left\{(1-R_2)\left[\frac{N\left(\frac{R_p\tau_{32}}{1+R_p\tau_{32}}\right)\sigma_{se}\ell}{\ln(\frac{1}{R_1R_2})} - 1\right]\right\} \quad . \qquad (3.22)$$

In the following sections the design of a continuous-wave laser will be presented, including an experimental assessment of its output intensity. In Section 3.4.1 these experimental results will be compared with a calculation based on Equation (3.22).

A rate equation analysis can also be made for pulsed operation of the laser. Unlike the continuous-wave case, pulsed lasers typically run at near room temperature with flowing water for convective cooling of the laser crystal to quickly dissipate the strong

intensity of pulse pumping. For example, the pulsed laser used in Chapters 6 and 7 is cooled with flowing water maintained at 15°C. In this situation the lower laser level is highly populated, and a three-level laser approach is more appropriate for analysis. As shown in Figure 3.4 the holmium $^5I_8$ lower laser level has blended into the ground state. This ground state is called level 2 to keep the same nomenclature used for the four-level low-temperature analysis.

Rate equations for this three-level representation can be written as

$$\frac{dN_4}{dt} = \frac{-N_4}{\tau_{43}} + R_p(N_2 - N_4) \qquad (3.23)$$

$$\frac{dN_3}{dt} = \frac{N_4}{\tau_{43}} - \frac{N_3}{\tau_{32}} \qquad (3.24)$$

$$\frac{dN_2}{dt} = \frac{N_3}{\tau_{32}} - R_p(N_2 - N_4) \qquad (3.25)$$

Solution of these coupled differential equations is difficult to solve in an analytical fashion, so a numerical approach is taken using the pulsed laser described in Chapter 6 as an example. The pump source, represented in Equations (3.23) and (3.25) as R_p, in this case is modeled as a step response terminating 1 ms after starting. Parameters used in the modeling include τ_{43} = 40 ms, τ_{32} = 5 ms, and a total number density of 5.56x 10^{20} atoms/cm^3. A more detailed description of the laser is found in Chapter 6.

Solution of the rate equations for the population inversion, N_3-N_2, is shown in Figure 3.5. Several features of the laser are manifest in this plot, such as the rapid build up of inversion due to the short lifetime of the transition from level 4 to level 3. Also, the long storage lifetime of level 3 shows in that the inversion is maintained for a relatively long

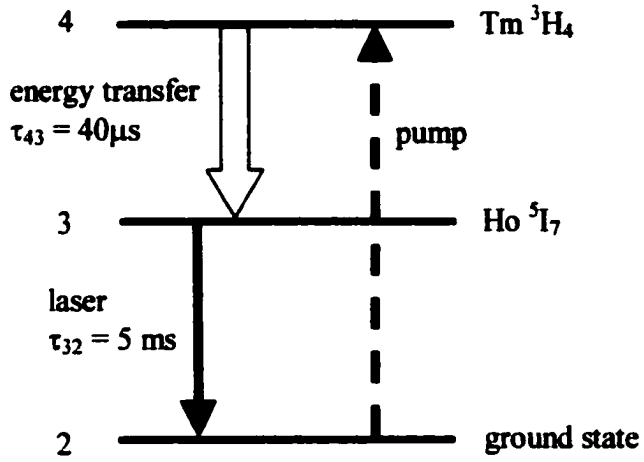

Figure 3.4: Three-level representation of Ho:Tm system at high temperature.

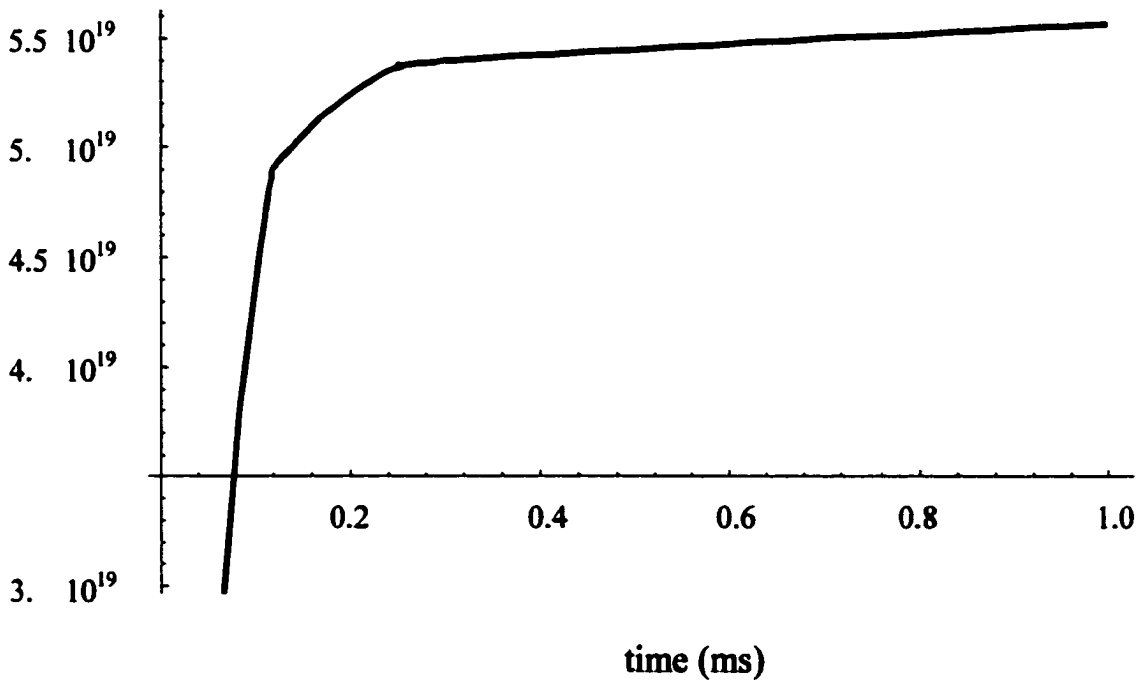

Figure 3.5: Population inversion for a 1-ms long pump pulse.

time, reflecting the fact that Ho:Tm is a good material for energy storage. In this case of a 1 ms long pump pulse, which is the largest that can be applied without risking damage to the pump diode lasers, the inversion builds up to a maximum level of 5.51×10^{19} atoms/cm^3. This inversion is 4.6 times the threshold inversion level, allowing an estimation of the output energy that could be obtained by Q-switching the laser.

Following the analysis of Verdeyen, the Q-switched energy can be calculated by[45]

$$E_Q = \frac{\ln\left(\frac{1}{R_{oc}}\right)}{\ln\left(\frac{1}{R_{oc}T_s}\right)} \frac{\Delta N A \ell h c}{2\lambda} \quad , \qquad (3.26)$$

where R_{oc} is the reflectivity of the output coupler and T_s is the transmission through the Q-switch, accounting for losses through the Q-switch. This first fraction in Equation (3.26) relates the output coupler loss to the total cavity loss. ΔN is the population inversion, A is the area of the laser mode, and l is the length of the laser crystal. The product $\Delta N A l$ thus represents the total number of photons available for laser action. With the inversion calculated from the simulation of Figure 3.5 for the pulsed laser described in Chapter 6, a calculation can be made of the available Q-switch pulse energy. With $R_{oc} = 80\%$ and $T_s = 95\%$, E_Q is found to be 138 mJ. The maximum Q-switched energy actually achieved is 100 mJ, so the modeling has over-estimated the available output. This difference between theory and experiment is attributed to the assumption in the model that all of the pump energy to the thulium $^3F_4$ level goes toward filling the Ho $^5I_7$ upper laser level. In practice some pump energy is lost in cross relaxation and up conversion processes.

A further estimate of laser performance can be made of the pulse width to expect from the Q-switched laser. As suggested by Verdeyen, a knowledge of the inversion can be used to calculate the power contained within the Q-switched pulse:[45]

$$P_{out} = \frac{\ln\left(\frac{1}{R_{oc}}\right)}{\ln\left(\frac{1}{R_{oc}T_s}\right)} \frac{hcA\ell\left\{\Delta N - \Delta N_{th}\left[1 - \ln\left(\frac{\Delta N}{\Delta N_{th}}\right)\right]\right\}}{\lambda\tau_p} \quad , \qquad (3.27)$$

where ΔN_{th} is the inversion required to achieve threshold and τ_p is the photon lifetime for the cavity. The average power in the laser pulse and its energy are related to the laser full-width half-maximum pulse width:

$$\Delta t = \frac{E_Q}{P_{out}} \quad . \qquad (3.28)$$

Applying this calculation to the pulsed laser of Chapter 6 reveals an average power output of 365 kW and a corresponding pulse width of 378 ns. The pulse width actually observed is 190 ns. Inaccuracy of the pulse width calculation is expected since the errors in calculating the pulse energy and output power have already been shown to exist.

The spectroscopy of Ho:Tm:YLF has also been studied experimentally. Podkolzina et al. measured the fluorescence as is reproduced in Figure 3.6.[46] Strong fluorescence is observed in the region from 2047 to 2070 nm, where stimulated emission is of interest between $^5I_7$ and $^5I_8$. The absorption by thulium at wavelengths conveniently accessible by semiconductor diode lasers is shown in Figure 3.7, as measured by Hemmati.[31] The

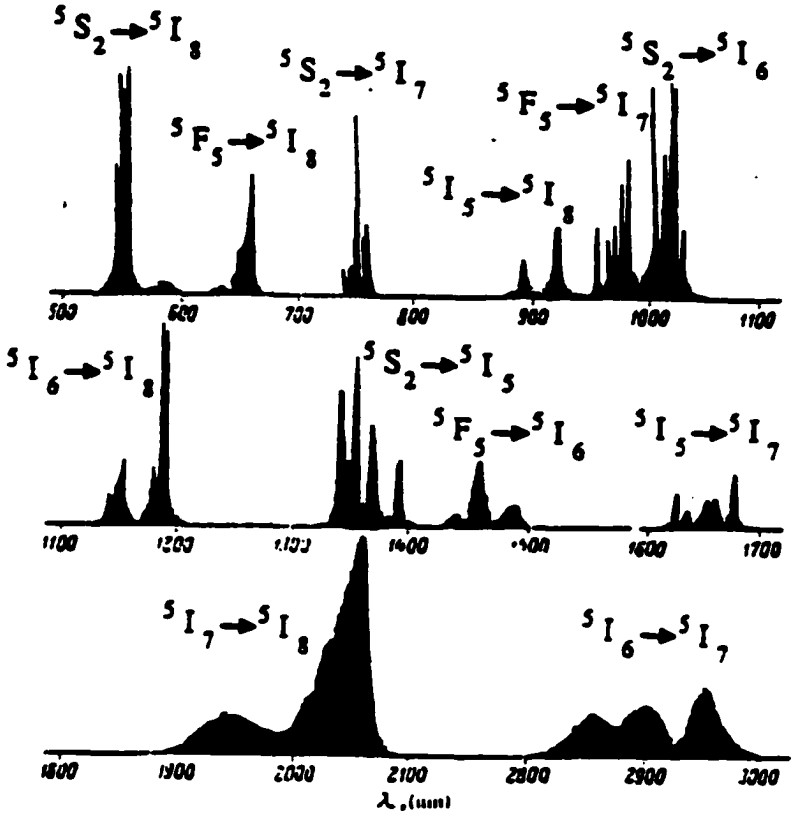

Figure 3.6: The fluorescence spectrum of Ho:Tm:YLF. From Podkolzina et al.[46]

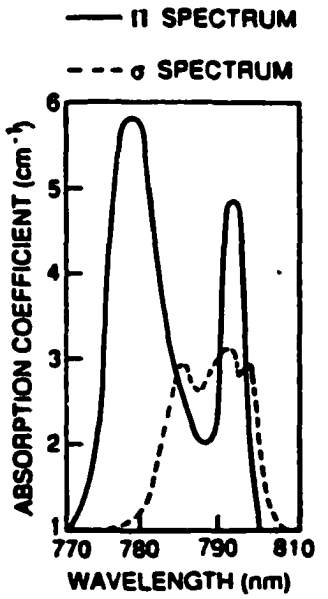

Figure 3.7: The absorption spectrum of Ho:Tm:YLF. σ polarization is parallel to the a axis and π polarization is parallel to c. From Hemmati.[31]

birefringent nature of the crystal manifests itself here in the different absorption characteristics along the orthogonal a and c axes.

3.3 Laser Design

The layout of the CW master oscillator is shown in Figure 3.8. A diode laser provides 1 watt of pump power at 792 nm, which is focused into a 5 mm cubic crystal of 0.3% Ho and 6% Tm. The laser crystal is oriented with the a-axis parallel to the optical axis of the resonator to take advantage of the high-gain c-axis polarized transition. Consequently, absorption of the pump may occur through either a or c-axis polarizations. A thermo-electric cooler is used to hold the crystal temperature at –37°C. The cavity resonator is formed by a high reflection (HR) coating on the end of the crystal and a 20 cm radius of curvature mirror mounted on a piezoelectric translator (PZT). Two etalons, one 1 mm thick and coated 40% reflectivity and another 66 μm thick and uncoated, are used to select and tune a single-mode output.

In the following subsections particular features of the design will be analyzed including the cavity mode calculations in 3.3.1, coarse tuning by etalon tilting in 3.3.2, and fine tuning by PZT motion in 3.3.3

3.3.1 Laser Cavity Design

The design of the laser cavity requires a choice of cavity length and mirror curvatures. A flat mirror is selected for the HR coating on the laser crystal, as curved crystal facets are difficult to manufacture. Choice of the output coupler curvature depends

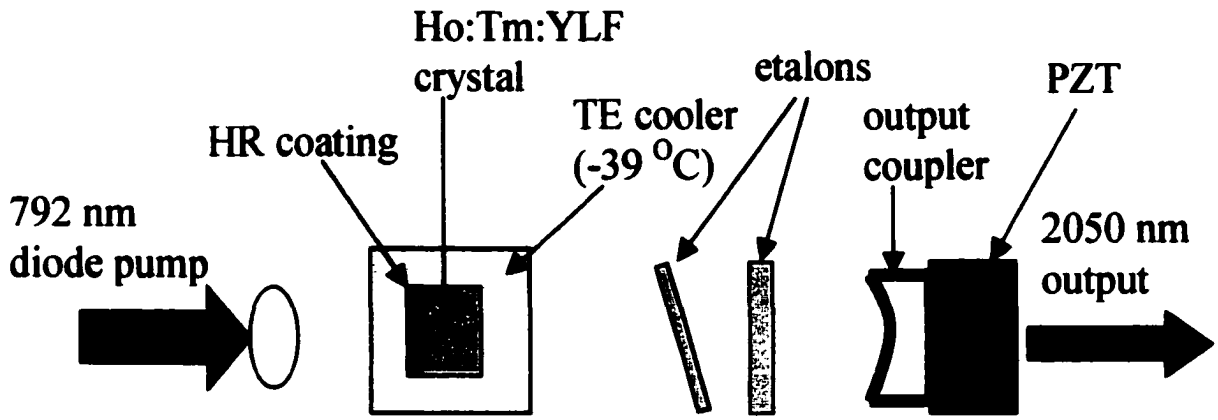

Figure 3.8: Layout of the Ho:Tm:YLF laser. The cavity length from high reflector (HR) to output coupler is 10 cm. A piezo-electric translator (PZT) moves the output coupler for fine frequency tuning.

on the cavity length, and several factors come into play which influence the selection of cavity length. First, the cavity must be long enough to allow insertion of the two etalons. Second, a shorter length is desirable for smaller package size and insensitivity to alignment. Third and most important, the cavity length sets the free spectral range of the oscillator as seen in the relation

$$\Delta\nu = \frac{c}{2(nl + d)} \quad . \qquad (3.29)$$

Where d is the cavity length from the crystal end facet to output coupler, n in the index of refraction of the crystal, l is the length of the crystal, and $\Delta\nu$ is the free spectral range in hertz. As will be shown in Section 3.3.3, the extent of the fine tuning range by the PZT is limited to a free spectral range of the laser cavity. Combining all of these considerations led to a cavity length choice of 10 cm from the HR crystal surface to output coupler, making the free spectral range 1.47 GHz.

The final design choice is then the output coupler curvature, which determines the mode size within the cavity. The design goal is to make the output beam a TEM_{00} profile, so care must be taken to match the pump volume with the mode structure within the cavity. If the pump volume is significantly larger than the TEM_{00} mode, then higher order spatial modes might be excited. Determination of the cavity mode size was made by a simulation of the laser cavity, as shown in Figure 3.9 after selection of the output coupler radius of curvature to be 20 cm.[46] This model applies the ABCD law in the resonator to track the complex gaussian beam parameters through out the cavity.[47] The size of the beam is calculated from the gaussian beam parameter and plotted versus cavity position. Every

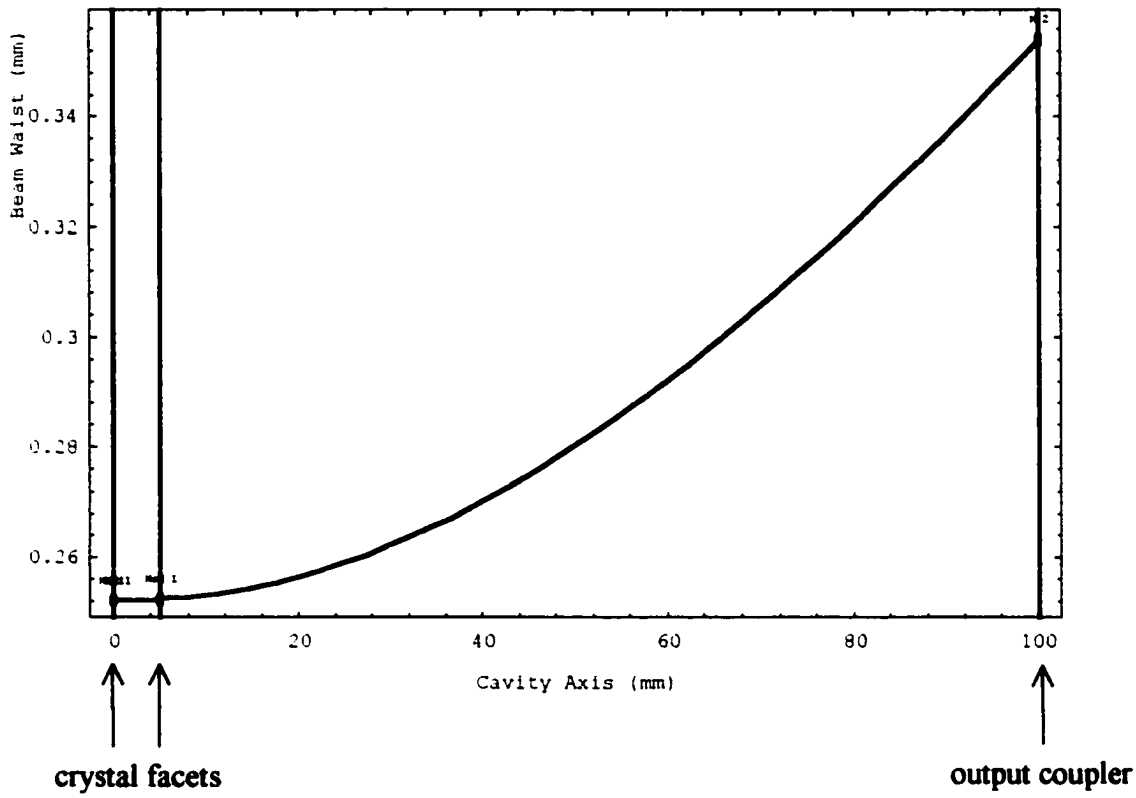

Figure 3.9: Cavity mode plot. The beam waist dimension is the 1/e radius of the electric field.

optical element is represented by a matrix and can therefore be readily changed to optimize the design. Figure 3.9 indicates that the pump beam focused from the diode laser should be kept under 250 μm $1/e^2$ radius throughout the 5 mm length of the crystal. Measurement of the focused pump beam with a knife-edge technique shows the radius to be 200 μm.

This cavity configuration is also attractive in that the TEM_{00} mode size has a small divergence, so that the etalons used for coarse tuning work predictably. Experiments with a hemispherical cavity, in which the mode is especially divergent, showed erratic tuning behavior from the etalons. As will be shown in the following discussion the analysis of etalon tuning is based on an assumption of a collimated source.

3.3.2 Coarse Tuning by Etalon Tilting

Etalons are used as filters inside the laser cavity by taking advantage of their Fabry-Perot resonance peaks. Away from resonance the loss inside the cavity is such that lasing will be suppressed. With a single etalon in the cavity multiple modes could oscillate within the gain spectrum of the laser, with the modes separated by the free spectral range of the etalon. The addition of a second etalon is then used to select a single mode from the modes left behind by the first etalon. An analysis of etalon mode selection can be made by considering the intensity transmitted through an etalon

$$I_t = \frac{1}{1+\frac{4r_{1r}r_2}{(1-r_1r_2)^2}\sin^2\left(\frac{2\pi nd}{\lambda}\right)} \quad , \qquad (3.30)$$

where r_1 is the reflectivity of the front etalon surface, r_2 is the reflectivity of the back etalon surface, n is the index of refraction of the etalon glass, d is the thickness of the etalon, and λ is the wavelength.

This function is plotted in Figure 3.10 for the etalons used in the laser design over the wavelength range where laser gain is of interest. Neither of these etalons is of high finesse—the attenuation off resonance is not particularly strong. This is because a small attenuation is all that is required to suppress lasing. The position of the peak transmission of the etalons can be moved by tilting them, so as to allow lasing at a desired wavelength. Once this wavelength is centered near an absorption line, PZT movement of the output coupler is used for fine tuning over the absorption line.

3.3.3 Fine Tuning by PZT Motion

Fine tuning of the laser wavelength is accomplished by making small changes to the laser cavity length. The output coupler has been attached to a piezo-electric translator (PZT), so that the cavity length can be changed by up to 5 μm. An equation relating PZT motion ΔL, and frequency shift $\Delta\nu$, can be derived by noting that a cavity length change of one half wavelength changes the laser's frequency by one free spectral range. That is,

$$\Delta L = \frac{\lambda}{2} \rightarrow \Delta\nu = FSR = \frac{c}{2(nl + d)} \quad . \qquad (3.31)$$

Thus, a cavity length change of 1.0 μm ($\lambda/2$ at 2 μm) will shift the frequency by 1.47 GHz.

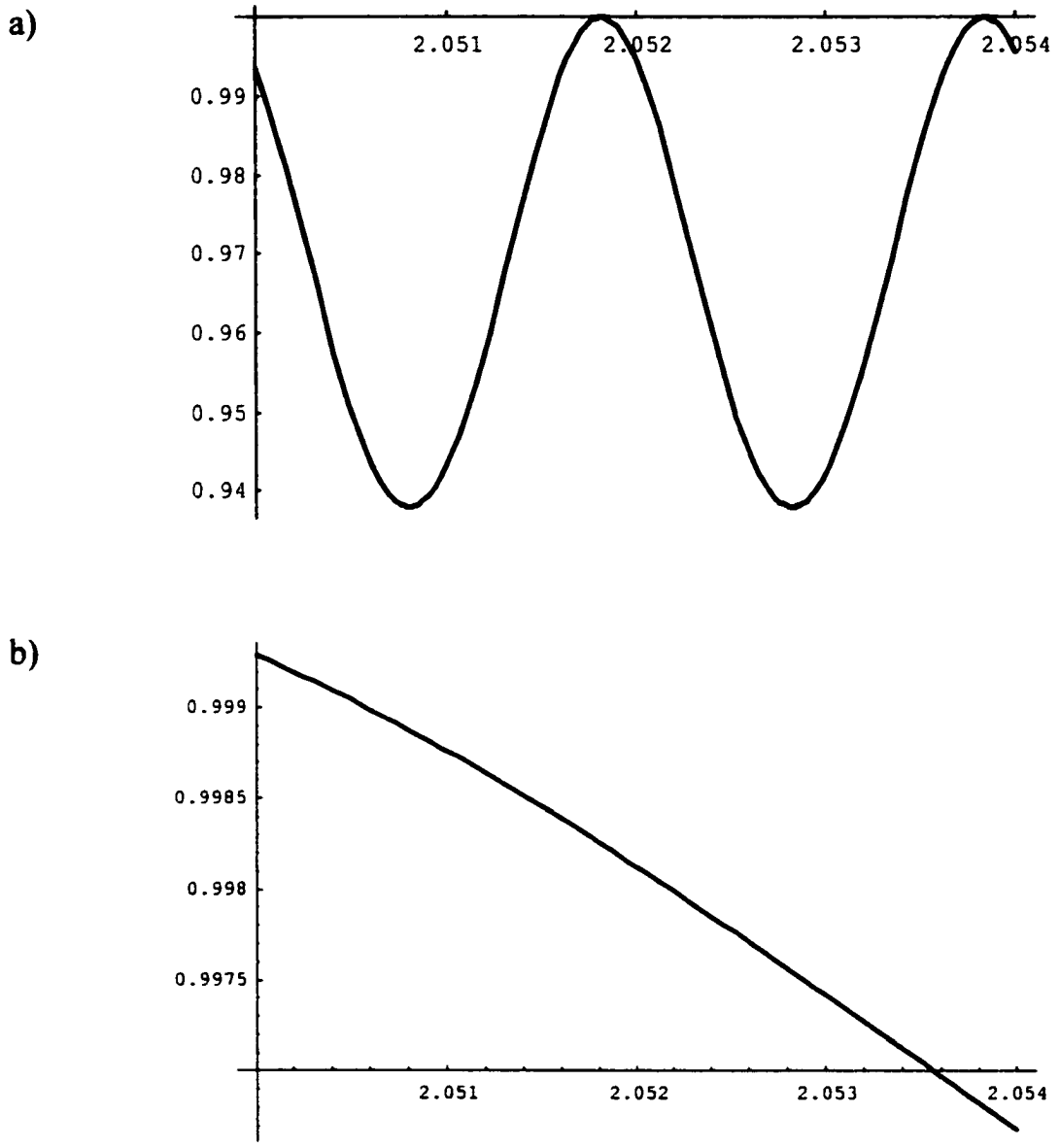

Figure 3.10: Etalon transmissions versus wavelength for a) 1 mm thick etalon with one side 40% reflective and the other side uncoated and b) 66 μm thick etalon with both sides uncoated. Gain is offered throughout the spectral range identified.

Furthermore, tuning beyond one FSR is a limit on the overall fine tuning range. If the PZT pushes the output coupler past 1.0 μm distance then the next longitudinal mode takes over oscillation, and the same wavelength range is encountered. If a greater fine-tuning range were desired, the cavity length could be shortened to decrease the FSR. However, the 1.47 GHz range was intentionally set to trap the laser wavelength close to the absorption line center. Even if the laser experiences a mode hop, the wavelength is still confined to a narrow range around the absorption line center.

3.4 Laser Characterization

Results are presented in this section on the laboratory characterization of the re-designed CW master oscillator. In the following subsections laser performance is reported in power output, wavelength, coarse tuning, fine tuning, and mode structure.

3.4.1 Power Output

The maximum power produced by the laser is 200 mW with a multimode spectrum created when there are no etalons placed in the cavity. Performance in power can be compared to the theoretical prediction of Section 3.2. The parameters pertinent to Equation (3.22) are summarized in Table 3.2, along with comments on how some of these quantities were measured or calculated. Insertion of these values in Equation (3.22) predicts an output intensity of 154 W/cm^2, while the measured power normalized to the crystal mode size shows an actual output of 102 W/cm^2. The over estimation of the theoretical value is attributed to the simplification made in the development of Equation

parameter	representing	value	comments
h	Planck's constant	6.62×10^{-34} J s	
ν	laser frequency	1.46×10^{14} Hz	
σ_{se}	stimulated emission cross section	1.3×10^{-20} cm^2	from reference 49
τ_{32}	upper state lifetime	6 ms	from reference 49
R_1	cavity mirror reflectivity	1	HR mirror formed by coating on crystal facet
R_2	output coupler reflectivity	0.98	
N	total population Density	4.15×10^{19} atoms/cm^3	crystal is composed of 0.3% of YLF atoms replaced by holmium. Crystal density and molecular weight are listed in Table 3.1.
R_p	pumping rate	5.74×10^{19} atoms/s	750 mW incident of crystal with 75% absorption by thulium.
l	crystal length	0.5 cm	

Table 3.2: Parameters used in the calculation of output intensity.

(3.22) in which all of the pump energy is assumed to fill the upper laser level. In reality some of the pump energy is lost in the cross-relaxation and upconversion processes associated with energy transfer from thulium to holmium. A more detailed representation of the Ho:Tm system has been developed by Barnes et al., including quantum mechanical modeling of the various energy transfer processes.[48] This model could perhaps be employed to make a more accurate prediction of laser output intensity. However, the model of analysis of Section 3.2, when coupled to the experimental observations made here, suggests that it can be useful in general analysis of the Ho:Tm system with application of a correction factor of 66% to account for the over-simplification of the model.

Etalons work by imposing a wavelength selective loss, so a drop in power is to be expected when the laser is forced to have a single-frequency spectrum. Furthermore, the loss inside the cavity will depend on wavelength as the transmission through the etalons interacts with the laser gain at the selected wavelength. Figure 3.11 shows how the power output varies with diode pump current with the laser tuned to a wavelength of 2051.983 nm. This wavelength offers the highest output while maintaining a single-frequency spectrum. The threshold for laser oscillation is seen at 1.8 A of diode pump current with a linear increase in power until 2.15 A. The gain begins to saturate after 2.15 A, and by 2.7 A only a small increase in output power is produced by increasing drive current. No data was recorded above 2.7 A, as this is the maximum rated current for this diode laser.

The challenge in the laser design is to make it operate at a precise wavelength corresponding to the peak of an absorption line. The wavelength corresponding to Figure 3.8, where maximum single-frequency power occurs, is not a desired on-line wavelength.

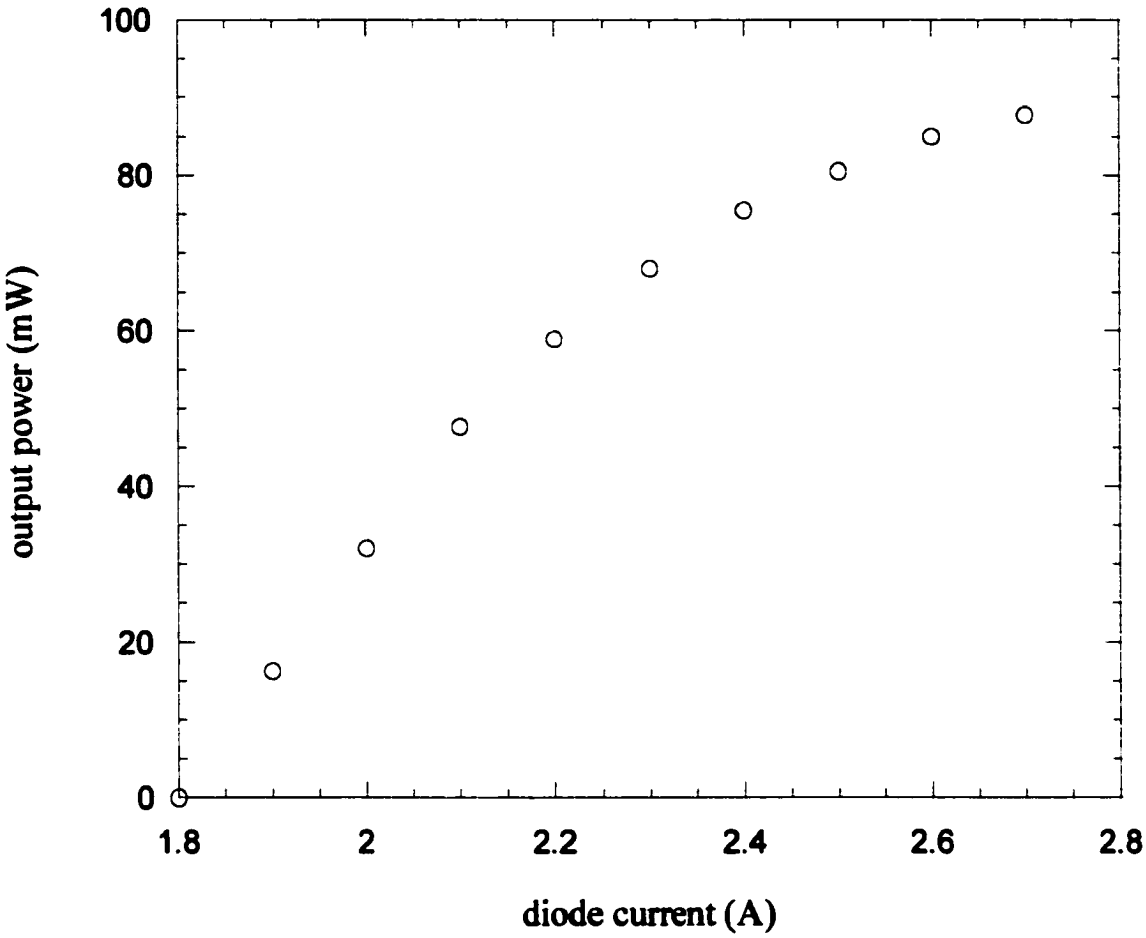

Figure 3.11: Power out versus diode pump current. The spectrum is single frequency at 2051.983 nm.

When tuned to the on-line wavelengths of interest the output power is reduced. At the peak of the water vapor absorption line at 2050.532 nm the maximum power is 45mW, while on carbon dioxide lines at 2050.428, 2052.070, and 2053.204 nm the power is 30, 42, and 20 mW respectively.

3.4.2 Coarse Tuning

Visualization of the longitudinal mode structure was made by coupling the laser beam to a 1-m long Czerny-Turner monochromator with its output slit replaced by an infrared sensitive video camera. The display from the video camera is reproduced in Figure 3.12 for cases without and with etalons. In a) no etalons are inserted in the cavity so a wide swath of modes is seen centered around 2061 nm. Distinct modes can be seen even though this is not expected since the monochromator should not be able to resolve the 1.47 GHz free spectral range of the cavity. Inspection of the observed mode spacing shows it to be 25 GHz, corresponding to an unexpected etalon of 4.3-mm length. This length matches that of the laser crystal, suggesting that the facets of the crystal are acting as a weak etalon. In practice, then, there are actually three etalons in the cavity: two glass etalons and an unintended etalon from the laser crystal.

In Figure 3.12 b) the effect is seen of inserting the 1-mm thick etalon. The loss introduced by this etalon has interacted with the laser gain to favor 2 wavelengths near 2052 nm and one at 2061 nm. The two wavelengths around 2052 are separated by 2 nm as expected from the modeling of Figure 3.10. The job left up to the remaining etalon is to select only one of these modes. Figures 3.12 c) and d) show single-mode oscillation

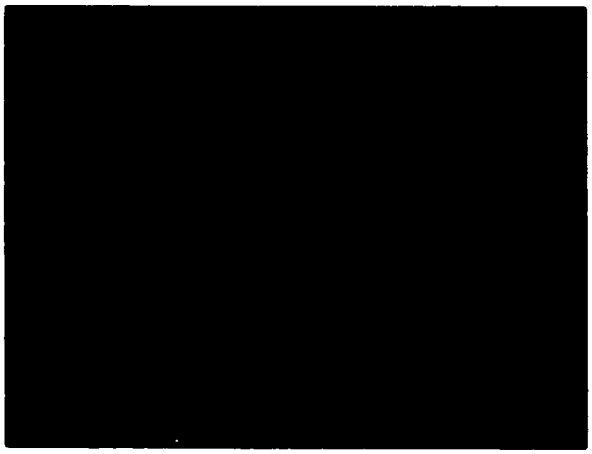

a) no etalons

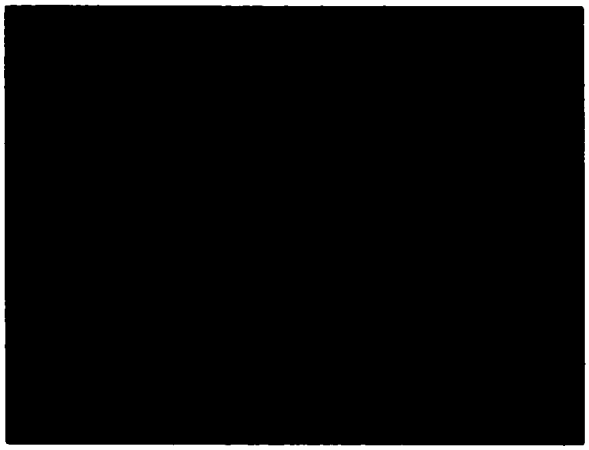

b) thick etalon only

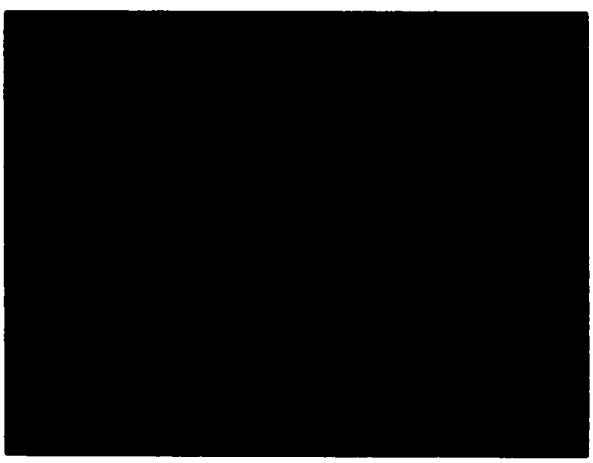

c) both etalons

d) both etalons

Figure 3.12: Spectrum of laser with a) no etalons in the cavity, b) 1mm thick etalon only, c) both etalons in cavity adjusted for single mode mode oscillation at 2050.464 nm, and d) both etalons in cavity adjusted for single mode oscillation at 2053.097 nm.

selected by the thin etalon. By changing the tilt angle of both etalons a wide range of wavelengths can be reached. The tuning, however, is not continuous in that not every wavelength could be reached within the tuning range between 2049 and 2054 nm. This discontinuous behavior is attributed to interference by the unintended etalon created by the laser crystal facets. Evidence of the crystal etaloning effect is seen by changing the temperature of the laser crystal, which in turn tunes the etalon. The range of allowed wavelengths can be altered somewhat by adjusting the crystal temperature. Several desired wavelengths could be reached that correspond to a water vapor absorption line at 2050.532 nm and carbon dioxide absorption lines at 2050.428, 2052.070, and 2053.204 nm.

3.4.3 Fine Tuning

Once the laser wavelength has been coarsely tuned by the etalons in the vicinity of the absorption line, fine tuning by PZT motion of the output coupler is used to resolve features of the absorption line. This fine tuning was characterized by monitoring the wavelength with a wavemeter. Figure 3.13 shows the resulting wavelength measurements as the PZT voltage is increased. A linear tuning is observed over 20 pm (1.5 GHz), before a mode hop occurs. The same range of wavelength is repeated after the hop. The 20 pm range matches the expected tuning range, determined by the cavity free spectral range as calculated in Section 3.3.3.

Before the PZT-tuning characterization of Figure 3.13, the wavelength was coarsely tuned to a wavelength matching an absorption line of carbon dioxide centered at 2053.204 nm. As will be shown in Chapter 4 the absorption lines of interest at low pressure are

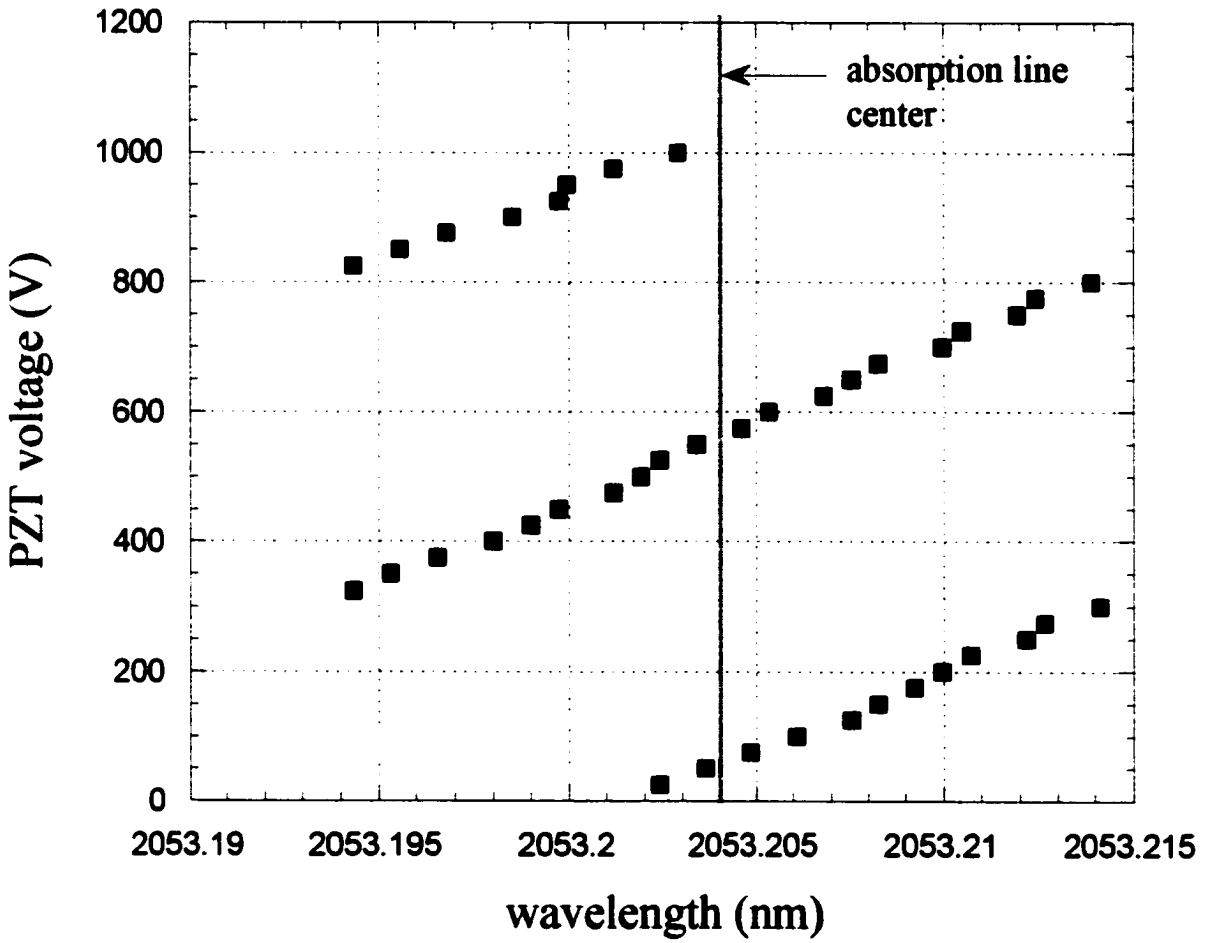

Figure 3.13: Tuning characteristic as piezo-electric translator (PZT) is moved. Two mode hops occur within the 1000 volt range of the PZT

approximately 5 pm wide, so the fine tuning capability is well suited to resolve the center of the absorption line. PZT motion will also be used to modulate the laser for the frequency stabilization technique.

3.4.4 Spatial Profile

The spatial profile of the beam was imaged in order to determine if any high-order spatial modes are oscillating. This measurement was made by removing the lens from an infrared sensitive camera and aligning the camera face to the laser beam. The resulting image of the beam is shown in Figure 3.14, with relative intensities indicated by color. The round, symmetrical shape of the beam indicates that the mode structure is TEM_{00}.

The absence of high-order spatial modes was also verified by focusing the beam onto a 1-GHz bandwidth photodiode. A radio-frequency spectrum analyzer connected to the photodiode would detect beating between the spatial modes, as they oscillate at different frequencies. No such beat signals were detected.

3.4.5 Linewidth

Linewidth is difficult to measure, as there is no instrument available with enough resolution to directly measure the expected sub-megahertz width. A Fabry-Perot interferometer would offer a direct measurement, but the finesse of commonly-available interferometers makes their resolution only 20 MHz. Measurement with such an interferometer was made and indicated the linewidth to be less than 20 MHz.

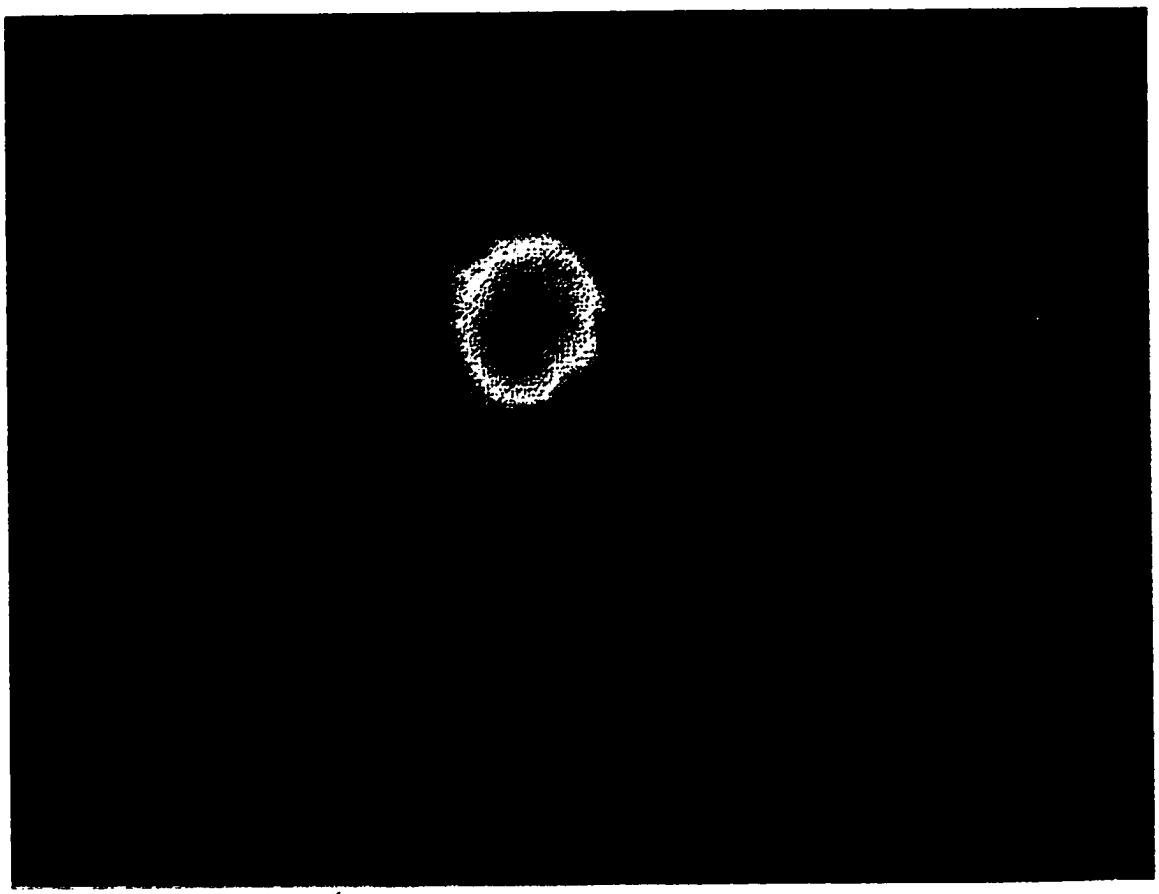

Figure 3.14: Beam profile of CW master oscillator showing TEM_{00} structure.

An alternate linewidth measurement was made by heterodyning with another laser of linewidth known to be less than 200 kHz. This second laser is a Ho:Tm:YLF crystal in a monolithic cavity configuration, in which the resonator optics are formed by coatings on the crystal facets.[33] Its linewidth was probed with a custom-built Fabry-Perot interferometer that offered a resolution of 200 kHz. This high-resolution interferometer is no longer available, but the monolithic Ho:Tm:YLF laser can be used as a linewidth reference. By heterodyning the two lasers together a beat signal results with a width composed of a convolution of the linewidths of the two lasers.

This beat signal measurement is shown in Figure 3.15, in which the width of the beat signal is seen to be 198 kHz at full-width half-maximum. Since this 198 kHz width is a convolution of the two lasers, a precise quantification of each laser's linewidth is not possible. However, the width of each laser must be less than 198 kHz for the convolution to be of such a width.

3.4.6 Summary of Laser Characterization

A summary of the laser characteristics is given in Table 3.3. Comparison with Table 2.1 shows that all of the requirements for the continuous-wave master oscillator have been meet except for frequency stability. Achieving frequency stability is the subject of the following two chapters.

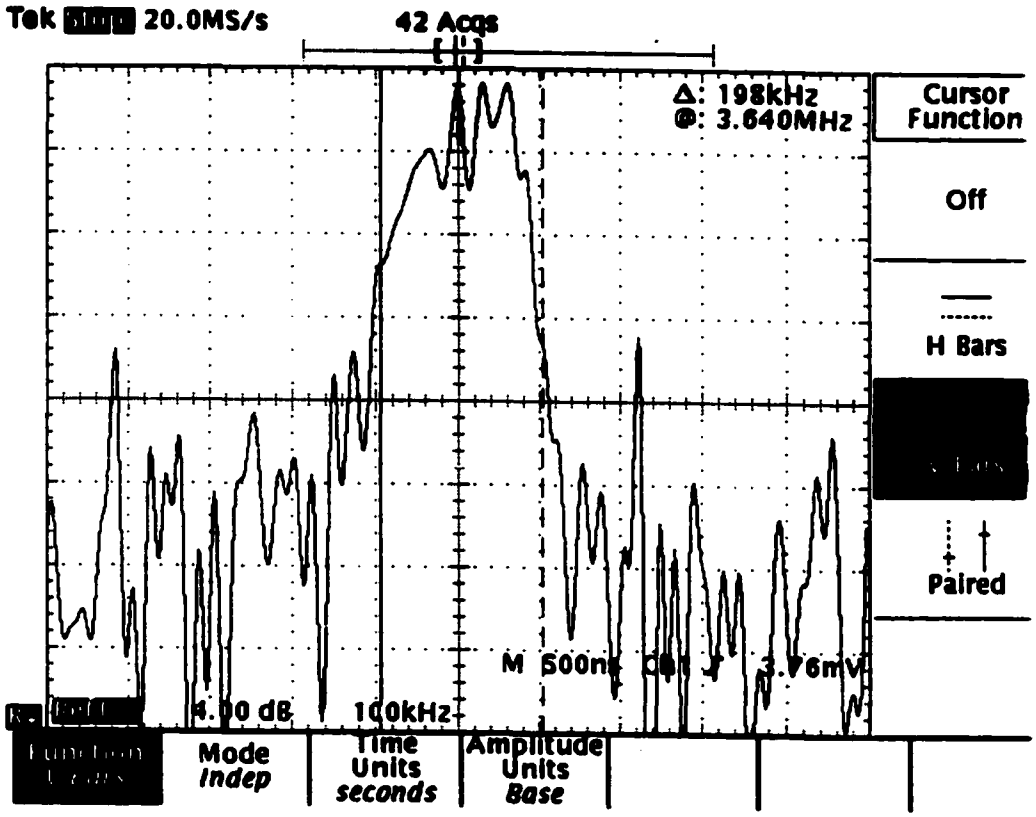

Figure 3.15: Heterodyne beat signal viewed by a fast Fourier transform between laser under test with Ho:Tm:YLF monolithic laser of linewidth less than 200 kHz. The width of the beat signal, as indicated by the cursor marks, is 198 kHz.

Coarse Tuning Range = 6 nm (2049 to 2055 nm) Resolution = 5 pm
Fine Tuning Range = 20 pm Resolution < 0.5 pm
Spectrum: single frequency
Linewidth < 198 kHz
Power: 20- 45 mW (depending on wavelength)

Table 3.3: Specifications of Ho:Tm:YLF laser.

CHAPTER 4

WAVELENGTH MODULATION SPECTROSCOPY: THEORY AND EXPERIMENT

Wavelength modulation spectroscopy (WMS) is a technique for interrogating molecular absorption features with a high level of sensitivity.[50] This sensitivity is allowed by a synchronous detection scheme related to the wavelength modulation, which results in suppression of background noise. WMS is sometimes referred to as derivative spectroscopy because the signals which result are related to derivatives of absorption with respect to wavelength.

Signals related to odd-order derivatives feature a zero crossing at line center and a linear region around the zero crossing. The linear section goes negative toward one side of line center, and flips polarity on the other side, allowing an instantaneous determination of the magnitude and direction of the laser's detuning from line center. Such a signal is used as a feedback error indication to stabilize the wavelength of the Ho:Tm:YLF laser, as is described in Chapter 5.

In this chapter the theory behind WMS is presented along with experiment results of the spectroscopy of carbon dioxide and water vapor. Section 4.1 presents a mathematical derivation of WMS. Sections 4.2 and 4.3 explore the physical properties of the carbon dioxide and water molecules, showing how rotational and vibrational transitions are involved in the absorption of laser light. Finally, in Sections 4.4 and 4.5 experiments and results are presented of the spectroscopy of carbon dioxide and water vapor.

4.1 Principles of Wavelength Modulation Spectroscopy (WMS)

The easiest implementation of laser spectroscopy of a gas is to tune the laser's wavelength over the region where the absorption is expected to be and to monitor the intensity transmitted through the gas. This technique could be improved by modulating the laser and detecting the transmitted light at the frequency of the modulation, thereby reducing noise by detecting the signal only within a narrow band of frequency. WMS is an implementation of such a modulation technique based on a phase modulation of the electric field generated by the laser. This phase modulation can be interpreted physically as a modulation of wavelength, hence the name for this spectroscopic technique. Phase modulation can also be interpreted as frequency modulation, suggesting the nomenclature of frequency modulation spectroscopy (FMS). While the use of the terminology of WMS and FMS would seem to be interchangeable, these two terms have come to imply a distinction in the scientific literature. WMS is reserved for describing techniques in which the frequency of modulation is much smaller than the spectral width of the absorption line, and FMS is used to describe techniques is which the frequency of modulation is comparable to the absorption line width. Spectral lines typically under study are in the megahertz to gigahertz range, so FMS uses modulation in the radio frequency range. WMS uses modulation in the audio frequency range, making the implementation of the electronics associated with the experiment easier to implement than for FMS. The advantage of FMS is that the higher modulation frequency places the noise floor further away from 1/f noise than in WMS. More sensitive detection can then be carried out using FMS, but at the expense of more complicated electronics. WMS is used in this research

since the higher level of sensitivity offered by FMS is not required due to the strongly absorbing lines used.

The mathematical analysis of WMS begins with considering the Beer-Lambert law describing the intensity of electromagnetic radiation propagating through a gas:

$$I(\nu) = I_0 e^{-\alpha(\nu)L} \quad . \quad (4.1)$$

Here L is the length of the absorption path, and $\alpha(\nu)$ is a frequency dependent absorption coefficient given by

$$\alpha(\nu) = n\bar{\sigma}g(\upsilon) \quad , \quad (4.2)$$

where n is the density of the gas, σ is the integrated absorption cross section, and $g(\nu)$ is the line shape function. A weak absorption feature, characterized by $\alpha(\nu) << 1$, allows an approximation of Equation 4.1:

$$I(\nu) \approx I_o[1 - n\bar{\sigma}g(\nu)L] \quad . \quad (4.3)$$

The unchanging background intensity is generally not of interest in experiments and is normalized from Equation 4.3 by considering a signal of the form

$$S = \frac{I(\nu) - I_0}{I_0} = -I_0 n\bar{\sigma}g(\nu)L \quad . \quad (4.4)$$

The frequency, ν, in all of the proceeding equations is modulated. That is, the laser frequency is sinusoidally varied to create an electric field from the laser described by

$$E(t) = E_0 \cos(2\pi\bar{\nu}_L t + \frac{\beta}{\omega_m}\sin\omega_m t) \quad , \quad (4.5)$$

where ν_L is the center frequency of the laser, ω_m is the modulation frequency, and β is the magnitude of the modulation in reciprocal seconds. The instantaneous frequency of this electric field is[51]

$$\nu(t) = \bar{\nu}_L + \beta \sin(\omega_m t) \quad . \quad (4.6)$$

The lineshape function can then be represented by

$$g(\bar{\nu}_L + \beta \sin(\omega_m t)) \equiv f(\phi) \quad . \quad (4.7)$$

Inspection of Equation (4.7) suggests that a solution for $f(\phi)$ will be composed of harmonics of the modulation frequency. Meyers and Putzer have derived a convenient Fourier series representation of $f(\phi)$ with the kth component of the series given by

$$C_k = \sum_{n=0}^{\infty} \frac{g^n(\nu_L)}{n!} \left(\frac{\beta}{2j}\right)^n B_{n,n-k} \quad , \quad (4.8)$$

where $B_{n,n-k}$ is the coefficient of the Z^{n-k} term in the residue theorem expansion for $(Z^2-1)^n$ with $Z = e^{j\phi}$.[52]

The WMS technique detects the harmonic terms indicated by Equation (4.8) using synchronous detection. It follows from Equations (4.5), (4.7), and (4.8) that the Nth detected harmonic can expressed as[53]

$$S_{wm}^N = -n\bar{\sigma}LI_0(-1)^{\frac{[N]}{2}} \sum_{v=0}^{\infty} \left(\frac{\beta}{2}\right)^{2v+N} \frac{1}{v!(v+N)!} g^{2v+N}(\nu_L) \quad , \quad (4.9)$$

Where [N] = N for even values of N and [N]=N-1 for odd values of N. A derivative is represented by $g^{2n+N}(\nu_L)$, describing the (2n+N)th derivative of the absorption line shape. In the case where the amplitude modulation, β, is small then the higher order terms of this summation will be small, leaving the v=0 term dominating. Thus, the first harmonic signal is proportional to the first derivative, the second harmonic signal will be proportional to the second derivative, etc.

The next step in evaluating Equation (4.9) is to analyze the lineshape function $g(\nu)$, so that its derivatives can be computed. Several mathematical models exist to describe lineshape functions including the lorentzian, gaussian, and voigt profiles.[54] Each of these models fits a particular case of different ranges of gas pressure in which different mechanisms dominate the line broadening.

At low gas pressures, less than 250 torr, the spectral broadening is due to the velocity of the individual molecules. That is, the range of velocities of the molecules creates a range of Doppler shifts about the absorption line center. This Doppler broadened line structure has been found to be accurately described by a gaussian function. At high gas pressure, above 250 torr, the collisions of molecules within the gas has more of an effect on spectral broadening than does the Doppler effect. This collision broadened regime is described by the lorentzian profile. In many experiments the pressure varies and the voigt profile is used, as it incorporates both Doppler broadening and collision broadening. In the limit of high and low gas pressures, the voigt profile assumes the shape of the lorentzian or gaussian profile.

The experiments presented here were carried out using low gas pressures in order to make the absorption lines as narrow as possible while still retaining a significant absorption strength. As will be described in the following chapter, a narrow absorption line provides a

better reference than does a wide line for the purpose of stabilizing a laser. The pressure used for spectroscopy of carbon dioxide and water were in the range of 2 torr to 15 torr, indicating that the gaussian profile is best suited to modeling the experiments.

The line shape function for a Gaussian profile is given by

$$g(\nu) = \left(\frac{4\ln 2}{\pi \Delta \nu_D^{\,2}}\right)^{1/2} \exp\left(\frac{-4\ln 2(\nu-\nu_0)^2}{\Delta \nu_D^{\,2}}\right) \quad , \qquad (4.10)$$

where $\Delta\nu_D$ is the Doppler width of the line given by

$$\Delta \nu_D = \left(\frac{8kT\ln 2}{Mc^2}\right)^{1/2} \nu_0 \quad . \qquad (4.11)$$

In Equation (4.11) M represents the mass of the molecule and c is the speed of light. The nth derivative of Equation (4.10) can be written as

$$g^N(\nu) = \frac{g(\nu)}{\pi^{1/2}} \frac{1}{(\Delta \nu_D)^{2N+1}} \sum_{k=0}^{[N]/2} C_{2k,N} (\Delta \nu_D)^{2k} (\nu-\nu_0)^{N-2k} \quad , \qquad (4.12)$$

where

$$C_{2k,N} = (-1)^k \frac{N!}{(N-2k)!} \frac{(-2)^{N-2k}}{k!} \quad , \qquad (4.13)$$

$$[N] = \begin{Bmatrix} N-1 & \text{for odd N} \\ N & \text{for even N} \end{Bmatrix} \quad . \qquad (4.14)$$

Insertion of Equations (4.12) to (4.14) in Equation (4.9) allows modeling of WMS signals. Analytical solutions for this manipulation become rather cumbersome, so numerical computer solutions have been used to generate the plots shown in Figure 4.1 for

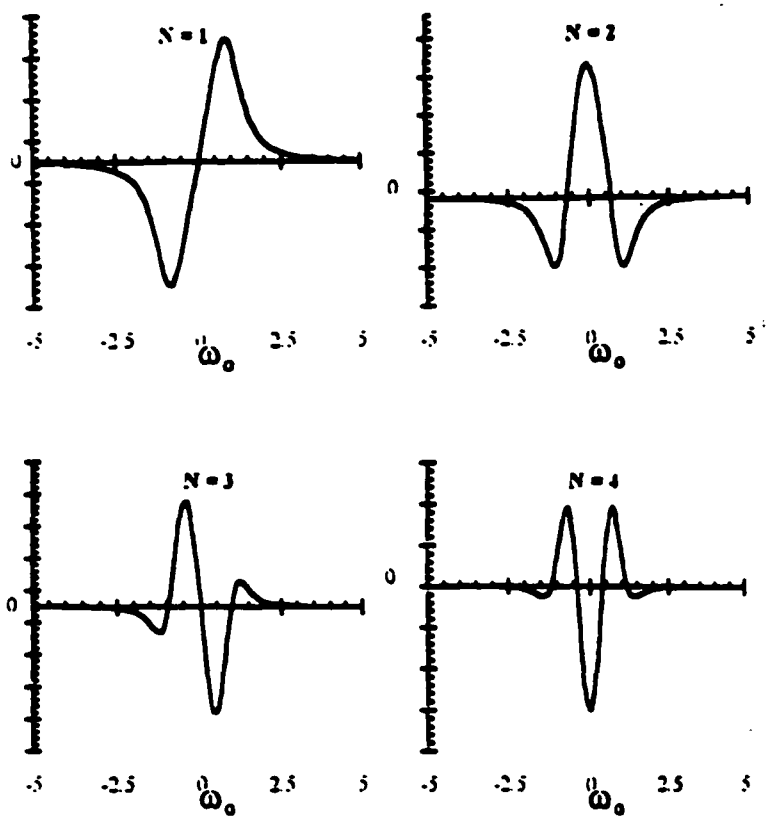

Figure 4.1: Theoretically derived wavelength modulation spectra for N=1 to 4. The vertical axes are arbitrary units. The horizontal axes are frequency normalized to linewidth. From Bullock et al.[55]

the first through fourth harmonics. An interesting feature in these plots is that the odd harmonics have a zero crossing at line center, while the even harmonics have a peak at line center. The peaks of the even harmonics make them useful for identifying line center, but the zero crossing of the odd harmonics makes them the primary interest in this research. The first harmonic signal will be used, as is described in the following chapter, as a feedback signal to indicate the location of the laser wavelength with respect to absorption line center.

4.2 Carbon Dioxide Spectroscopy

The three atoms of the carbon dioxide molecule form a linear molecule belonging to the $D_{\infty h}$ point group, having a symmetric top shape.[56] Figure 4.2 shows the energy levels associated with electronic transition of CO_2.[57] However, only the ground state energy is of interest in this research, as the infrared transitions involved are vibrational and rotational transitions taking place within the electronic ground state, $\chi'\Sigma_g$.

The vibrational energy levels within the ground electronic state are shown in Figure 4.3. Levels shown by solid horizontal lines have been observed experimentally, while the levels shown by dashed lines have been predicted by theory but not yet observed. Allowed transitions between energy levels are indicated by vertical lines, with Raman transitions represented by dashed vertical lines.

The vibrational spectra of carbon dioxide stems from three fundamental modes of vibration labeled v_1, v_2, and v_3 in Figure 4.4. The v_1 mode is a symmetric stretch, the v_2 mode is a bend, and the v_3 mode is an asymmetric stretch. These vibrational modes are each quantized, and each transition will have a series of three integers associated with it to

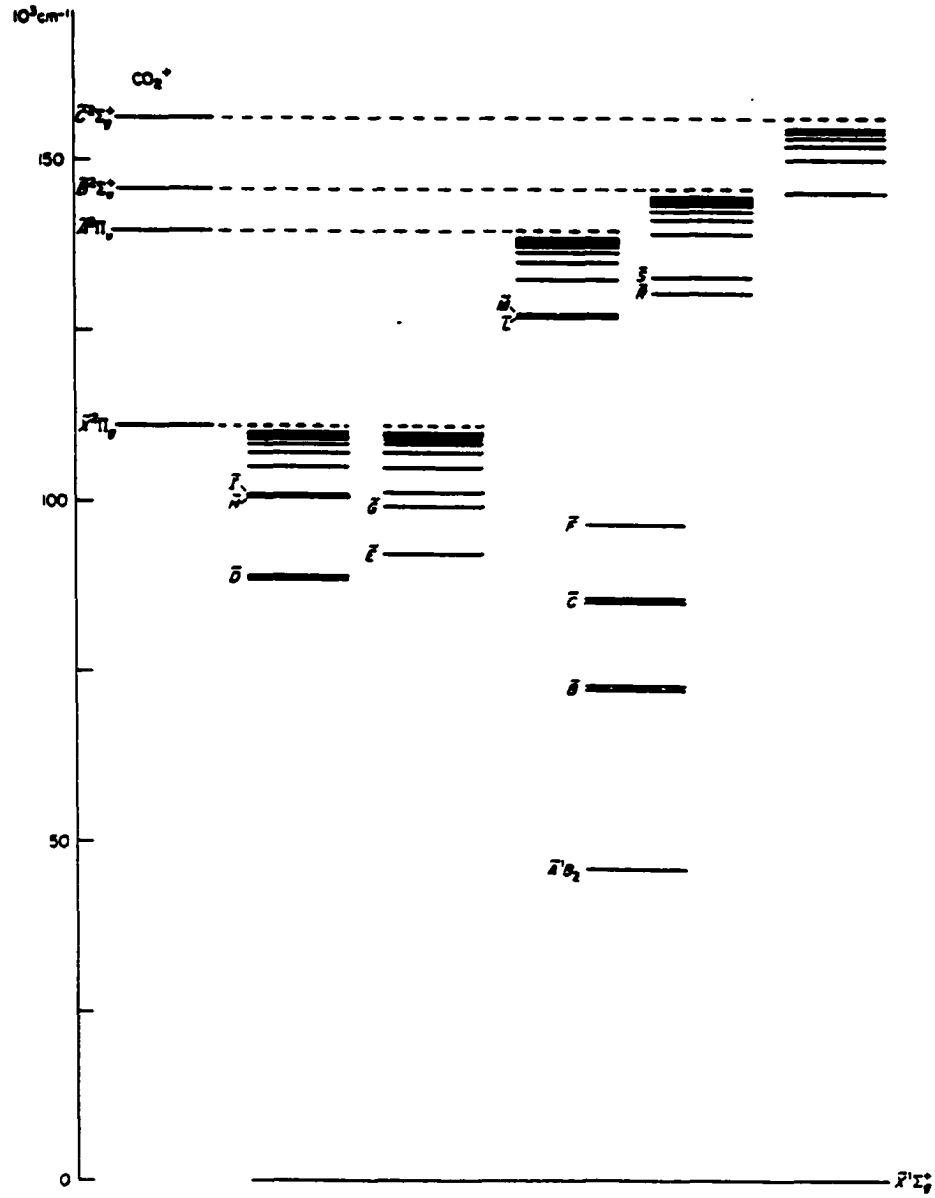

Figure 4.2: Observed energy levels associated with electronic transitions of CO_2. From Herzberg.[57]

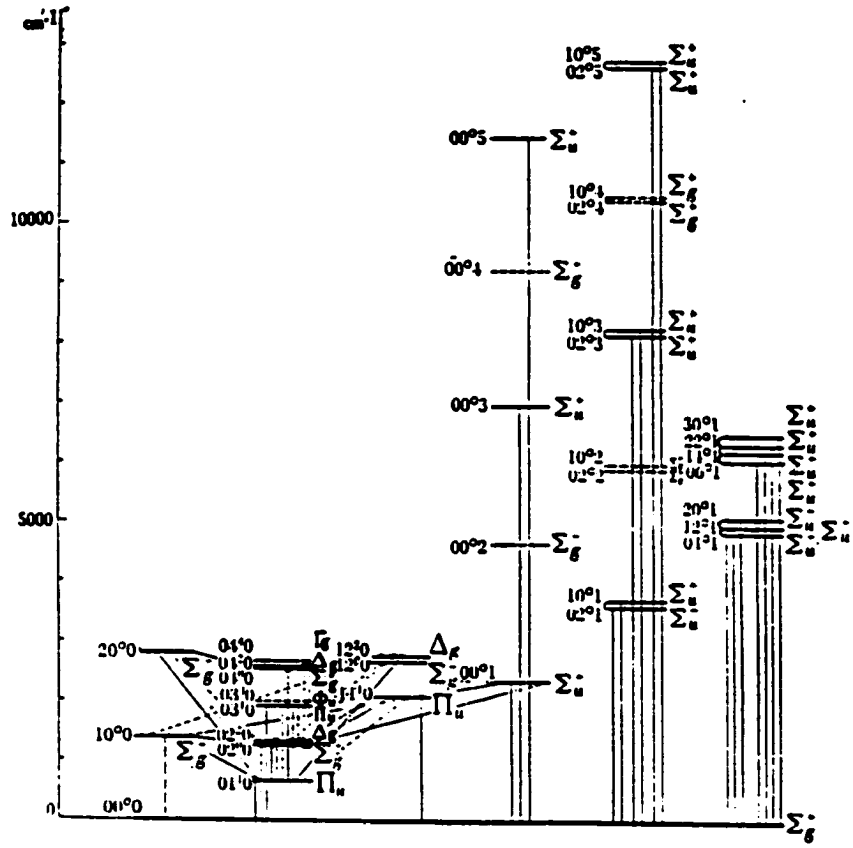

Figure 4.3: Vibrational energy levels within the ground electronic state of CO_2. From Herzberg.[58]

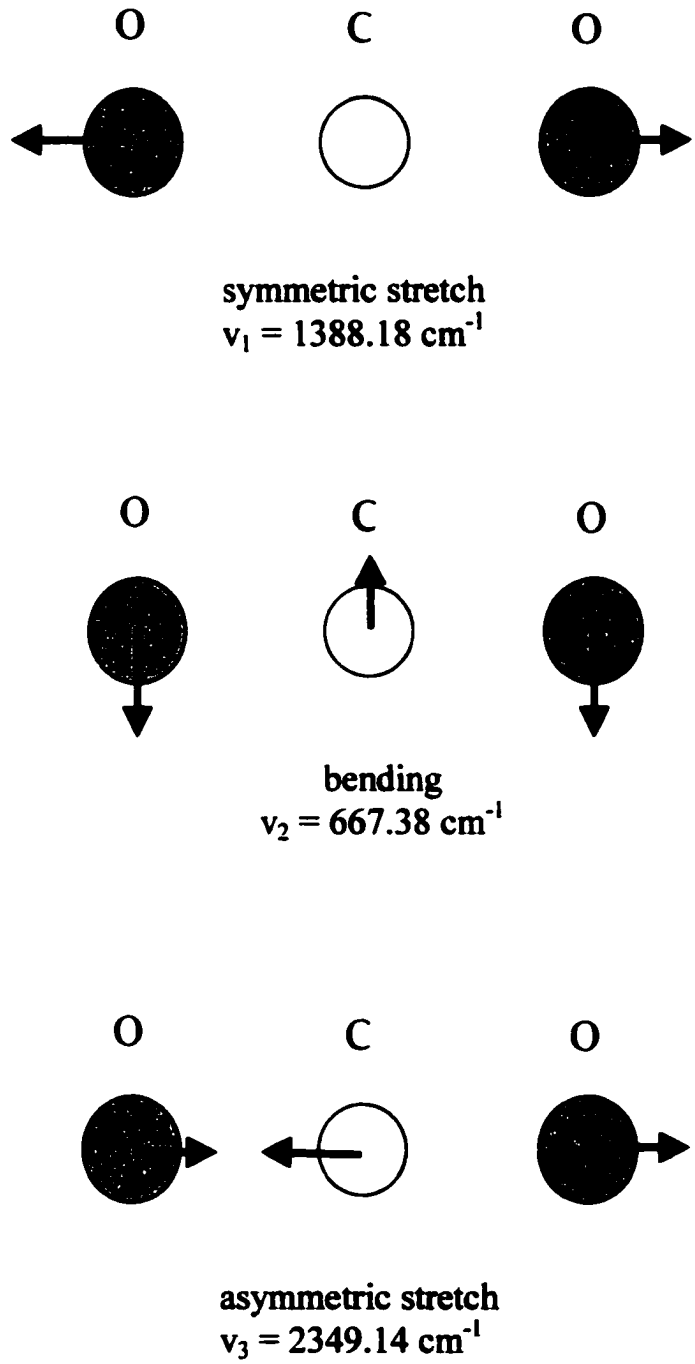

Figure 4.4: The three fundamental modes of vibration of CO_2.

indicate the number of quanta in each mode. Because bending of the molecule can occur in any plane around the axis of the molecule, the v_2 mode is degenerate. Depending on where the molecule is bent an additional angular momentum can be added proportional to Planck's constant. Extra notation must be introduced to describe this degeneracy of the v_2 mode. Hence, a subscript is added to the v_2 integer to indicate the presence or absence of additional angular momentum. The total vibrational energy of a particular level is given by

$$G(v_1,v_2,v_3) = w_1(v_1+\frac{1}{2}) + w_2(v_2+1) + w_3(v_3+\frac{1}{2}) + x_{11}(v_1+\frac{1}{2})^2 + x_{22}(v_2+1)^2 + g_{22}l_2^2 + x_{33}(v_3+\frac{1}{2})^2 + x_{12}(v_1+\frac{1}{2})(v_2+1) + x_{13}(v_1+\frac{1}{2})(v_3+\frac{1}{2}) + x_{23}(v_2+1)(v_3+\frac{1}{2}) \quad (4.15)^{58}$$

Where v_1, v_2, and v_3 are the vibrational mode quanta previously described, l_2 is the quantum number of the vibrational angular momentum (l_2 = 0, 1, 2, 3, . . . corresponds to Σ, Π, Δ, Φ, . . .), and the other parameters are empirically derived constants summarized in Table 4.1.

$\omega_1 = 1351.2\ cm^{-1}$	$\omega_2 = 672.2\ cm^{-1}$	$\omega_3 = 2396.4\ cm^{-1}$
$x_{11} = -0.3$	$x_{22} = -1.3$	$x_{33} = -12.5$
$x_{12} = 5.7$	$x_{13} = -21.9$	$x_{23} = -11.0$
$g_{22} = 1.7$		

Table 4.1: Spectroscopic constants associated with vibration of CO_2.[58]

Within each of the vibrational energy levels of Figure 4.3 is a manifold of rotational energy levels. Allowed rotational transitions are determined by a selection rule that requires that the rotational quantum number, J, can only change by zero or +/- 1. The three allowed quantum number changes are denoted by P, Q, and R. The P(J) branch involves a rotational quantum number change of –1, the Q(J) branch involves a rotational quantum number change of 0, and the R(J) branch involves a rotational quantum number change of +1.

4.3 Water Vapor Spectroscopy

The electronic transitions of water vapor are shown in Figure 4.5, but as in the case of carbon dioxide the transition encountered in this research is rotational/vibrational within the ground electronic state $^1A_1$. While being a three atom molecule like carbon dioxide, the vibrational/rotational spectra of water vapor is complicated by the fact that there is a 120 degree bond angle between the oxygen and hydrogen atoms. The three fundamental modes of vibration, presented in Figure 4.6, then include an angular displacement.

The bond angle of water vapor places it in the C_{2v} point group, making it an asymmetric top molecule. The vibrational spectra of asymmetric top molecules are classified as being parallel, called species A, or perpendicular, called species B, to the axis of symmetry.[58] The transition used here is of species B, for which a vibrational energy level diagram is shown in Figure 4.7. A quantitative expression of the vibrational structure of water is given by

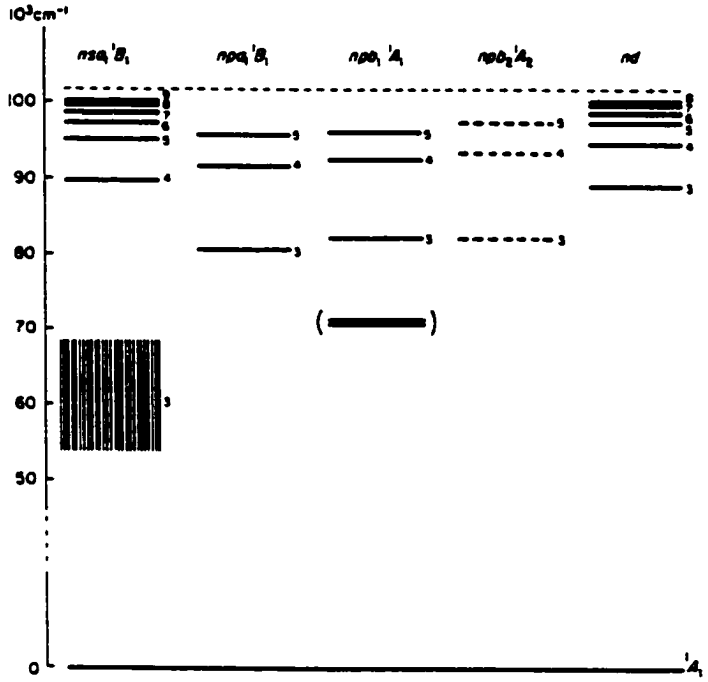

Figure 4.5 : Observed energy levels associated with electronic transitions of H_2O. From Herzberg.[57]

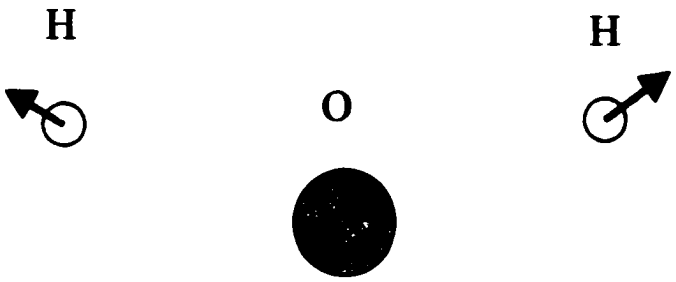

symmetric stretch
$v_1 = 3651.7\ cm^{-1}$

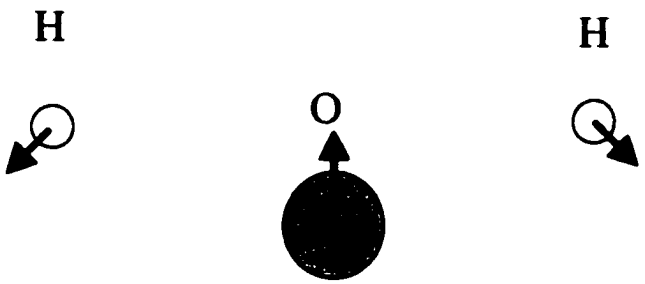

bending
$v_1 = 1595.0\ cm^{-1}$

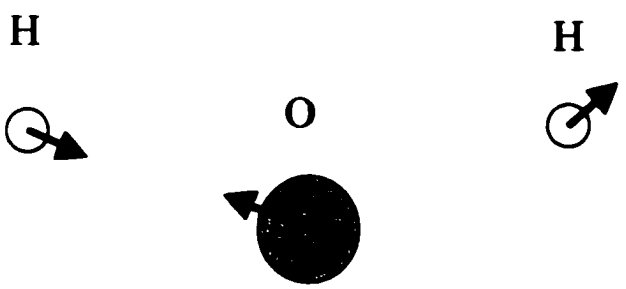

asymmetric stretch
$v_1 = 3755.8\ cm^{-1}$

Figure 4.6 : The three fundamental modes of vibration of H_2O.

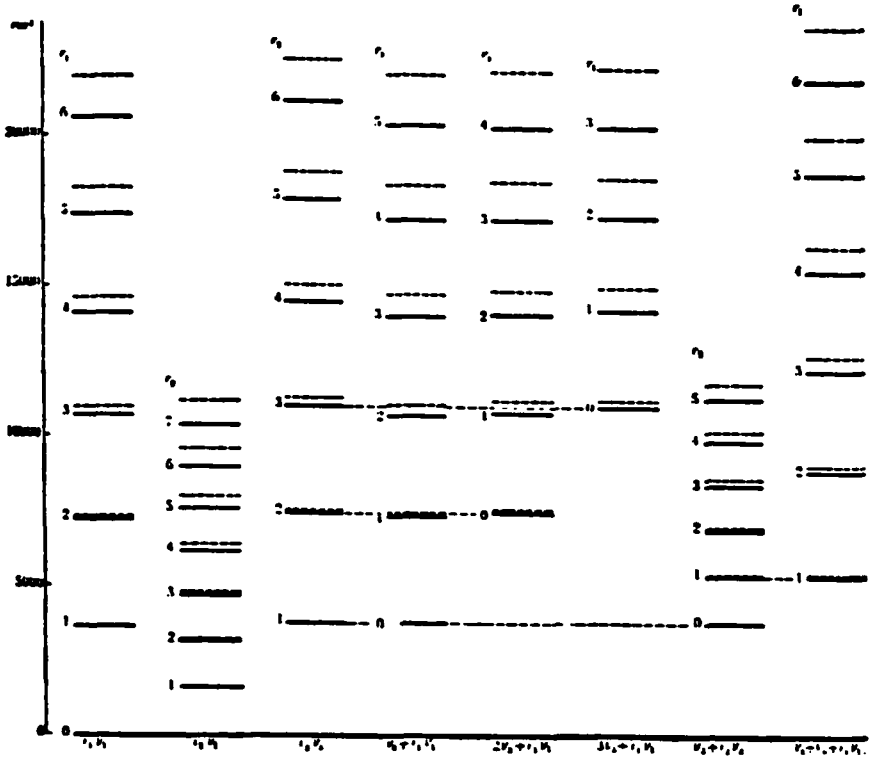

Figure 4.7: Vibrational energy levels of H_2O. From Herzberg.[58]

$$G(v_1,v_2,v_3) = w_1(v_1+\frac{1}{2}) + w_2(v_2+1) + w_3(v_3+\frac{1}{2}) + x_{11}(v_1+\frac{1}{2})^2 + x_{22}(v_2+1)^2 + x_{33}(v_3+\frac{1}{2})^2 + x_{12}(v_1+\frac{1}{2})(v_2+1) + x_{13}(v_1+\frac{1}{2})(v_3+\frac{1}{2}) + x_{23}(v_2+1)(v_3+\frac{1}{2}) \quad , \quad (4.16)^{58}$$

which is similar to Equation (4.15) except for the absence of the degeneracy term. The constants associated with Equation (4.16) are summarized in Table 4.2.

$\omega_1 = 3693.8\ cm^{-1}$	$\omega_2 = 1614.5\ cm^{-1}$	$\omega_3 = 3801.7\ cm^{-1}$
$x_{11} = -43.8$	$x_{22} = -19.5$	$x_{33} = -46.3$
$x_{12} = -20.0$	$x_{13} = -155.0$	$x_{23} = -19.8$

Table 4.2: Spectroscopic constants associated with vibration of H_2O.[58]

Rotational transitions of water vapor follow the same selection rule for carbon dioxide, that is

$$\Delta J = 0, \pm 1 \quad . \quad (4.17)^{58}$$

However, the asymmetric geometry of water vapor places an additional selection rule on allowed rotational transitions, requiring that the change in levels must be of

$$++ \leftrightarrow -- \quad \text{or} \quad +- \leftrightarrow -+ \quad . \quad (4.18)^{86}$$

This notation of + and – refers to symmetry properties of the rotational eigenfunctions. The levels associated with these symmetry properties are shown in Figure 4.8.

4.4 WMS of Carbon Dioxide

The Ho:Tm:YLF laser described in Chapter 3 was used to probe three absorption lines of carbon dioxide at 2050.428, 2052.070, and 2053.204 nm. These transitions are all in the ground electronic state, $\chi'\Sigma_{g^+}$ and all within the same vibrational transition from a 00^00 lower level to 20^01 upper level. Three different rotational transitions are involved of R(32) for the line centered at 2050.428 nm, R(26) for the line centered at 2052.070 nm, and R(22) for the line centered at 2053.204 nm. Figure 4.9 shows a schematic for the spectroscopy experiments. A Faraday isolator was used to prevent back-reflections from destabilizing the laser. The beam was focused by a lens into the center of a mulitpass cell, set in this case for 13 m of path length. InGaAsP photodiodes were used at the output of the cell and to sample the laser beam before entering the cell. About 0.5 mW of laser power was picked off for the photodiode before the cell, and 2 mW was sent into the cell. The purpose of the photodiode before the cell is to monitor amplitude variation of the laser, which has a large impact on the stabilization results. The multipass cell was first filled with pure carbon dioxide at atmospheric pressure, before activating a vacuum pump to bring the carbon dioxide pressure to 2 torr.

Wavelength modulation was applied by driving the laser's PZT with a 100 Hz sinusoid of 50 V_{pp}. β of Equation (4.5) can be calculated by considering that the maximum

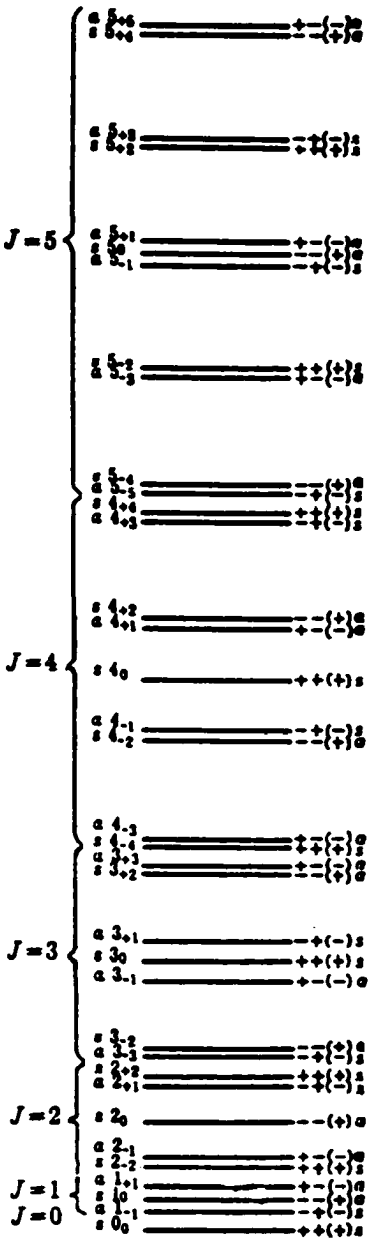

Figure 4.8: Rotational energy levels of H_2O. From Herzberg.[58]

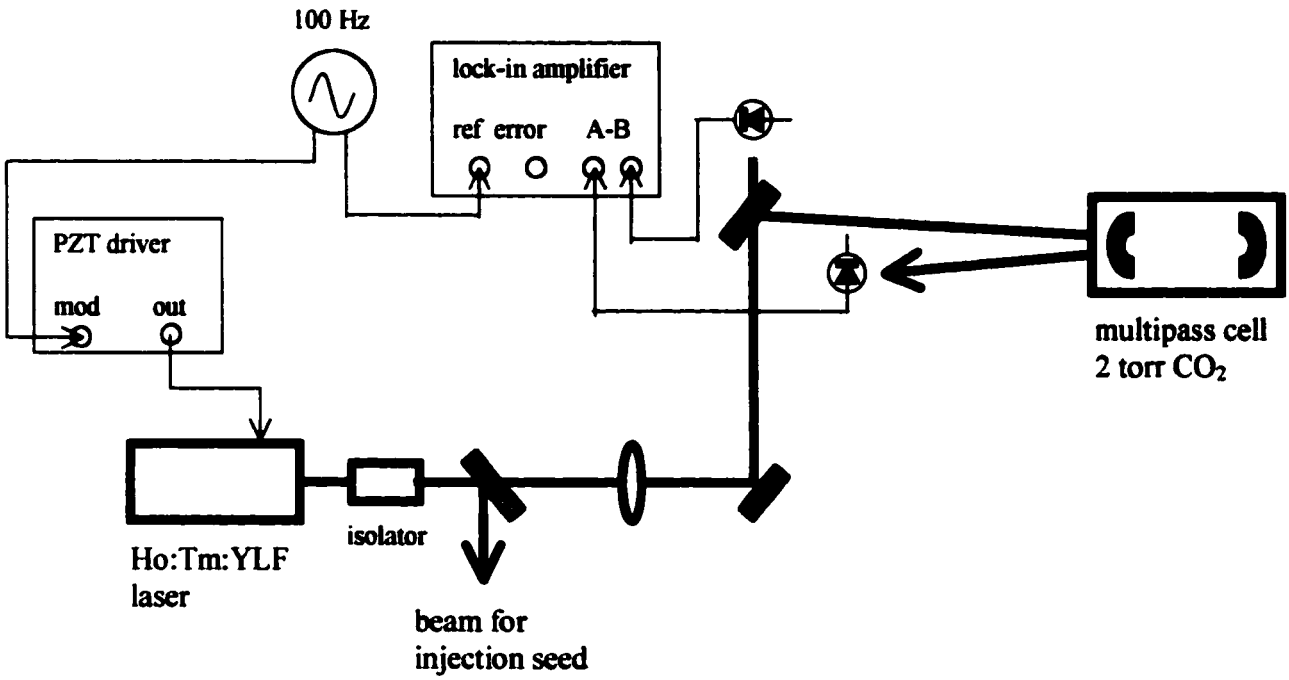

Figure 4.9: Layout of spectroscopy experiment.

frequency excursion, Δf, of the modulated field is related to the derivative of the phase of the right hand side of Equation (4.5). That is

$$\Delta f = \beta / 2\pi \qquad (4.15)$$

Δf can be calculated in this experiment by considering the 50 V_{pp} PZT modulation with regard to Figure 3.10. Δf is thus found to be 71 MHz. The modulation frequency of 100 Hz, making ω_m = 626 rad/s, was selected because higher modulation frequencies were found to excite mechanical resonance and create nonlinear modulation.

The signal seen by the photodiode after the cell contains harmonics of the modulation frequency with the Nth harmonic related to the Nth derivative of the absorption line shape with respect to wavelength. Demodulation of these harmonics is performed by a lock-in amplifier, and Figures 4.10 to 4.12 show the first and second harmonics for three different carbon dioxide lines. Also shown on each of these figures is the direct absorption signal made without use of laser modulation—the intensity of the transmission through the cell was monitored as the laser wavelength was swept. Two features are of interest in these direct absorption signals, taking the absorption line centered at 2053.204 nm as an example. First, the carbon dioxide absorption is readily apparent with a full-width half-maximum linewidth of 5 pm, on-center transmission of 19.4% , and center wavelength of 2053.204 nm—all consistent with the HITRAN database.[25] Second, a strong parabolic variation of laser intensity is seen as the laser is tuned. This laser intensity variation is also seen by the photodiode before the cell. The absorption signal could be normalized by the pre-cell signal to remove the effects of intensity variation, but this is not

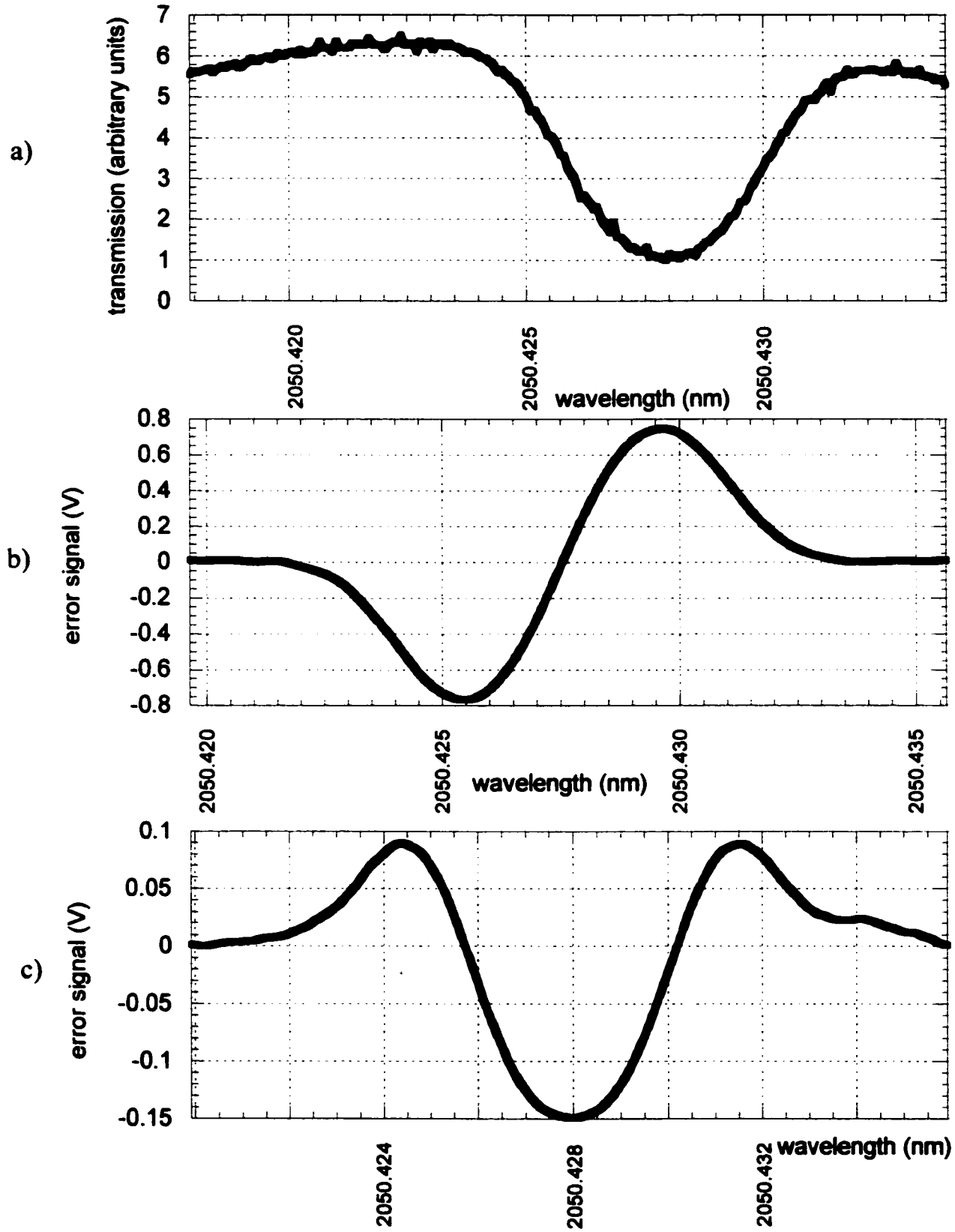

Figure 4.10: Spectra of carbon dioxide absorption line centered at 2050.428 nm—a) direction absorption, b) first harmonic, and c) second harmonic.

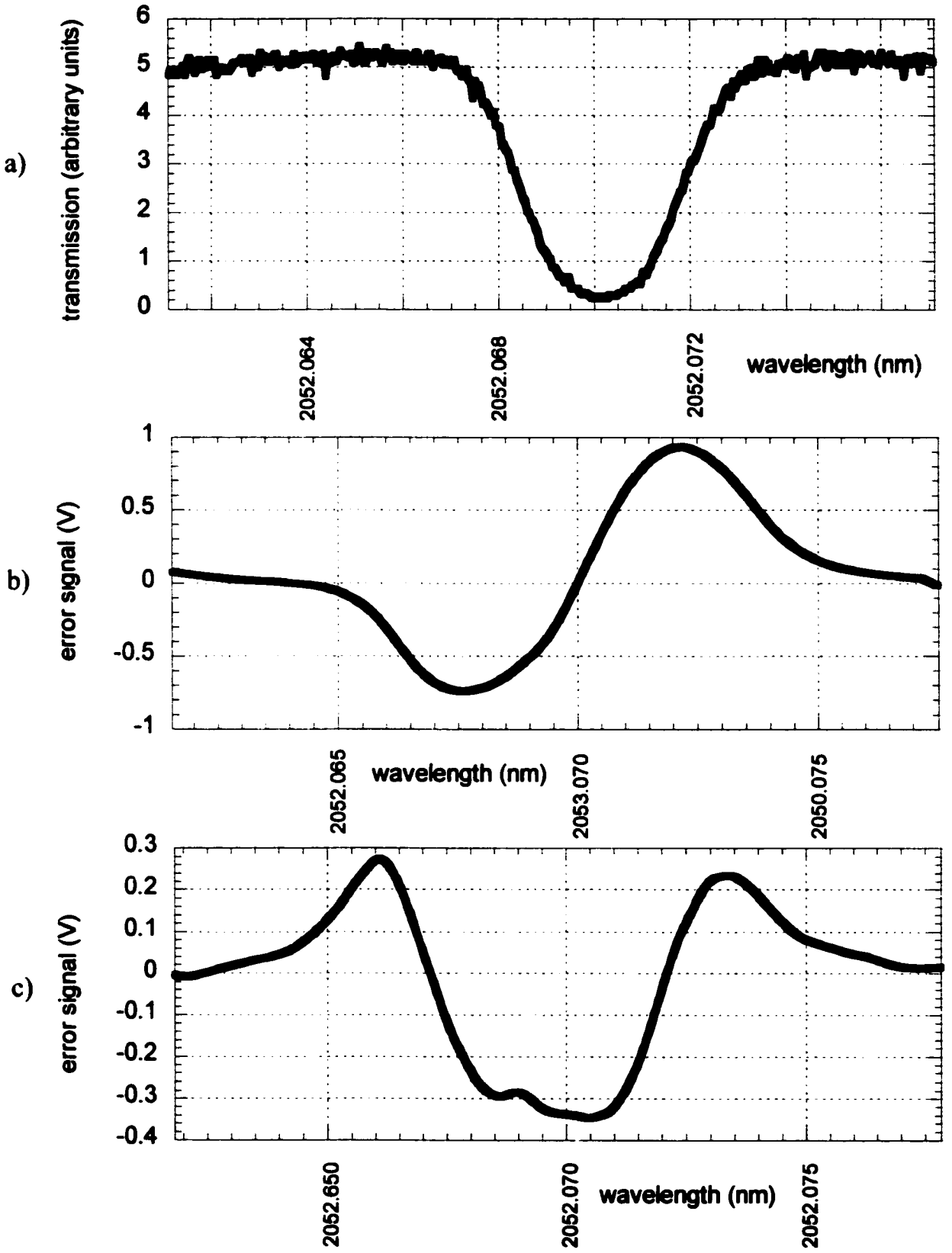

Figure 4.11: Spectra of carbon dioxide absorption line centered at 2052.070 nm—a) direct absorption, b) first harmonic, and c) second harmonic

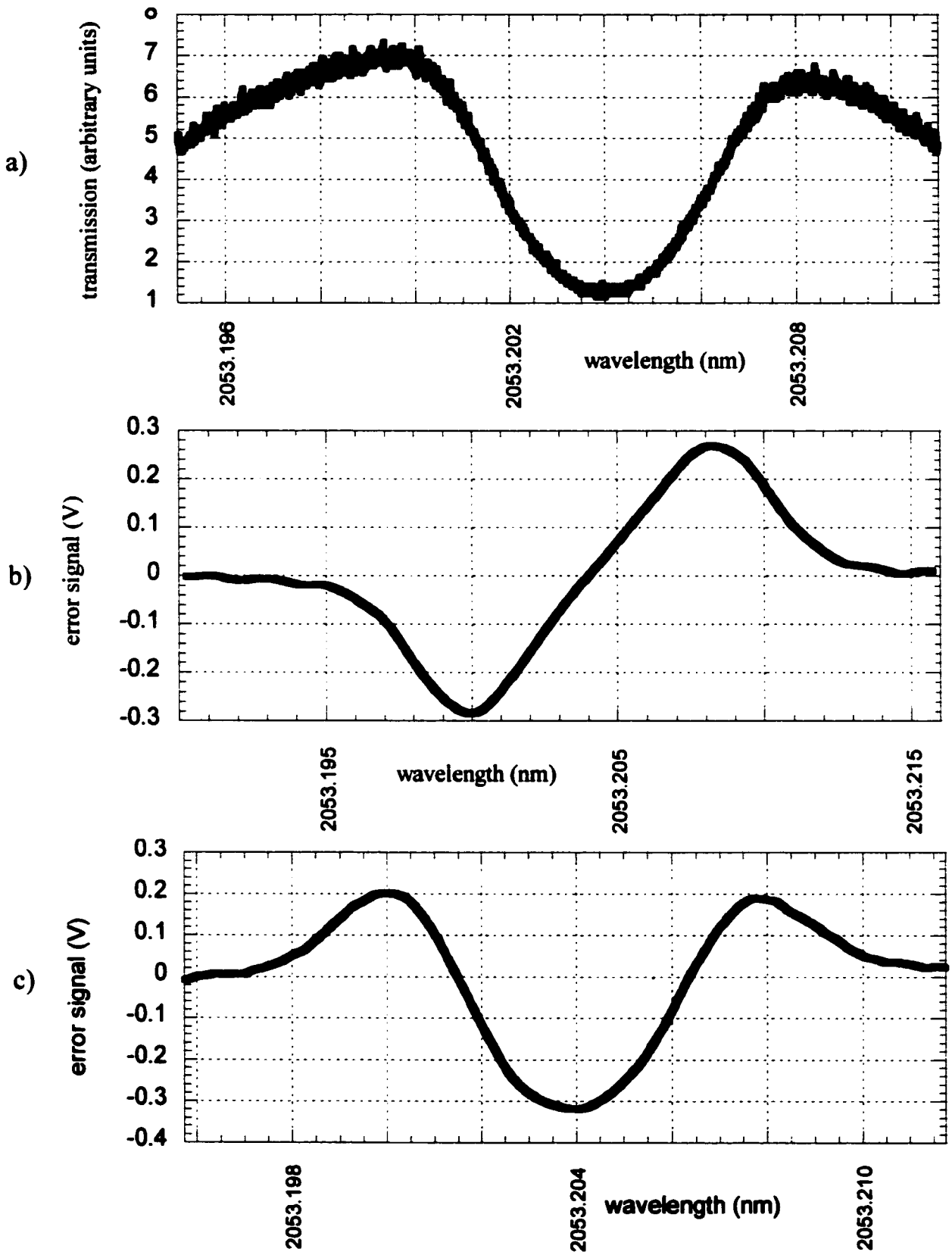

Figure 4.12: Spectra of carbon dioxide absorption line centered at 2053.204 nm—a) direct absorption, b) first harmonic, and c) second harmonic.

done in the presentation of these figures to emphasize the impact of laser intensity variation on the WMS signals.

To compensate for the intensity variation a differential input was used to the lock-in amplifier, in which the pre-cell signal is subtracted from the absorption signal prior to demodulation. For this subtraction to work effectively the amplitude of the photodiode signals must be an equal voltage. Such balancing was accomplished by taking the laser well off an absorption line and adjusting the gain of one of the photodiodes so that their voltages are equal. With balanced detection applied, the first and second harmonics of Figure 4.10 to 4.12 take on the approximation to derivatives as modeled in Section 4.1.

4.5 WMS of Water Vapor

A water vapor line centered at 2050.532 nm was also studied with the Ho:Tm:YLF laser, the same line used for the DIAL measurements described in Chapter 2. The same setup used for the carbon dioxide spectroscopy was used for water vapor except for the substitution of another multipass cell. The new cell offered a longer path length, 75 m, needed to accommodate the relatively weak strength of this water line.

In addition to the weaker absorption strength, working with the water vapor was more difficult than the carbon dioxide in that the water had to vaporized into the cell from a sample of liquid water. Care also had to be taken not to let the pressure and temperature inside the cell reach levels that would cause the water to condense onto the mirrors inside the multipass cell, which could damage the coatings of the mirrors. Water inside a cell at

room temperature would condense at a pressure of 20 torr, so the water vapor pressure was kept around 10 torr to provide a margin for error.

The apparatus for filling the multipass cell is diagrammed in Figure 4.13. A T-valve is used to connect a fill port to either a vacuum pump or a flask containing liquid water. This valve is first set to allow the vacuum pump to suck the air out of the multipass cell. The T-valve is then switched to the water flask while monitoring a vacuum guage. When the vacuum gauge reads 10 torr the cell is closed off. During this process air trapped

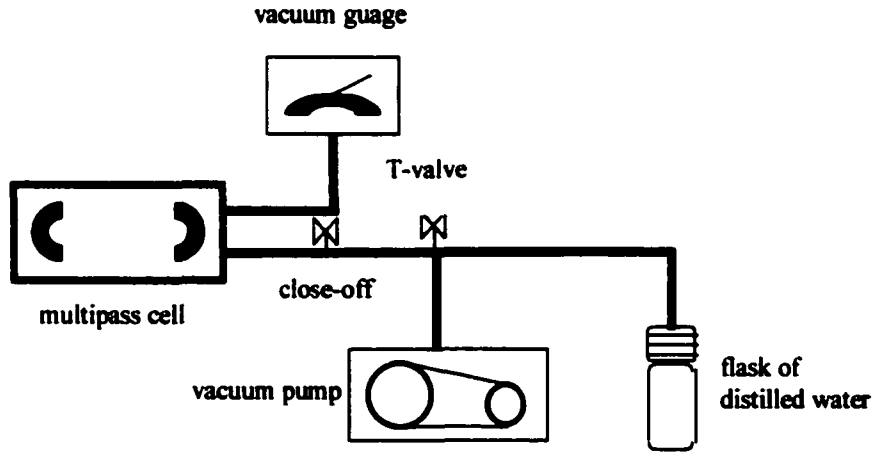

Figure 4.13: Appartus for filling multipass cell with water vapor.

in the water flask and connecting tubing fills the cell, along with water vapor. The evacuate-and-fill process is repeated in an attempt to fill the cell only with water vapor. Despite this procedure, a significant amount of air is still mixed with the water vapor. The resulting mixture in the cell was 10 torr total pressure with a water vapor content creating a 70% relative humidity. The water vapor absorption is then not as strong as desired because its concentration is diluted.

Indeed, the direct absorption signal was not strong enough to be seen. However, the sensitivity offered by WMS allowed first harmonic signals to be observed as shown in Figure 4.14. The PZT modulation was increased to 100 V_{pp} from the 50 V_{pp} used for carbon dioxide spectroscopy. While having all of the characteristics of a first derivative, comparison of this signal with the carbon dioxide spectra shows that the water vapor signal is plagued by more noise. The second harmonic signal was inundated with noise and unrecognizable as a second derivative.

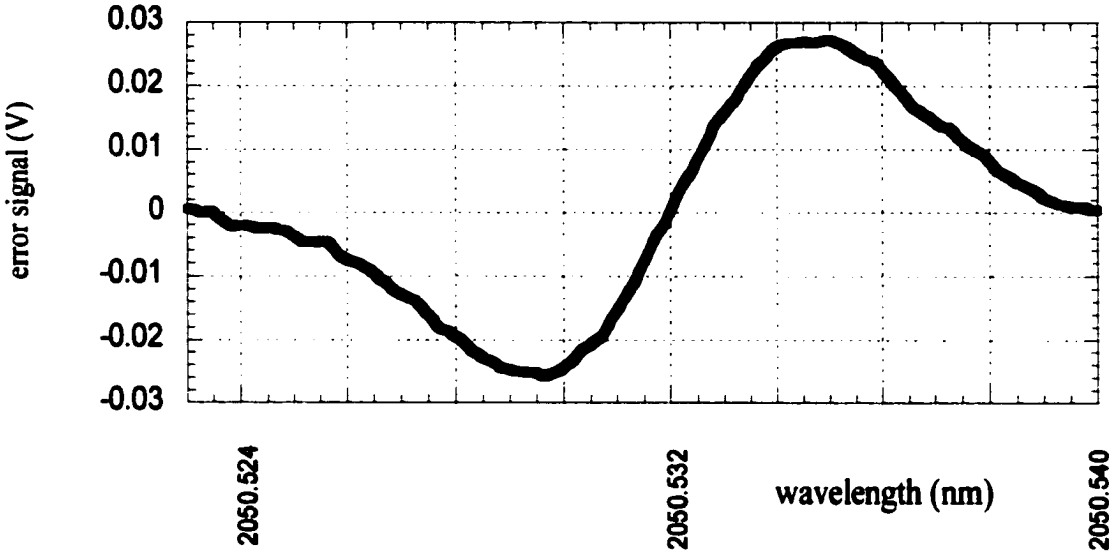

Figure 4.14: First harmonic spectrum of water vapor line centered at 2050.532 nm.

CHAPTER 5

FREQUENCY STABILIZATION: THEORY AND EXPERIMENT

The first-harmonic signals of the absorption lines presented in Chapter 4 can be used as an error signal to indicate how far, and to which side, the laser wavelength may be with respect to line center. In this chapter the results of a feedback scheme will be described for stabilizing the laser wavelength to absorption line center. The terms "frequency stabilization" and "wavelength stabilization" are used here interchangeably, but the convention in the scientific literature is to refer to the technique as frequency stabilization.

The basis of the frequency stabilization technique is to continuously adjust the laser PZT's DC voltage to the keep the first-harmonic error signal at its zero crossing. This technique has been used extensively to stabilize diode lasers to absorption lines.[59, 60] Work with solid-state lasers includes that of Arie *et al.* stabilizing a Nd:YAG laser to iodine at 639.5 nm and Laporta *et al.* stabilizing an Er:Yb laser to acetylene at 1530 nm.[61,62] The work presented in this chapter is the first investigation of the stabilization of a laser at or within 500 nm of the 2-μm wavelength.[63]

Figure 5.1 shows the setup for the stabilization experiments, which adds a feedback control loop to the spectroscopy experiment of Figure 4.9. The control loop for pushing the PZT was implemented with a Labview program running on a personal computer.[64] The output of the lock-in amplifier was digitized, and the Labview algorithm averaged five consecutive samples taken once every second. An increment of voltage was applied to the PZT if the average error signal exceeded a set boundary, and the applied voltage was held constant if the error signal was within the boundary.

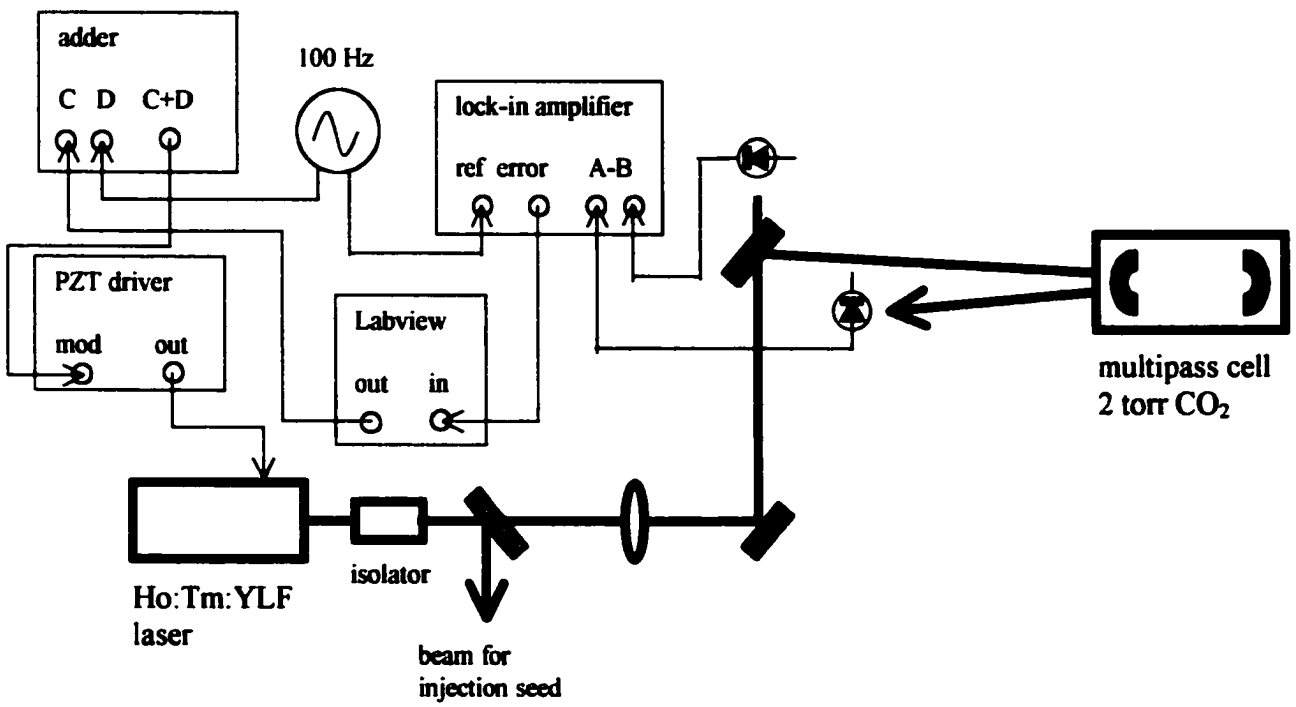

Figure 5.1: Layout of the spectroscopy and line stabilization experiments. Optical paths are drawn as thicker lines.

The error signal was also used to monitor the quality of the frequency stabilization and to track the drift of a free running laser. Plots will be presented in the following sections showing the frequency drift with and without stabilization feedback applied. In Section 5.1 the theoretical performance of the stabilization scheme is studied. Section 5.2 describes stabilization to carbon dioxide, and Section 5.3 describes experiments in stabilization to water vapor.

5.1 Theoretical Performance of Stabilization

A theoretical prediction of stabilization performance can be formulated by considering the first-derivative error signal shown in Figure 5.2. Figure 5.2 is similar to Figure 4.10b except that a greater voltage range is used, reflecting the voltage range actually used by the lock-in amplifier of Figure 5.1 and subsequently digitized by the computer that forms the feedback loop. Although the linear region of the first-derivative signal is the useful part for stabilization, the lock-in amplifier has to be set to work with the entire range of the signal plus an additional margin. Without viewing the entire signal, it would be impossible to determine if the first-derivative signal is free from distortion.

The computer program which controls the stabilization works with this extended voltage range, from −1.4 to 1.4 V in the data of Figure 5.2. The 8 bits with which the program processes the signal is spread over this 2.8 V range. The resolution of the feedback system is

$$\Delta V = \frac{2.8}{256} = 9.4\,\text{mV} \quad , \qquad (5.1)$$

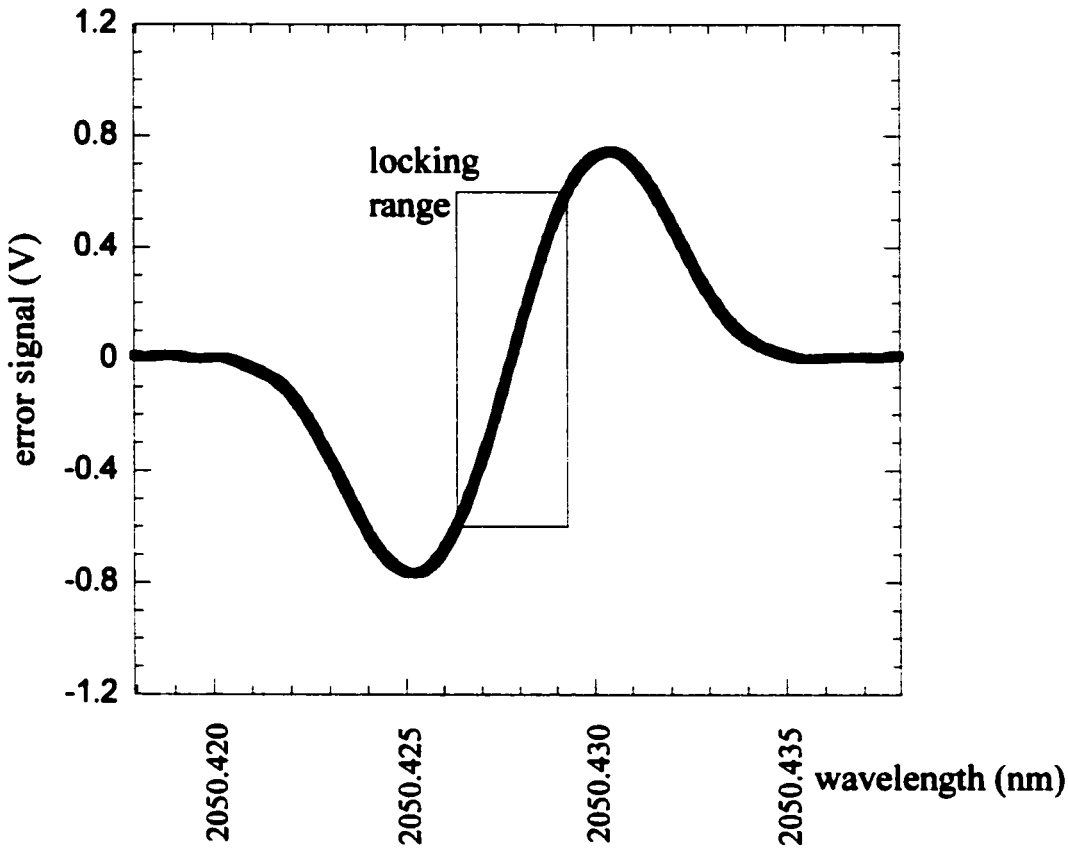

Figure 5.2: Locking range of the first-derivative error signal.

as 8 bits allows 256 levels. This voltage resolution can be converted to a frequency resolution by noting that the 1.2 V extent of the locking range corresponds to 2.4 pm (170 MHz), as seen in comparing Figure 5.2 to Figures 4.10a and 4.10b. The 9.4 mV voltage resolution then implies a 1.33 MHz frequency resolution.

This frequency resolution represents the finest frequency correction that the feedback control loop can apply. Thus, stabilization to within better than 1.33 MHz of absorption line center can not be expected. A possible means for achieving a higher level of control would be to make the locking range of Figure 5.2 steeper. A steeper slope corresponds to a narrower absorption line width, as could be obtained by decreasing the pressure of the gas or by using a different gas of inherently narrower width. Improvement of the control loop resolution could also be achieved by increasing the number of bits used in the control loop processing. However, going to additional expense or complication is not required since the requirement is to stabilize the CW master oscillator to within 1 pm (71 MHz). The control loop as designed has enough resolution to meet this requirement.

5.2 Frequency Stabilization to Carbon Dioxide

Figure 5.3 shows the use of the first-harmonic error signal to characterize the drift of the free-running Ho:Tm:YLF laser. In this record the laser was tuned with the PZT to line center by monitoring for a zero crossing of the error signal. The PZT voltage was then left constant, and the record was made of the error signal over the span of one hour. The free-running laser drifted 215 MHz from line center before drifting back toward line

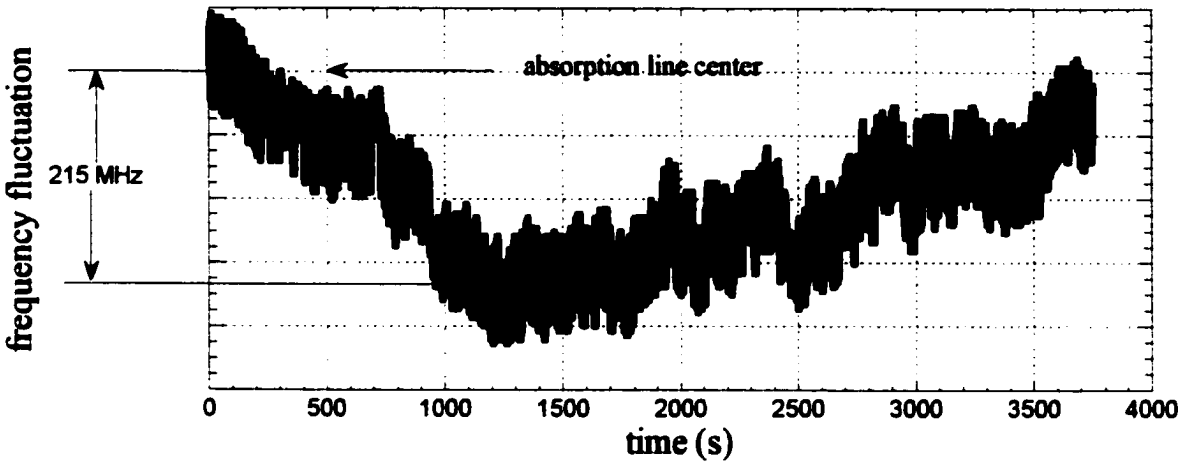

Figure 5.3: Frequency fluctuations of free-running laser as tracked by the first-harmonic error signal.

center. In most observations of laser drift the wavelength usually drifted in one direction to take the wavelength well off center, but in the data of Figure 5.3 a less common occurrence is seen as the drift changes direction. This technique of monitoring wavelength drift has the disadvantage of being ambiguous if the wavelength goes outside the linear range of the first-harmonic error signal. The nonlinear characteristic at further wavelengths makes it impossible to distinguish the direction of drift

Figure 5.4 shows more records of first-harmonic error signals, but in this case the stabilization control has been used. The results of the stabilization are shown to the three carbon dioxide lines described in Chapter 4 centered at 2050.428, 2052.070, and 2053.204 nm. Before each record was made the laser was intentionally detuned from line center. The beginning of each record thus shows the error signal quickly pulled toward zero as the stabilization is engaged. Confinement of the error signal near zero indicates that the laser wavelength has been locked on line center. The excursions of the error signal from zero indicate that the laser has been confined to within 13.5 MHz of line center for the transitions centered at 2050.428 nm and 2053.204 nm. Stabilization to the line centered at 2052.070 is slightly less effective with stabilization to within 16 MHz of line center. The lock to this transition is weaker than those of other two because the error signal, shown in Figure 4.11b, suffers from minor distortion, making the error signal less distinct than those associated with the lines at 2050.328 and 2053.204 nm.

The reduction of jitter to within 13.5 MHz of absorption line center is well within the requirement listed in Table 2.1 for less than 1 pm (71 MHz). The stabilization scheme is therefore acceptable for the desired lidar application. Performance is, however, approximately ten times larger than the theoretical minimum stabilization level of 1.33 MHz. This deviation from ideal performance is attributed to two factors. First,

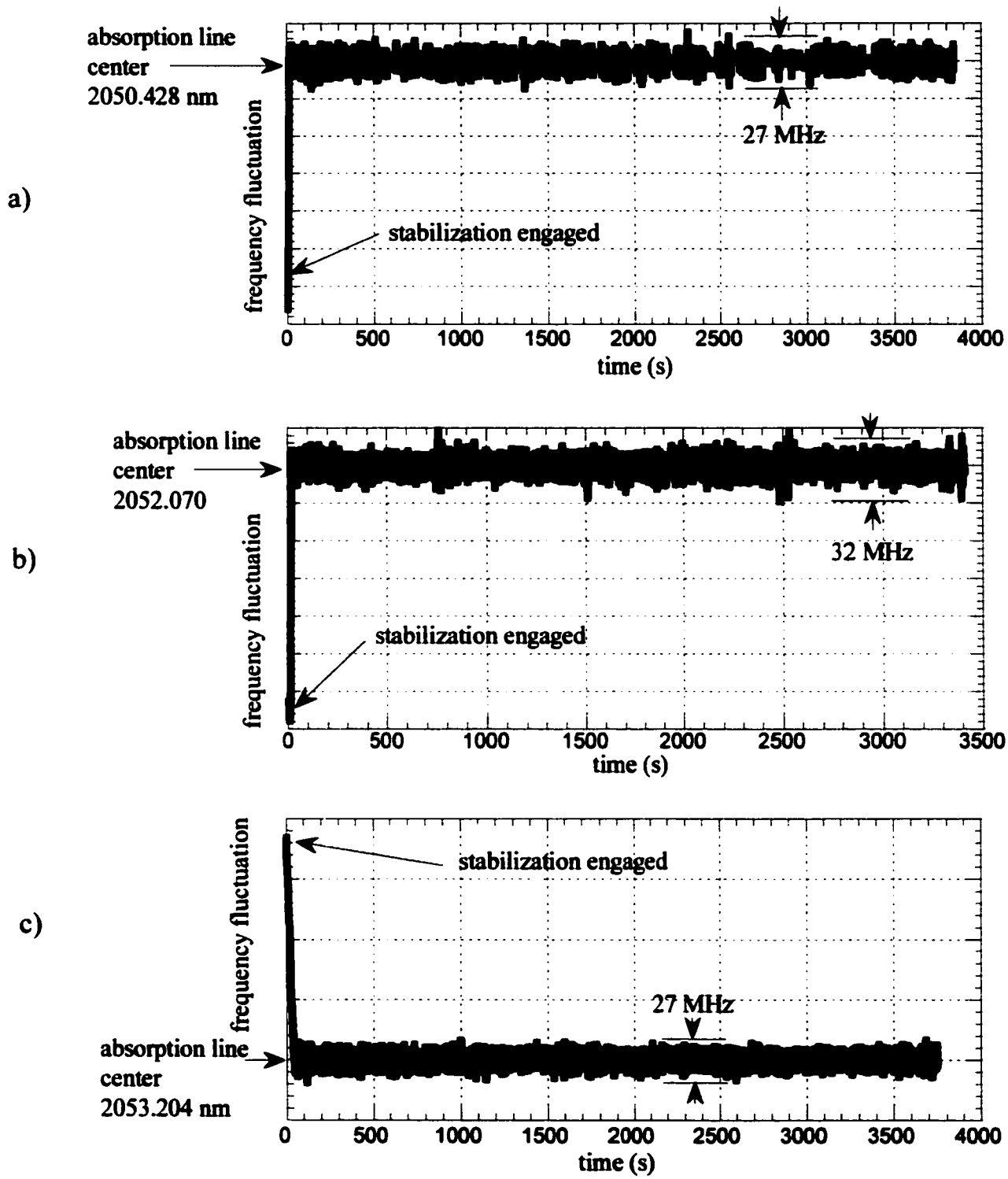

Figure 5.4: Stabilization of Ho:Tm:YLF laser to three different absorption lines of carbon dioxide. Line centers are at a) 2050.428 nm, b) 2052.070 nm, and c) 2053.204 nm.

noise exists in several components of the feedback control loop. For example, there is noise in conversion of the digital control signal to an analog signal and in the analog addition of the control signal to the sinusoidal modulation voltage. Second, there is inherent mechanical instability in the laser cavity against which the control loop must struggle. The mechanical design of the laser creates an inherent limit on stability by the small motion of the resonator optics. The effects of mechanical perturbation were readily seen by observing the error signal in the stabilized state and gently tapping the optical table near the base of the laser. Strong swings in the error signal occurred with every tap, for which the feedback loop quickly compensated. The biggest source of vibration in normal laser operation is water circulating through the base of the laser to remove heat from the thermoelectric cooler.

5.3 Frequency Stabilization to Water Vapor

The same control loop used for stabilization to carbon dioxide was applied to the water vapor absorption line centered at 2050.532 nm. The modulation parameters and resulting feedback error signal were identical to those presented in Section 4.5. Figure 5.4 shows the frequency deviation from line center without and with the control loop engaged.

Comparison of the stabilization to water vapor to that of carbon dioxide shows that a tighter lock was achieved to carbon dioxide—within 23 MHz of water vapor line center as opposed to 13 MHz for carbon dioxide. The carbon dioxide stabilization is more effective because the lines used are approximately ten times stronger than the water vapor line. Stronger absorption features result in a locking descriminant of a higher

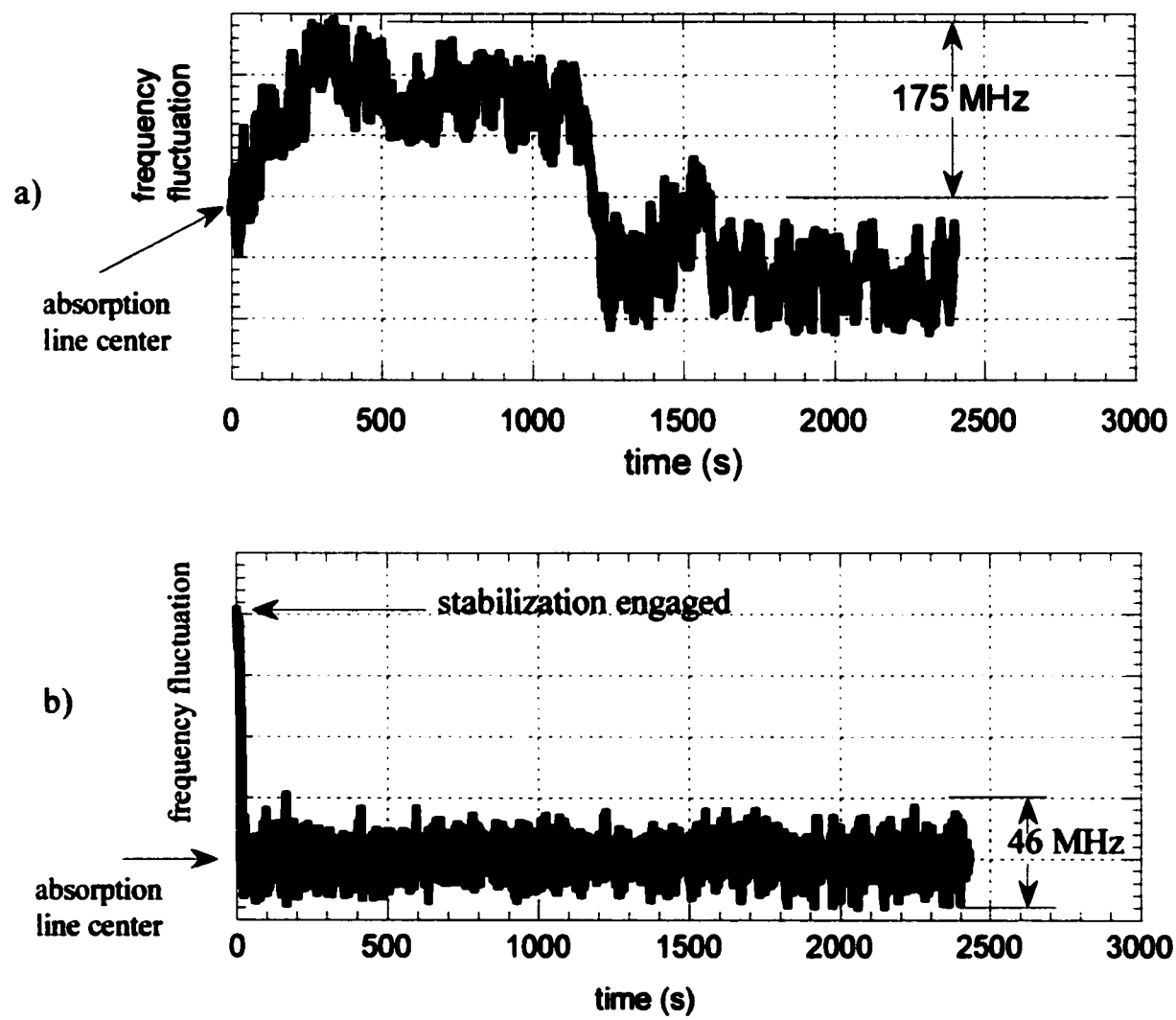

Figure 5.5: Frequency fluctuation without (a) and with (b) stabilization to water vapor line centered at 2050.532 nm. Fluctuations are measured by the first-harmonic error signal.

signal-to-noise ratio. With this stronger signal more sensitivity is offered to excursions from line center, so a higher level of stabilization is achieved. Still stabilization to within 23 MHz is within the requirement for 1 pm (71 MHz), and acceptable for use in the lidar.

CHAPTER 6

INJECTION SEEDING

In this chapter results are presented on using the stabilized CW master oscillator to injection seed a pulsed Ho:Tm:YLF laser. Injection seeding was briefly described in Chapter 2 as a means to achieve a single-frequency spectrum from a pulsed laser. The utility of injection seeding can now be extended with the advent of the stabilized CW master oscillator described in Chapters 3 through 5. Not only can a single-frequency spectrum be forced onto the pulsed laser, but the precise tunability of the seed laser can be imparted to the pulsed laser. The precise wavelength control that will be shown in this chapter is unprecedented for a pulsed laser in this wavelength range. Toward this demonstration Section 6.1 describes the theory behind injection seeding and Section 6.2 describes experiments in tuning and stabilization of the pulsed laser.

6.1 Injection Seeding Theory

Pulsed solid-state lasers typically run with a large linewidth and a high degree of frequency drift. Intracavity optics, such as birefringent filters and etalons, can be used to narrow the linewidth to subpicometer width. This is the scheme employed to narrow the CW master oscillator. However, the fluence circulating inside a pulsed laser can easily be high enough to damage an intracavity optic. Injection seeding offers an alternative technique for spectral control of a pulsed laser.

Injection seeding uses a narrow linewidth laser, called a seed source, to impart spectral purity to a pulsed oscillator. The beam from the seed source is mode matched to

the oscillator through either the output coupler or from a reflection off an intracavity element. Without the seed source, the pulse builds up from spontaneous emission in many modes. But with the seed source, the pulsed oscillator has an initial source of photons to amplify which may be in a single mode of the pulsed laser cavity. If the narrowband seed source is more powerful that the broadband spontaneous emission noise, then the pulse will build up from the coherent seed photons, which results in narrow spectral output.

An understanding of injection seeding is based on two fundamental concepts.[44] First, the seed energy competes with noise sources in capturing laser gain. Obviously, the seed power must be greater than the noise power. Second, while seeding may occur at any frequency, the pulsed oscillator will lase only on its longitudinal modes. The longitudinal modes selected are those adjacent to or within the injection seed frequency spectrum. The closer the seed frequency is to one of the longitudinal modes, the larger the power in that mode.

Lachambre et al. suggest a simple model for seeding based on the interplay between competition with noise and the extent of detuning from an oscillator longitudinal mode.[65] Results of their model indicate three regimes of seeding: first, a spontaneous oscillation zone for large detuning where no seeding occurs; second, a mode selection zone corresponding to moderate detuning and moderate seed power where the oscillator lases on a single longitudinal mode because of the presence of the seed; and third, a frequency-locking zone for little detuning and large seed energy in which the oscillator lases at the seed frequency.

Although insightful, this model does not entirely agree with experimental results. A more practical model and experimental verification with a $Ti:Al_2O_3$ oscillator indicate

that the mode selection zone is not characterized by single-mode oscillation.[26,66] Rather, for common cavity lengths (1.5 m) and typical seed source powers, two longitudinal modes are selected. A multiple longitudinal mode spectrum is unsatisfactory for a coherent lidar because the modes would all mix together in the heterodyne detection. To force a single mode to lase, the oscillator cavity length must be actively controlled to match the seed frequency—this regime of operation corresponds to the frequency-locking zone described by Lechambre et al.

A robust means for achieving the active matching of the pulsed laser cavity and injection seed was suggested by Henderson et al.[27] This technique, employed in the lidar described in Chapter 2, involves ramping the laser cavity length with a PZT-driven mirror during the pumping interval. A resonance between the seed and pulsed laser cavity, detected by a photodiode outside the cavity, serves as an indication to trigger the laser Q-switch.

6.2 Injection Seeding Experiment

The layout of the experiment is shown in Figure 6.1, in which the stabilized CW master oscillator is seeding a pulsed Ho:Tm:YLF laser. This pulsed laser is different from the one used in Chapter 2. In this improved design the output energy has been increased to as much as 100 mJ per pulse at 5 Hz repetition rate with a pulse width of 190 ns.[67] It's built from a 2 cm long rod of 0.4 % holmium and 6 % thulium doped into YLF with both ends of the rod diffusion bonded to undoped YLF. Ten quasi-CW arrays of diode lasers provide a total side pump energy of 3.5 J. A 2.7 m ring resonator is formed

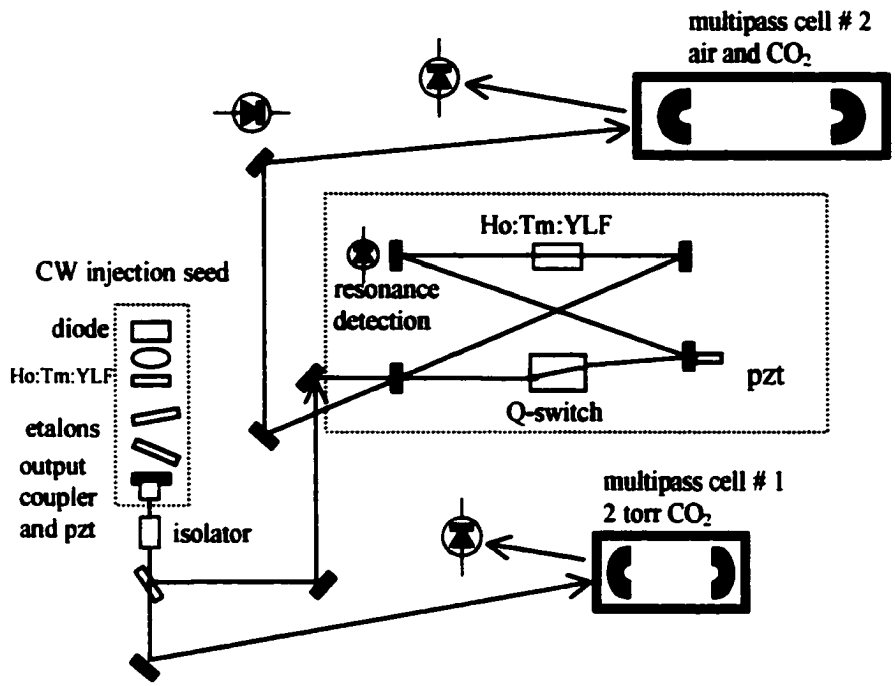

Figure 6.1: Setup of injection seeding experiment. The CW injection seed is referenced to the carbon dioxide absorption features as described in Chapters 4 and 5.

around the crystal in a bow-tie configuration, including an acousto-optic Q-switch. The ramp-and-fire technique that was used in Chapter 2 is repeated here.

To assess the wavelength properties of the pulsed laser, 10% of its output is split off and aligned to a multipass cell of 75 m path length of a mixture of air and carbon dioxide. Diluting the carbon dioxide with air was required since pure carbon dioxide at this path length and pressures less than 10 torr presented 100 % absorption at line center. Figure 6.2 shows the laser pulse before and after the absorption cell. Analysis of these temporal pulses indicates that the spectrum of the laser output is single frequency, because more than one mode oscillating would result in mode beating superimposed on the pulse. A profile of a multimode pulse, made by deactivating the ramp-and-fire circuitry, is shown in Figure 6.3. The temporal profile in this case shows a modulation caused by the mixing of the modes; this modulation shows up very strongly in the corresponding FFT.

The pulse detected after the cell is delayed in time with respect to the pulse before the cell due to the 75 m path inside the cell. An additional path length is created in the distance required to direct the beam in and out of the absorption cell.

Tunability of the pulsed laser was tested by sweeping the seed laser wavelength across an absorption feature and observing if the pulsed laser also scanned across the absorption line. The results of this experiment are presented in Figure 6.4. The top graph in this figure shows the transmission of the injection seed laser through multipass cell # 1 as the PZT attached to its output coupler is ramped to change the output wavelength. The absorption is seen to peak at 157 V with a corresponding center wavelength of 2050.428 nm. In addition to the transmission variation due to the carbon dioxide absorption, the parabolic variation described in Chapter 4 is seen in intensity as the laser is tuned. The

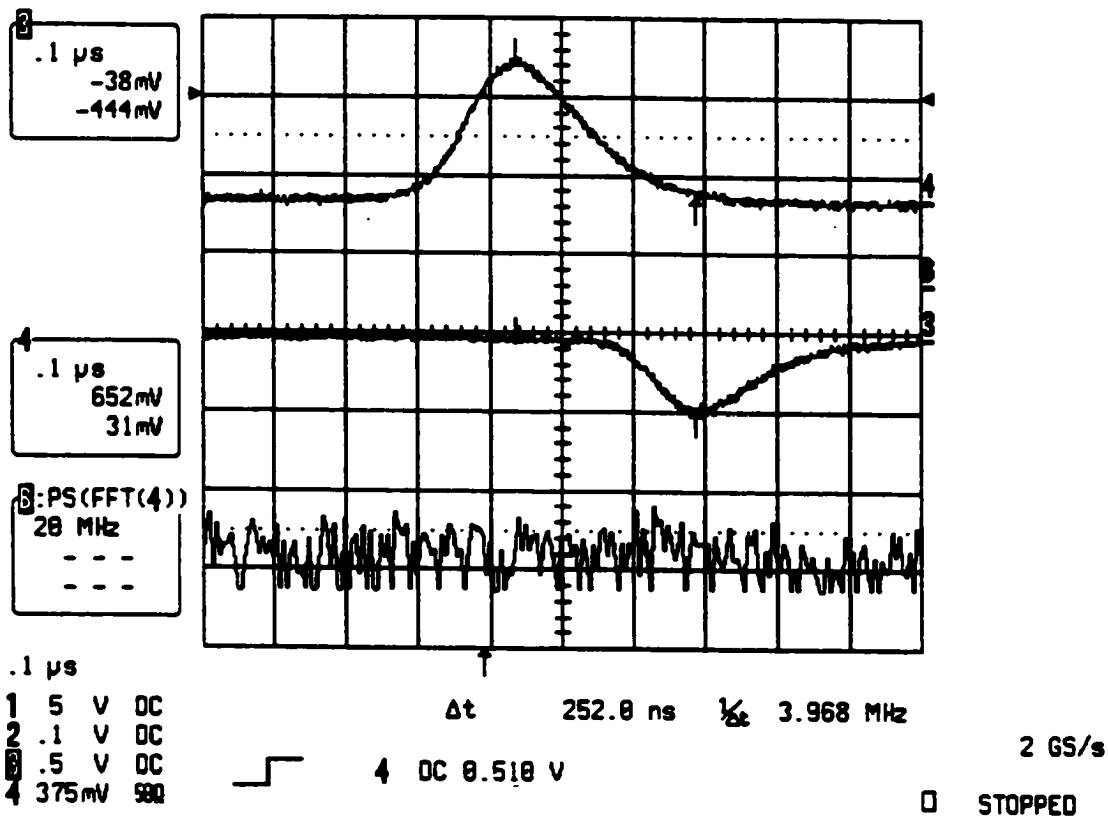

Figure 6.2: Oscilloscope traces of laser pulses before (upper trace) and after (middle trace) absorption cell #2. One pulse is positive going and the other is negative going due to the opposite biases of the detectors. A fast Fourier (FFT) is shown (lower trace) of the pulse before the cell indicating no mode beating, verifying that the laser is operating single frequency.

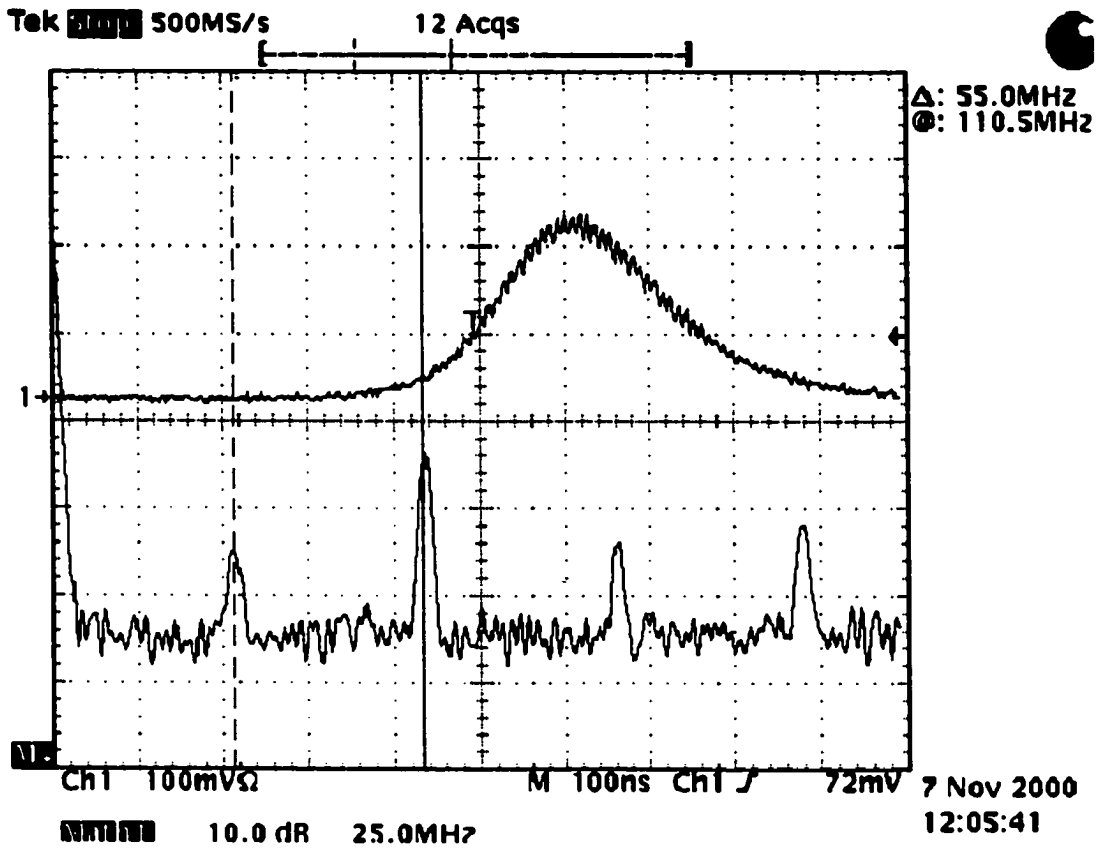

Figure 6.3: Oscilloscope trace of laser pulse with multimode spectrum. Mode beating is apparent in the modulation of the temporal profile and becomes obvious when viewed with an FFT. The frequency of the mode beating is 107.8 MHz, corresponding to the free spectral range of the pulsed laser cavity.

tuning range corresponding to the full PZT voltage excursion shown here is 19 pm (1.35 GHz); the width of the absorption line is 5 pm at full-width half maximum.

The lower two graphs of Figure 6.4 show the output of the pulsed laser detected before and after the absorption cell. These sequences of pulses were detected with the same acquisition parameters of Figure 6.2, but with the oscilloscope set to display a sequence of triggers. Figure 6.4b shows that the output directly from the pulsed laser maintains the same amplitude as the wavelength of the injection-seed laser is ramped, as is expected. But the pulses after multipass cell # 2, shown in Figure 6.4c, show a strong variation in amplitude, sweeping out the gaussian shape of the absorption line. The peak absorption of the pulsed laser matches that of the injection seed, indicating that the pulsed laser wavelength tracks the seed. This fine control of the pulse laser allows tuning well within 1 pm of absorption line center.

Experiments were also performed to lock the pulsed laser on-line center by stabilizing the injection seed. With the injection seed stabilized to line center, as described in Chapter 5, the pulsed laser is also expected to be held near line center. The goal in this next experiment is to determine how well the pulsed laser tracks the seed while the CW master oscillator is locked on line center. The data of Figure 6.4 shows that the pulsed laser tracked the scanning seed laser to well within a picometer, and performance of the stabilized condition was initially made by measurements similar to those of Figure 6.4. With the seed laser locked to cell #1, transmission of the pulsed laser through cell #2 was used to monitor if the pulsed laser remained at peak absorption. Variation of the pulsed laser wavelength away from line center would result in an increase of the amplitude of the pulse detected after the cell. No significant change in the transmitted pulse amplitude was observed for over an hour, aside from the 5% amplitude

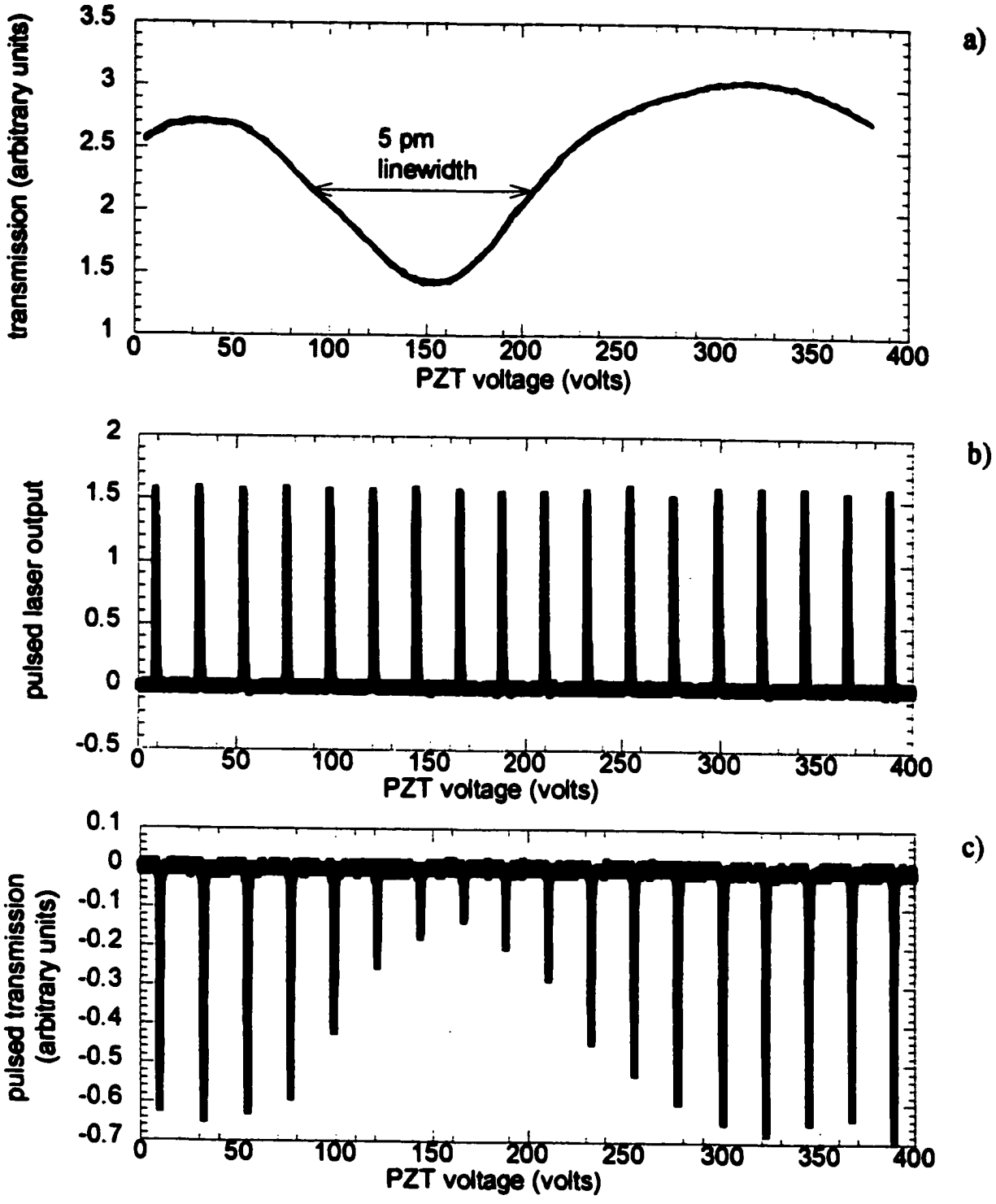

Figure 6.4: Transmission of the seed laser through a carbon dioxide line (a) as output coupler PZT voltage is ramped producing a plot similar to Figure 4.10a. Corresponding pulsed laser output (b) and transmission of pulsed laser through carbon dioxide line (c). The line scanned is centered at 2050.428 nm.

variation inherent to the pulsed laser. This amplitude variation limits the sensitivity with which this measurement of pulsed laser stability can be made.

A more sensitive measurement was thus devised based on heterodyning the pulsed laser output with a portion of the seed laser. As diagrammed in Figure 6.5, the CW master oscillator has been split into three beams. One beam goes through a mulipass cell so that the seed laser can be locked to the carbon dioxide absorption line. A second beam is used to seed the pulsed laser. The third beam is diffracted by an acousto-optic modulator to be shifted by 105 MHz before being focused into a polarization-maintaining fiber. This fiber-coupled beam serves as the local oscillator for the heterodyne measurement with an intermediate frequency of 105 MHz. This intermediate frequency is used in order to discern to which side of absorption line center the pulsed oscillator may drift. This scheme of splitting and frequency shifting the CW master oscillator was also used in the lidar system described in Chapter 2, Furthermore, the monitoring of the heterodyne signal between the pulse and local oscillator is used in the lidar system to monitor and correct for this drift. The difference in this experiment and that of Chapter 2 is that the CW master oscillator is locked onto line center.

To perform the experiment the CW master oscillator was first stabilized to the carbon dioxide absorption centered at 2050.428 nm. Samples of the heterodyne signal were then recorded for 1000 consecutive shots of the pulsed laser. Each heterodyne signal was analyzed for it beat signal by a fast Fourier transform. With each pulse sampled at 500 Ms/s for 500 points, the resolution of the beat signal measurement is 500 kHz. The record of the of the beat signal frequency is shown in Figure 6.6. Most of the pulses were at 105 MHz offset, indicating no measurable deviation of the pulsed laser from the injection seed. However, 50 pulses had a slight deviation away from the seed

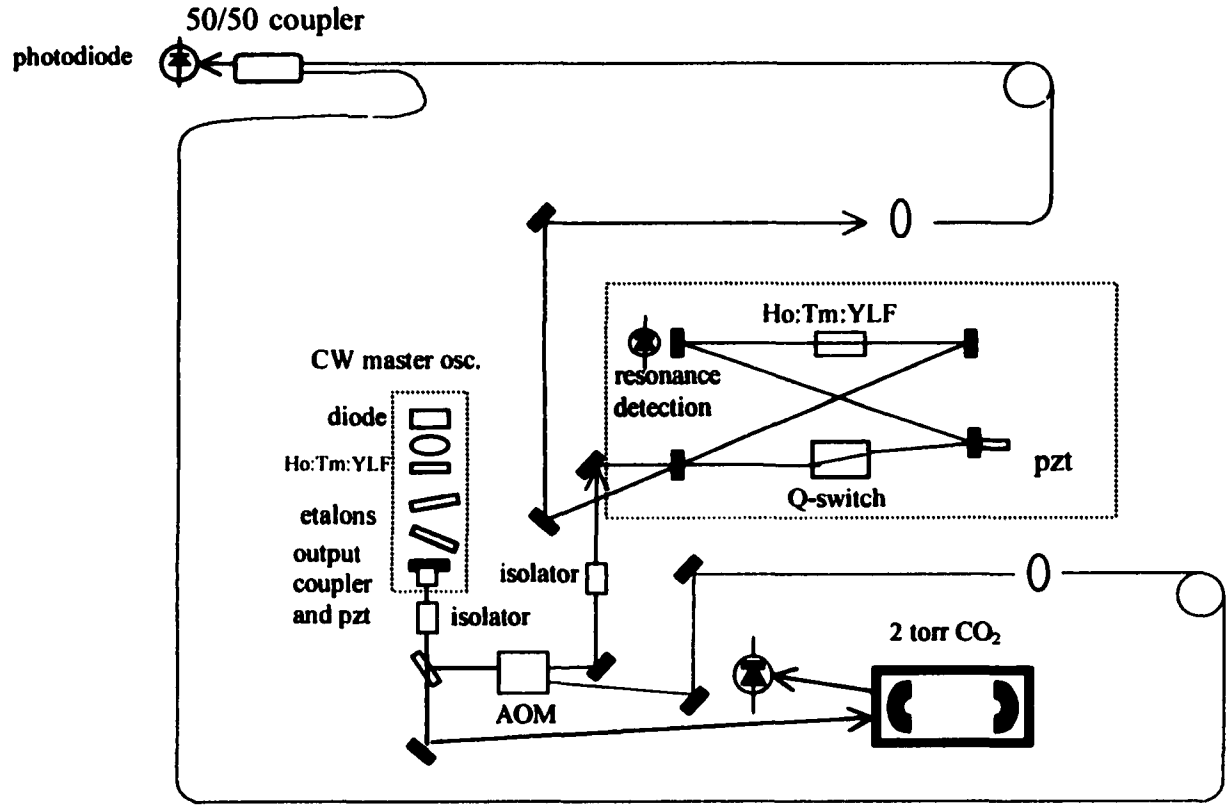

Figure 6.5: Layout of heterodyne experiment to determine wavelength deviation of pulsed laser from injection seed.

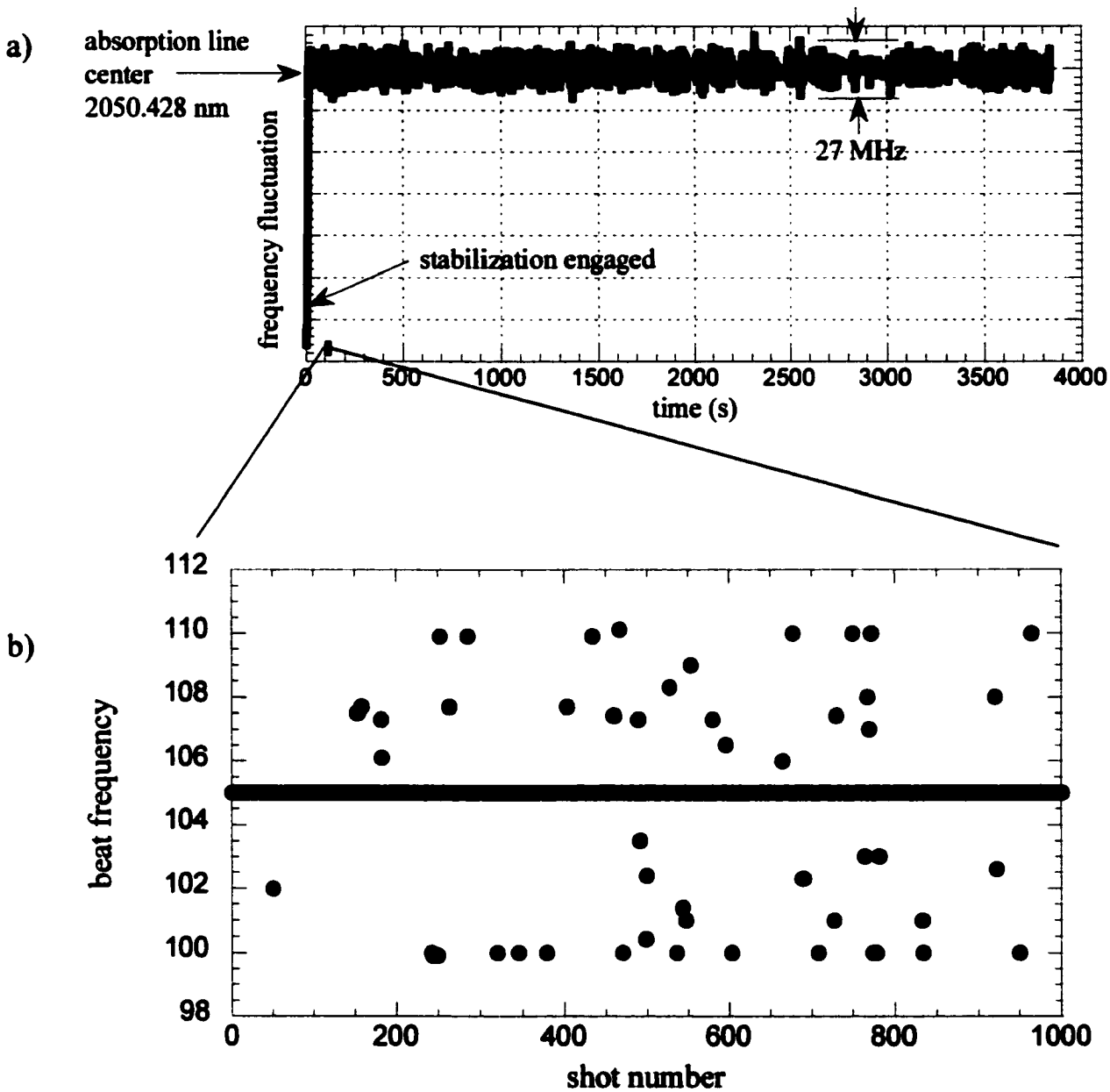

Figure 6.6: a) stabilization of CW laser to absorption line of carbon dioxide at 2050.428 nm and b) intermediate frequency of heterodyne signal showing frequency offset between pulsed laser and CW laser over a time span of 20 s.

wavelength by as much as 5 MHz. With the seed laser known to within 13.5 MHz of line center and the pulsed laser offset at the most by 5 MHz, the transmitted wavelength can only be 18.5 MHz from line center in the worst case.

The results presented in this section show that the stabilized CW master oscillator performs well as an injection seed source. The phase modulation used in the absorption line stabilization does not adversely affect the seeding process—the pulsed laser output consists of a single-frequency spectrum. Furthermore, it has been shown that the pulsed laser wavelength precisely follows that of the seed source. If the CW master oscillator is stabilized onto an absorption line, then so is the pulsed laser. If the CW master oscillator is scanned in wavelength, then so is the pulsed laser. A tunability of the pulsed laser has thus been demonstrated with enough resolution to make DIAL measurements.

CHAPTER 7

SECOND-GENERATION COHERENT DIFFERENTIAL ABSORPTION LIDAR

With the newly developed stabilized CW master oscillator and the availability of a higher energy pulsed laser, the coherent DIAL results presented in Chapter 2 are expected to improve. This chapter describes lidar results incorporating these improvements in a second-generation coherent DIAL. In this implementation carbon dioxide was probed, as opposed to water vapor in Chapter 2. There are three reasons for pursuing a carbon dioxide measurement in this chapter. First, there has been a recent surge in interest among atmospheric scientists for lidar measurement of carbon dioxide. Second, it's desired to show application of this lidar technology to both gases. And third, the concentration of carbon dioxide is relatively fixed (compared to water vapor), so it serves as a good calibration reference to which to judge the accuracy of the DIAL measurement.

A further question to answer in this experiment is if the modulation applied to the master oscillator adversely affects its operation as a local oscillator. It was proven in Chapter 6 that the modulation has no affect on the master oscillator as an injection seed source, but the master oscillator must also function as a local oscillator. Since the modulation occurs over a long time scale compared to the time in which atmospheric return signals are received, no effect upon the local oscillator function is expected. Still, proper local oscillator functionality must be validated.

The design of the lidar, diagrammed in Figure 7.1, builds upon the developments of the previous chapters. The injection seeding setup of Chapter 6 is repeated here

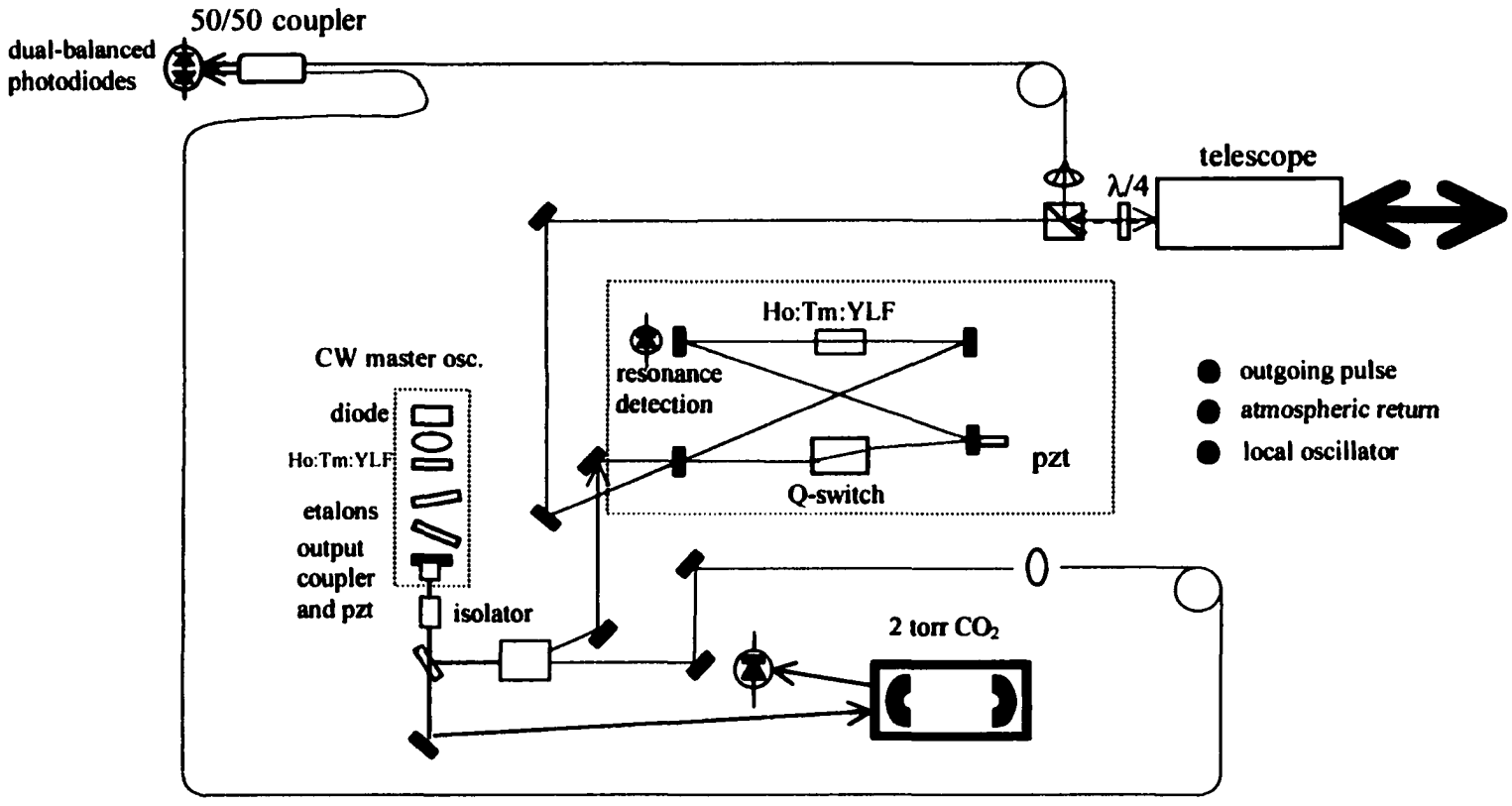

Figure 7.1: Layout of second-generation coherent DIAL.

to form the transmitter for the lidar, but with the acousto-optic modulator (AOM) providing an extra function. In addition to setting the intermediate frequency at 105 MHz, the AOM is used to split off a beam to serve as the local oscillator. The CW master oscillator is locked to absorption line center, as developed in Chapter 5, for the on-line measurement.

The receiver design is identical to the one presented in Chapter 2. The output of the pulsed laser is directed toward an off-axis paraboloid telescope, which serves to both expand the transmitted beam to a 4-inch diameter and collect the backscatter from the atmosphere. The transmitted and received paths are separated by the polarization relationship imposed by a polarizing beam splitter and a quarter waveplate. The same photodetector used in Chapter 2, InGaAsP photodiodes in a dual-balanced configuration, are used again here to heterodyne the local oscillator and atmospheric return.

Demonstration of the lidar follows the approach presented in Chapter 2, with measurement of wind and carbon dioxide addressed in separate sections. Section 7.1 explores wind measurement and Section 7.2 addresses the DIAL measurement.

7.1 Wind Measurement

The real-time processing for making wind profiles that was used for the data of Figure 2.6 was not available for this experiment. Signals were instead analyzed manually using an oscilloscope and personal computer following the algorithms for processing that would ordinarily be performed by the real-time processor. Computer-controlled scanning of the lidar beam was also not available, so a profile was made of wind speed and direction versus altitude (in which complex scanning is not required). The configuration

for such a measurement is to direct the lidar beam at a 45° elevation for two orthogonal azimuths. Line of sight velocities along these orthogonal azimuths yield two components of the wind field, which can be vector summed to find the wind speed and direction as a function of altitude. Such a calculation has been performed and graphed in Figure 7.2.

Data prior to 500 m range is not displayed because prior to this range the heterodyne detectors are recovering from saturation by the outgoing laser pulse. This effect was also observed in the experiments of Chapter 2, but the saturation subsided by 200 m range. The saturation range is further in this second-generation system because the pulse energy is about 50 times greater. The perturbation from internal scatter consequently has a stronger effect. The benefit, of course, of a stronger energy is a longer-range capability and higher SNR. In the data of Figure 7.2 the maximum range is an altitude of 1800 m, where the top of the atmospheric boundary layer occurred.

The measurement of wind speed shown in Figure 7.2a indicates that the wind is increasing with altitude, a phenomenon to be expected since friction with the ground slows wind speed. This was also observed in Figure 2.6. The measurement of wind direction of Figure 7.2b shows an interesting occurrence as the wind direction sweeps through a wide range with altitude. The force that would be exerted on an object rising from the ground, such as a helium balloon, would be such that the object would move in a spiral. Albeit this spiral force would be gentle effect, since the wind speed is low. Abrupt changes in wind direction, called a wind shear, are commonly encountered in the atmosphere when there is convective activity creating updrafts of air. The data of Figure 7.2 is an example of a weak wind shear, but wind shear can occur with such strength that a hazard can be posed for an aircraft on approach to a runway. Wind shear has been reported as a contributing factor in aircraft accidents in at least 28 incidents, including

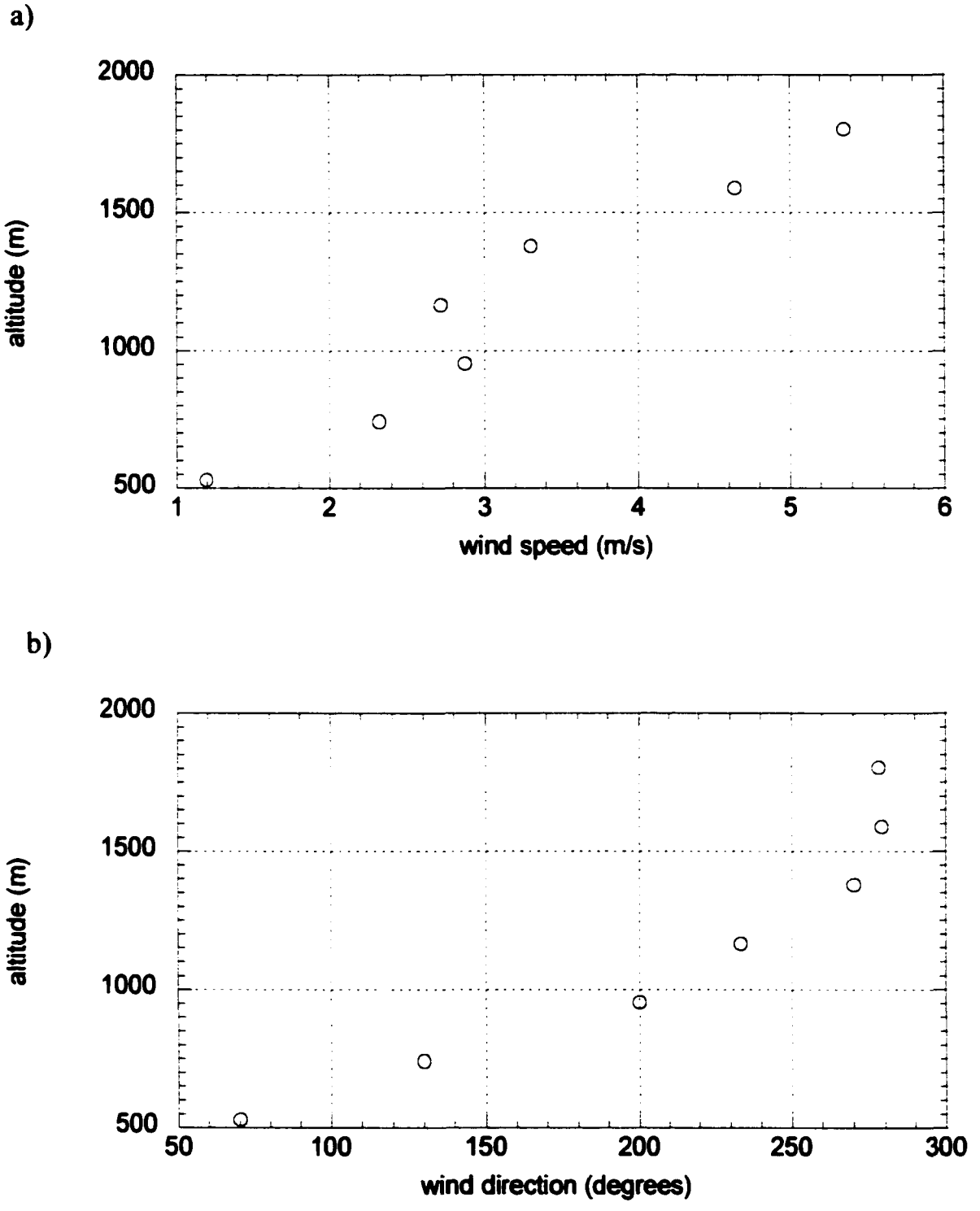

Figure 7.2: Wind speed and direction versus altitude as measured by lidar. Weather station measurements at ground level were 1.3 m/s from the east.

600 fatalities, between 1974 and 1996.[5] As demonstrated by Figure 7.2, even very weak wind shear can be detected with a coherent lidar. Coherent lidar could then be used as a monitor for dangerous wind shear at airports, and several experiments have been carried out to investigate such an application from both ground and aircraft-based systems.[5, 68]

The wind measurements made by this second-generation lidar have shown a performance similar to the results of Chapter 2 and of coherent lidars reported in the literature. The local oscillator was modulated, though not locked on line, during these experiments to determine if the modulation affected the function of the local oscillator. No degrading effects from the local oscillator were found, as was expected since the modulation occurs over time scales very long compared to the times over which the atmospheric return in processed. The more challenging test is to see how well the second-generation system works for a DIAL measurement.

7.2 DIAL Measurement of Carbon Dioxide

The method for making the DIAL measurement of carbon dioxide is the same presented in Chapter 2 for the measurement of water vapor. The CW master oscillator, and therefore the pulsed laser, is locked onto the absorption line centered at 2050.428 nm. The atmospheric return from 100 shots was averaged and recorded with the data acquisition system of Figure 2.7. The lock for the on-line laser was shut down, the CW master oscillator was tuned off line to a wavelength of 2051.658 nm, and another 100 shots were averaged. Approximately 5 minutes was required to make the transition from on line to off line. The atmospheric return signals are plotted in Figure 7.3 with the lidar beam directed vertically.

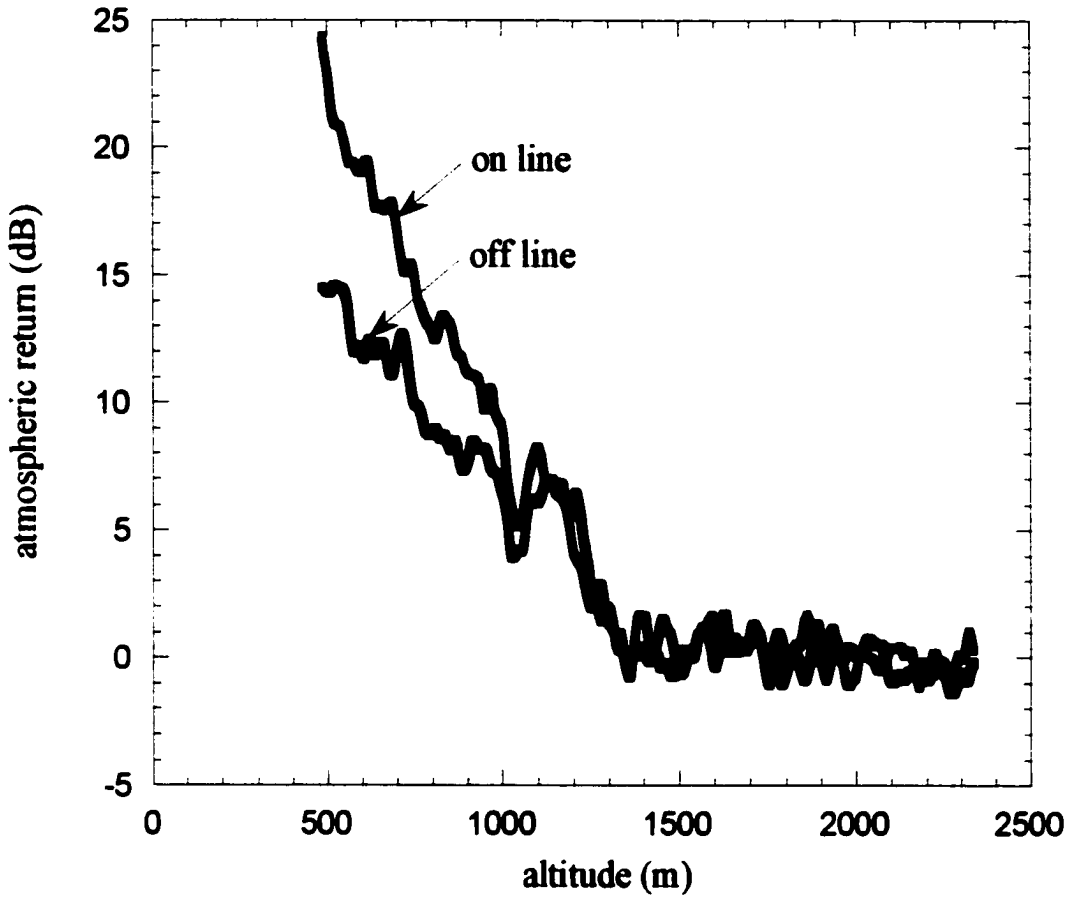

Figure 7.3: Carbon dioxide DIAL measurement.

The on-line signal starts at a higher level because there was more pulse energy available with the laser tuned on line and more power available for the local oscillator with the laser tuned on line. The transmitted energy was 35 mJ for the on-line data and 25 mJ for the off-line data. This is a substantial increase in energy over the first-generation lidar of Chapter 2, and results in a higher SNR with which to work. The differential absorption is obvious in Figure 7.3 with the on-line signal attenuated at a faster rate than the off-line signal. The top of the atmospheric boundary layer is seen at 1.3 km altitude by the abrupt drop in aerosol concentration at this altitude. Another feature to note is that the aerosol profile is different between the on-line and off-line signals, caused by the long time required between the two measurements.

As was performed in the data of Chapter 2, the aerosol profiles were smoothed in an attempt to average out these aerosol concentration differences. The smoothed profiles are presented in Figure 7.4, with the four points indicated used for a DIAL calculation. Equation 1.15 is used for this calculation, taking $\Delta\sigma = 6.945 \times 10^{-22}$ cm^2 as indicated by the HITRAN database.[25] The calculated concentration based on the four points of Figure 6.4 is 457 ppm. Several studies of carbon dioxide by point sensors indicate that the concentration should be 355 ppm, implying a DIAL measurement error of 29%

A 29% error is a substantial reduction from the 86% error found in Chapter 2. This improvement is attributed to the stabilization of the CW master oscillator to absorption line center. The on-line measurement is now made with the wavelength precisely known.

While a substantial improvement, a 29% error is still not satisfactory for meteorological or scientific applications. An accuracy in water vapor concentration of better than 20% is needed for meteorological needs. Carbon dioxide measurements pose

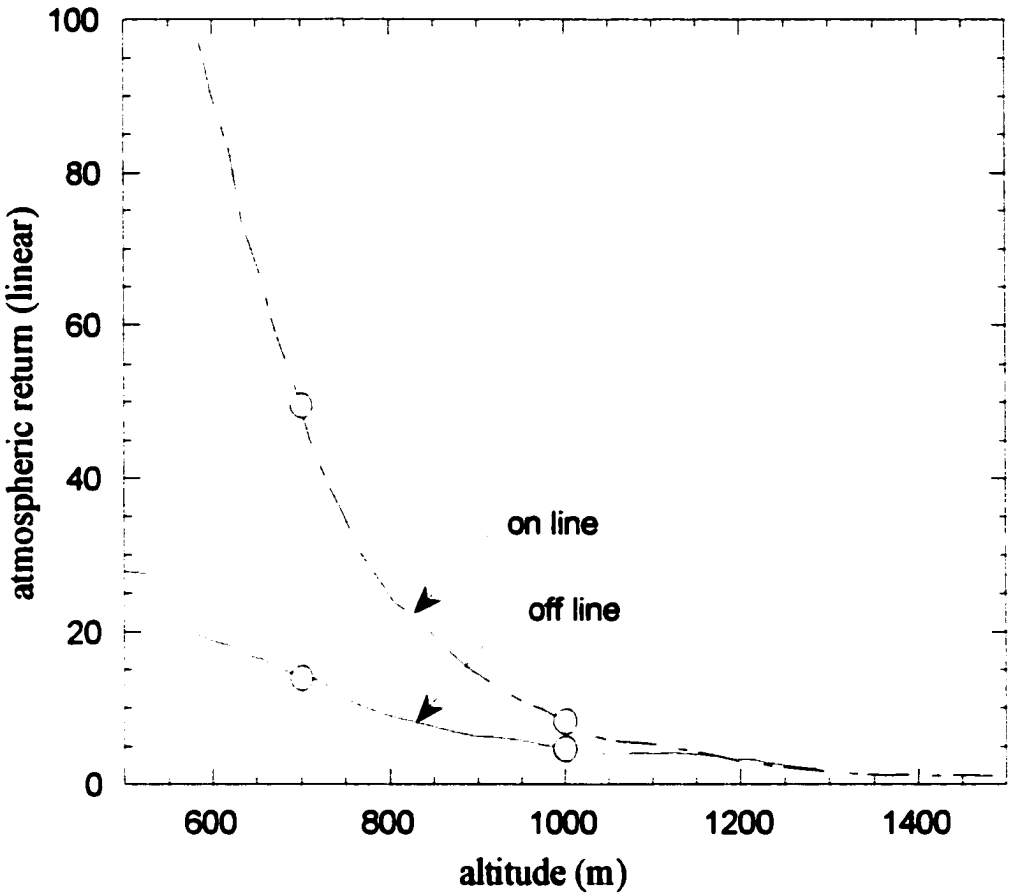

Figure 7.4: Smoothed carbon dioxide DIAL measurement. The four points indicated were used for a DIAL calculation.

an even greater challenge with a requirement for better than 1% accuracy in order to meet scientific needs to determine small-scale changes of a large background level.

A remaining source of error is manifest in the differences in the aerosol profiles between the on-line and off-line data of Figures 2.8 and 7.3. The aerosol concentration of the atmosphere has changed over the time required to switch from the on-line to off-line measurements. These differences in aerosol concentration lead to differences in slopes that mimic differential absorption. As an illustration of this effect consecutive aerosol profiles were made at the off-line wavelength once every 5 minutes over a span of 15 minutes, as plotted in Figure 7.5. Marked changes are seen in the aerosol profiles, with the slope of the data changing strongly from one data set to the next. Taking 5 minutes between on and off-line measurements, as was done for the data of Figure 7.3, is then obviously too long. The data of Figure 7.5 is an extreme situation of rapid changes in aerosol profiles, made when there was strong convective activity prior to precipitation. This convection is characterized by turbulent updrafts that vigorously churn the aerosols within the boundary layer.

In order to solve this problem limiting DIAL accuracy, the time between the on and off-line profiles must be reduced. Observation of continuously flowing data, of which Figure 7.5 are samples, indicates that both measurements should be made in less than ones minute. The best approach would be to alternate on and off-line pulses, so that both measurements would be made in less than a second. These on/off pairs can then be interleaved in a long series, separated, and then averaged. Designs are presented in the next chapter for implementing a rapid switching between the on and off wavelengths.

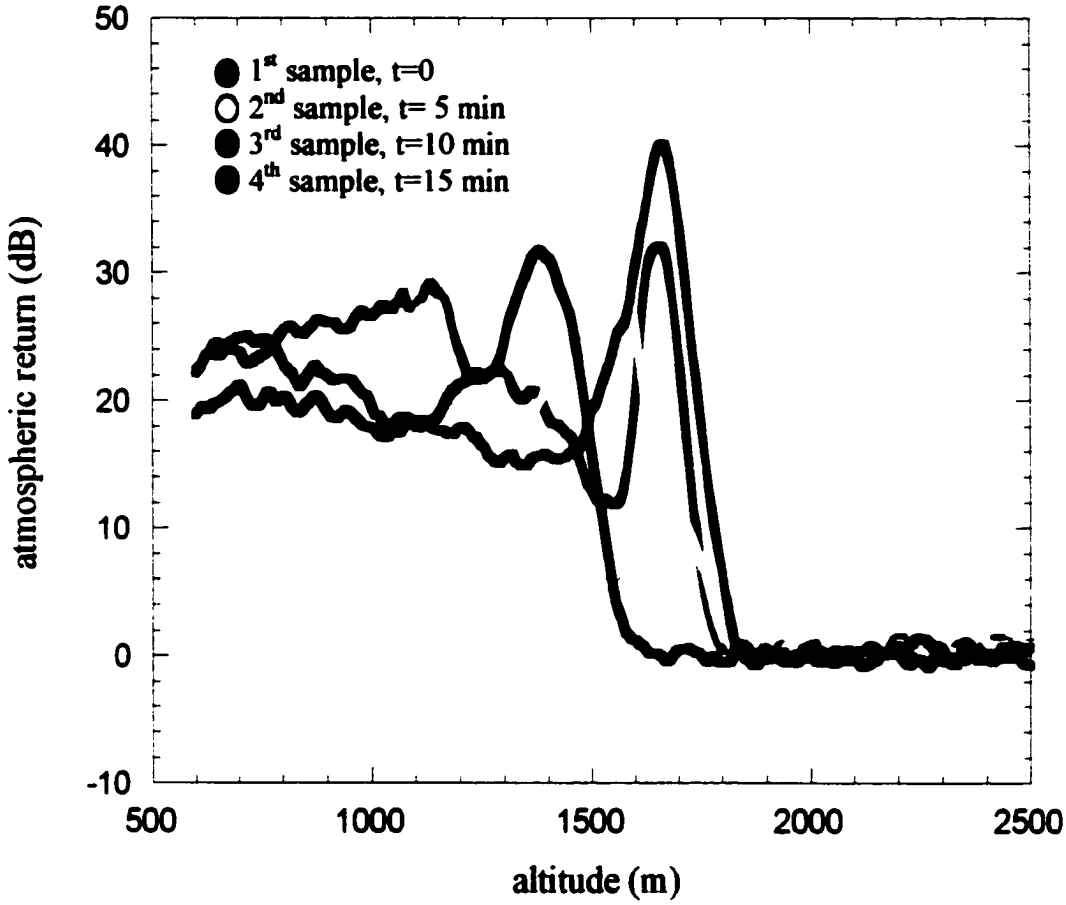

Figure 7.5: Evolution of aerosol profile in the atmospheric boundary layer over a span of 15 minutes sampled every 5 minutes.

CHAPTER 8

CONCLUSION

The research presented in this dissertation has shown the possibility of making combined wind and DIAL measurements with a coherent lidar. This is the first demonstration of this combined technique using a solid-state laser, which also offers the added benefit of an eye-safe wavelength at 2 μm. DIAL detection was made of both water vapor and carbon dioxide, showing a capability for detection of multiple trace gases. These measurements also represent the first DIAL detection of carbon dioxide. A Ho:Tm:YLF laser has also been built with an unprecedented capability for spectral control, offering a single-frequency spectrum at an absolute wavelength accuracy of less than 1 pm. This laser was stabilized to absorption lines of both water vapor and carbon dioxide, representing the first stabilized laser at or within 500 nm of the 2 μm wavelength.

Wind measurements were shown to a precision better than 0.5 m/s, giving a resolution suited to a variety of meteorological applications. DIAL measurement accuracy was improved from a preliminary demonstration of 86% to a second-generation accuracy of 29%. This improved performance was allowed by implementing the stabilization technique for the continuous-wave master oscillator. The DIAL measurement accuracy is just on the cusp of offering enough resolution to make useful meteorological measurements of water vapor at better than 20% accuracy. The missing component to bring the accuracy under 20% has been identified in a need to alternate laser pulses between the on and off-line wavelengths. Designs are proposed in Section 8.1 on how to achieve this rapid switching. Section 8.2 explores a suggested improved

design for coherent DIAL measurement of water vapor, with the goal of using a stronger absorption line of water vapor.

Scientific needs for carbon dioxide measurement are of increasing interest due to its suspected role in climate change. No existing instrument is capable of profiling carbon dioxide over long ranges and large geographical areas. The challenge for this measurement is to provide an accuracy of better than 1%. The experiments presented in this research have shown that a Ho:Tm:YLF-based lidar may be able to make such a measurement by deploying it on board an aircraft of satellite. However, it is questionable if a coherent approach can offer such a high accuracy because of its fundamental noise limit due to speckle fluctuations. To approach an accuracy of 1% so many pulses would have to be averaged that a coherent lidar would be impractical from a moving platform. A direct detection lidar is thus favored. Fortunately, the transmitter for such a direct detection lidar is identical to the laser developed in this research, and the design for a matching receiver is discussed in Section 8.2.2.

8.1 Wavelength Switching

As was pointed out in Chapter 7, a substantial source of DIAL error is caused by not switching quickly between the on and off-line measurements, allowing time for the atmosphere to change in its aerosol composition. The best scenario for reducing the interval between measurements is to alternate the wavelengths between pulses. The fastest pulse repetition rate used in this research was the 20 Hz system of Chapter 2, but higher repetition rate systems are anticipated. An attractive option for a short time

between pulses has recently been reported by Yu et al., in which the Ho:Tm:YLF laser is fired twice per pumping cycle.[69] A doublet of pulses is produced at a 5 Hz rate, with the spacing between pulses of the doublet of 400 μs. If one of the pulses of this doublet could be tuned on line and the other off line, then the short time interval between them would ensure that the atmosphere remains constant for the on-line and off-line measurements.

A requirement for the wavelength switching is then to move from one wavelength to the other is less than 100 μs. In the designs presented in Chapters 2 and 7, the on-line and off-line wavelengths were taken from a single laser that was tuned by tilting an etalon. Even if the etalon tilting could be motorized, it is doubtful that a switching time under 100 μs could be achieved. Furthermore, time must also be allowed for the wavelength stabilization to take hold. Hence, the use of two master oscillator lasers is envisioned—one laser is tuned off line and the other is locked on line.

Two methods have been devised for combing these two lasers into a single beam and for quickly switching between the two wavelengths. Figure 8.1 shows one method using an electro-optic Pockels cell as a polarization rotator. The on-line and off-line beams are made collinear by combining them through a polarizing beam splitter. These beams are orthogonally polarized to each other, so both polarizations are presented to the Pockels cell. A polarizer at the output of the cell only allows horizontal polarization to pass, and the Pockels cell serves to select which wavelength is horizontally polarized. With no voltage applied the on-line beam is passed through the Pockels cell and admitted through the polarizer. However, when a half-wave voltage is applied to the Pockels cell then the input polarization is rotated 90°. In this case the off-line beam is selected.

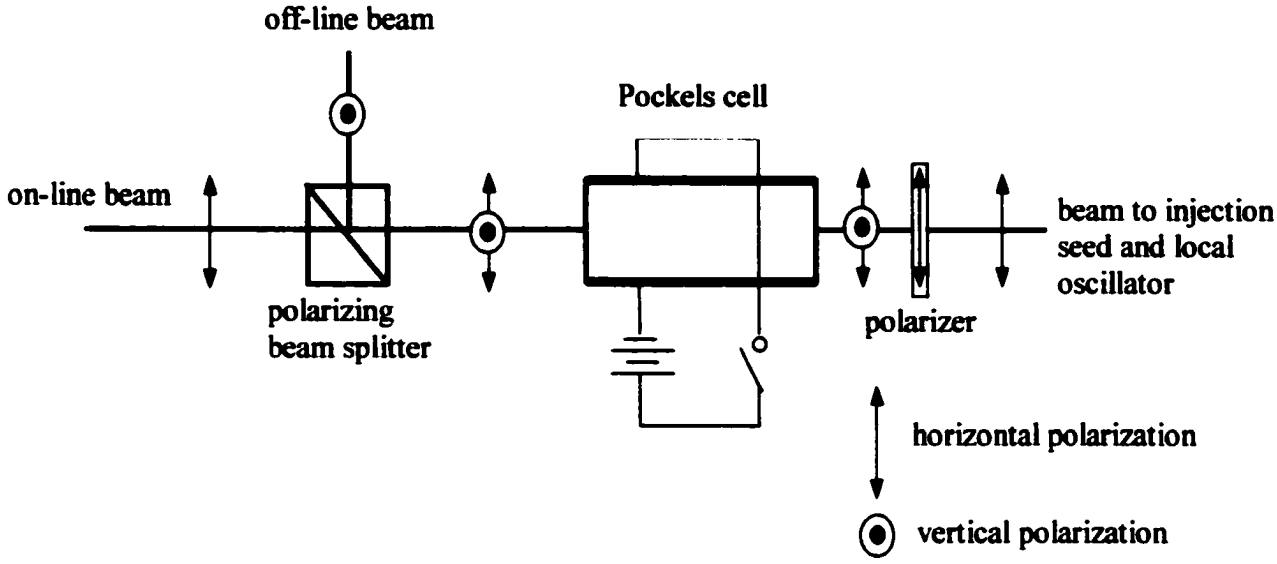

Figure 8.1: Electro-optic design for rapid on-line to off-line switching.

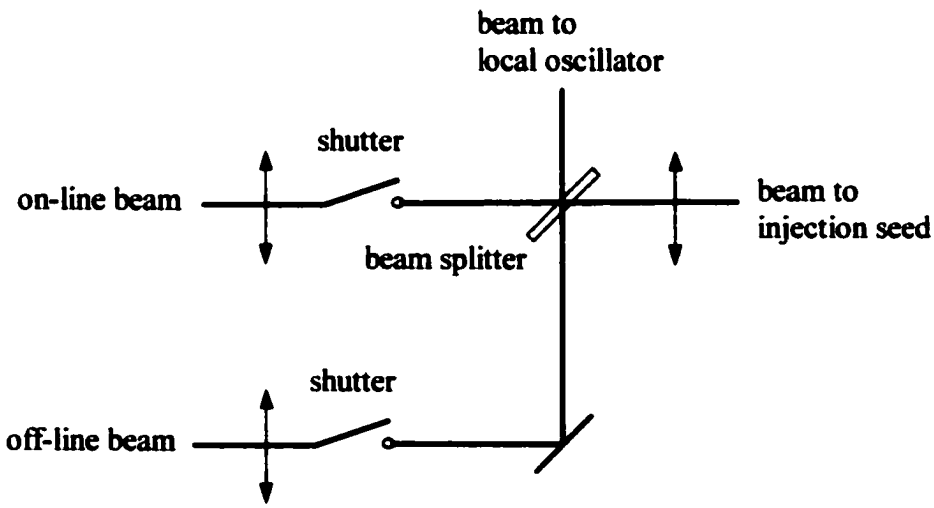

Figure 8.2: Mechanical design for rapid on-line to off-line switching.

Consideration of options for the Pockels cell shows that a possible design is a $LiNbO_3$ crystal, which would require a switching voltage of 700 V. The time required for switching this voltage is 5 μs.[70,71]

An alternate switching design, shown in Figure 8.2, is based on mechanical shutters that block the beam. A shutter is placed in the path of the on-line and off-line beams prior to being combined with a beam splitter. To select a desired wavelength the shutter for that wavelength is opened, while that for the other wavelength is blocked. Rapid activation of the shutter is a challenge for this technique, but shutters with a capability for switching in 100 μs are commercially available.[72]

8.2 Future Lidar Systems

This research has suggested two paths for future lidar systems. Section 8.2.1 discusses an improved DIAL system for combined wind and water vapor measurements. Section 8.2.2 describes a direct-detection DIAL system for high-accuracy profiling of carbon dioxide.

8.2.1 Coherent DIAL for Wind and Water Vapor Profiling

With the addition of a wavelength switching technique, a coherent DIAL should be able to measure water vapor profiles with an accuracy less than the 20% required for meteorological purposes. The wind profiling capability has already been shown to be of a velocity precision less than the 1 m/s required for meteorological applications. A further improvement could be realized to the water vapor measurement results presented

in Chapter 2 by finding an absorption line that is more strongly absorbing then the line used at 2050.532 nm. This would allow the effective range of the lidar to be brought closer. Use of a stronger line would also allow operation in less humid atmospheric conditions such as cold dry winter days. If the absorption were too strong for high humidity conditions, then the laser wavelength could be tuned to the side of the line for less absorption. This option does not exist for an absorption line that is too weak on center. The water vapor line at 2050.532 nm is also overlapped slightly by a carbon dioxide line, which can create confusion as to how much absorption is attributed to each species.

Fortunately, the wavelength region around 2 μm is rich with water vapor absorption lines that can be accessed with a minor modification to the laser designs presented here. This modification entails using a different laser crystal host material; the pumping, cavity designs, and receiver would remain the same. As was discussed in Chapter 3, holmium and thulium in different host laser crystals will offer different wavelength ranges.

The wavelengths over which holmium and thulium can operate extends from 1.85 to 2.15 μm. Davis et al. thus performed a trade-off study using the HITRAN atmospheric database to identify the candidate absorption lines.[73] This 300 nm range of interest, which contains thousands of absorption features, was analyzed with regard to absorption line strength, freedom from overlapping lines, dependence on pressure, and sensitivity to temperature variation. A list was produced, shown in Table 8.1, of the twenty best lines. The line used in Chapter 2 at 2050.532 nm, appears on the list as number 9, with its disadvantages identified in overlap with another line and a strength amenable to use in more humid environments. Consultation with the model developed in Chapter 1, shows

#	λ_{VAC}, μm	E'', cm^{-1}	$X_{L,\ 288.15\ K}$ cm^{-2}	T_S	T_{AW}	T_T	USE:	±5% XR Envelope(Range), Deg. F	±5% AR Envelope(Range), Deg. F	Depth, %	Overlaps (wing)
1	1.9693103	885	9.006 E-23	0.163	0.778	0	S,AW	52-66(14)	49-69(20)	75	Strong(right)
2	1.9734831	709	2.773 E-23	0.580	0.919	0.145	S,T	49-69(20)	44-75(31)	40	Moderate(left)
3	1.9751077	1960	2.811 E-23	0.583	0.959	0.087	S	56-62(6)	55-63(8)	45	minor(left)
4	1.9844298	1079	1.417 E-23	0.758	0.966	0.344	S,T	53-64(11)	53-66(13)	25	minor(right)
5	1.9852294	648	1.047 E-22	0.127	0.723	0	S,AW	48-70(22)	41-78(37)	85	minor(both)
6	2.0209554	842	3.401 E-23	0.494	0.901	0.077	S	52-66(14)	49-71(22)	41	Moderate(both)
7	2.0232844	1059	4.159 E-23	0.430	0.906	0.032	S	53-65(12)	52-66(14)	40	Moderate(both)
8	2.0331959	1122	3.816 E-23	0.466	0.910	0.054	S	53-65(12)	52-66(14)	50	Minor-moderate
9	*2.0505324*	*552*	*9.123 E-24*	*0.832*	*TBD*	*0.532*	*S,T*	*46-73(27)*	*33-92(59)*	*5*	*Moderate-strong*
10	2.0566484	300	1.666 E-23	0.716	TBD	0.332	S,T	23-105(82)	-60-120(180) *	18	Complex
11	2.0576132	1200	1.068 E-23	0.813	TBD	0.440	S,T,	54-64(10)	52-66(14)	21	Complex
12	2.0604538	212	1.356 E-23	0.764	0.945	0.423	S,T	-23-120(143) *	28-91(63)	17	None (left)
13	2.0707304	447	1.047 E-23	0.808	0.954	0.488	S,T	41-80(39)	8-120(112)	23	None
14	2.0777368	42	1.686 E-23	0.708	0.930	0.348	S,T	22-102(80)	45-75(30)	27	Moderate
15	2.0848300	224	1.734 E-26	0.725	0.933	0.328	S,T	-12-120(132)	25-94(69)	22	Moderate
16	2.0938882	79	1.480 E-23	0.744	0.927	0.394	S,T	5-116(111)	42-78(36)	22	Minor
17	2.1833703	224	3.381 E-23	0.513	0.873	0.114	S,AW,T	-12-120(132)	25-94(69)	49	None
18	2.1871061	704	4.169 E-23	0.818	0.969	0.489	S,T	50-69(19)	44-75(31)	17	None
19	2.1882404	285	1.103 E-23	0.808	0.961	0.517	S,T	19-115(96)	-12-115(127)	17	Moderate(left)
20	2.1905247	326	1.235 E-23	0.785	0.954	0.438	S,T	29-96(67)	-60-120(180) *	20	None

Nomenclature:

λ_{VAC} - line center wavelength *in vacuo*; E''- ground-state energy of transition ; X_L - Lorentz cross-section; XR- Relative cross-section(relative to value at 288.15 K) ; AR - Relative absorption coefficient. * denotes widest temperature range for XR or AR category.

T- transmittance along horizontal path; S- 1976 Standard Model Atmosphere; AW- Arctic Winter Model Atmosphere; T-Tropical Model Atmosphere.

Table 8.1: Summary of twenty water vapor lines optimal for measurement of water vapor in the boundary layer. From Davis et al.[73]

that an absorption cross section of greater than 3×10^{-23} cm^2 mol is desired for use in less humid conditions. Table 8.1 shows that several lines exist that are of this cross section. In particular, lines 6 and 7 are attractive because they match the wavelength accessible by the Tm:LuAG laser crystal. Carbon dioxide lines are also within the tuning range of Tm:LuAG.

8.2.2 High Accuracy Direct-Detection DIAL of Carbon Dioxide

While coherent DIAL offers the advantages of a multifunctional ability to measurement both wind and gas concentrations, it suffers from a disadvantage in requiring long averaging times to make accurate DIAL measurements. If a long averaging time were used from an aircraft or satellite, a long distance of geographical area is likely to be smeared to make a single measurement. The science needs for carbon dioxide profiles are for a very high accuracy over a spatial area accessible only from a moving platform. Direct-detection lidars do not require as long an averaging time because their receivers view multiple speckle cells in a single laser pulse. The disadvantage of direct-detection is that is not as sensitive as coherent reception, so greater transmitted pulse energy and a larger area telescope are required. Direct detection is especially problematic at 2 μm wavelength since photodetectors are not as sensitive as their counterparts for visible wavelengths.

A block diagram of a direct-detection lidar for high-accuracy carbon dioxide profiling is shown in Figure 8.3. The laser transmitter is the same as that presented in Chapter 7, with the addition of the two switched injection seed lasers. The receiver consists of a 16-inch diameter Schmidt-Cassegrain telescope, a telescope configuration

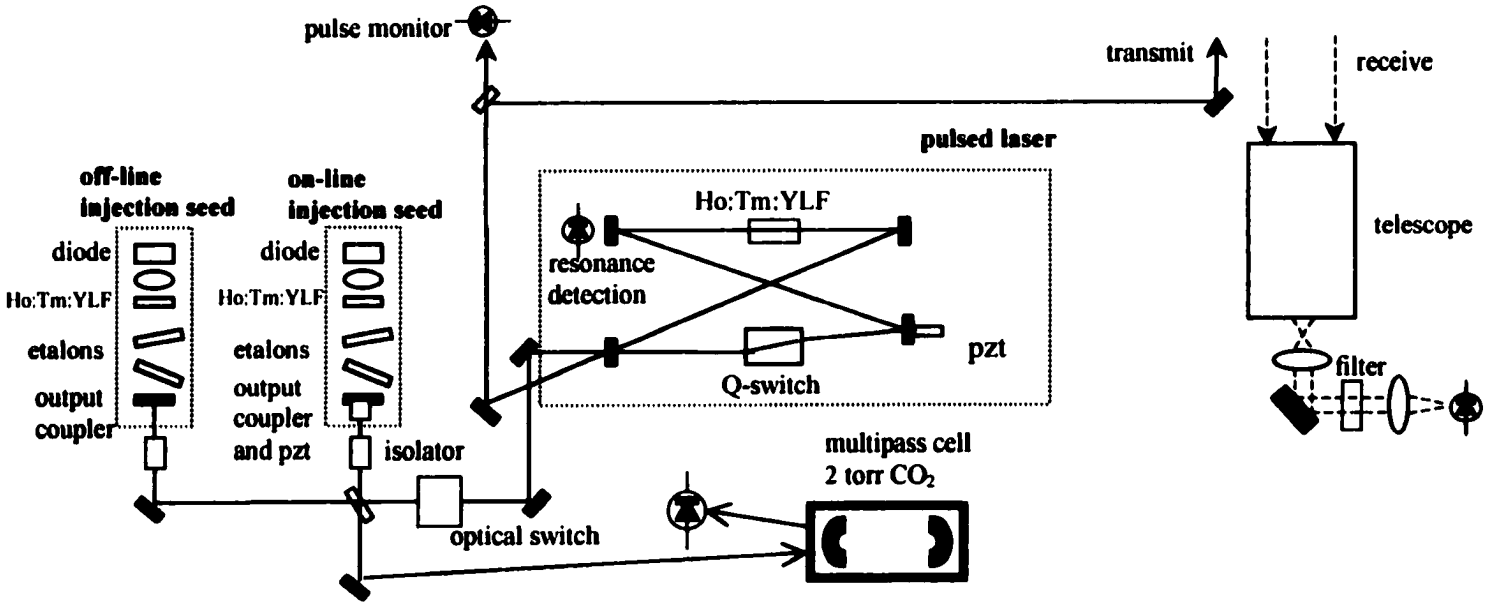

Figure 8.3: Layout of direct-detection design for DIAL of carbon dioxide.

commonly used for astronomical observation. The light collected by the telescope is collimated for transmission through an interference filter that only passes a few nanometers of light centered around the wavelength of interest. Such filtering is required to keep ambient or reflected sunlight from overwhelming the signals of interest. An optical filter is not required in a coherent receiver, as the synchronous detection acts an exceptionally narrow filter. The final component of the direct-detection receiver is a photodiode which detects light focused after the interference filter. This photodiode is an InGaAsP PIN similar to the device used for coherent detection, except with a larger surface area and cooled to -20° C to minimize noise.

BIBLIOGRAPHY

1. R.M. Measures, *Laser Remote Sensing* (Wiley-Interscience, New York, 1984).
2. G.J. Koch, B.C. Barker, and C.L. Britt, "Development of an operational wake vortex sensor based on pulsed coherent lidar," in *Ninth Biennial Coherent Laser Radar Technologies and Applications Conference* (Swedish Defense Research Institute, Linkoping, Sweden, 1997), pp. 194-197.
3. P. Brockman, B.C. Barker, G.J. Koch, D.P.C. Nguyen, and C.L. Britt, "Coherent pulsed lidar sensing of wake vortex position and strength, winds and turbulence in airport terminal areas," in *Tenth Biennial Coherent Laser Radar Technologies and Applications Conference* (Universities Space Research Association, Huntsville, Ala., 1999), pp. 12-15.
4. S.M. Hannon, H.R. Bagley, S.C. Soreide, D.A. Bowdle, R.K. Bogue, and L.J. Ehrenberger, "Airborne turbulence detection and warning: ACLAIM flight test results," in *Tenth Biennial Coherent Laser Radar Technologies and Applications Conference* (Universities Space Research Association, Huntsville, Ala., 1999), pp. 20-23.
5. R. Targ, B.C. Steakley, J.G. Hawley, L.L. Ames, P. Forney, D. Swanson, R. Stone, R.G. Otto, V. Zarifis, P. Brockman, R.S. Calloway, S.H. Klein, and P.A. Robinson, "Coherent lidar airborne wind sensor II: flight test results at 2 and 10 μm," Appl. Opt. **35**, 7117-7127 (1996).
6. R.D. Richmond, P.D. Woodworth, R. Fetner, J.A. Overbeck, M. Salisbury, S.W. Henderson, S.M. Hannon, and S.R. Vetorino, "Eye-Safe Solid State Ladar for Airborne Wind Profiling," in *Eighth Biennial Coherent Laser Radar Technologies and Applications Conference* (Optical Society of America, 1995 Technical Digest 19), pp. 138-141.
7. W.E. Baker, G.D. Emmitt, P. Robertson, R.M. Atlas, J.E. Molinari, D.A. Bowdle, J. Paegle, R.M. Hardesty, R.T. Menzies, T.N. Krishnamurti, R.A. Brown, M.J. Post, J.R. Anderson, A.C. Lorenc, T.L. Miller, and J. McElroy, "Lidar-Measured Winds from Space: A Key Component for Weather and Climate Prediction," Bull. Amer. Meteor. Soc. **76**, 869-888 (1995).
8. G.D. Emmitt, M. Kavaya, T. Miller, "SPARCLE: A Mission Overview," in *Tenth Biennial Coherent Laser Radar Technologies and Applications Conference* (Universities Space Research Association, Huntsville, Ala., 1999), pp. 88-93.
9. G.J. Koch, R.E. Davis, A.N. Dharamsi, M. Petros, and J.C. McCarthy, "Differential absorption measurements of atmospheric water vapor with a coherent lidar at 2050.532 nm," in *Tenth Biennial Coherent Laser Radar Technologies and Applications Conference* (Universities Space Research Association, Huntsville, Ala., 1999), pp. 68-71.
10. M.J. Kavaya, S.W. Henderson, E.C. Russell, R.M. Huffaker, and R.G. Frehlich, "Monte Carlo computer simulations of ground-based and space-based coherent DIAL water vapor profiling," Appl. Opt. **28**, 840-851 (1989).
11. C.J. Grund, R.M. Hardesty, and B.J. Rye, "Feasibility of tropospheric water vapor profiling using infrared heterodyne differential absorption lidar," DOE report DE-A103-94ER61761, 1995.
12. R.M Hardesty, "Coherent DIAL measurement of range-resolved water vapor concentration," Appl. Opt. **23**, 2545-2553 (1984).

13. W.A. Brewer, V. Wulfmeyer, R.M. Hardesty, and B.J. Rye, "Combined wind and water vapor measurements using the NOAA and mini-MOPA Doppler lidar," in *Nineteenth International Laser Radar Conference*, NASA/CP-1998-207671 (available from NASA Center for Aerospace Information, University of Nebraska, Omaha, Neb., 1998), pp. 565-568.
14. American National Standard Z136.1-1993.
15. S. Lehman, H. Linne, and J. Bosenberg, "Simultaneous measurement of wind speed and water vapor with a heterodyne DIAL System," *in 20th Internation Laser Radar Conference* (Institut Pierre Simon Laplace, Vichy, France, 2000).
16. R.P. Wayne, *Chemistry of Atmospheres* (
17. U.S. Weather Bureau, *Radiosonde Observation*, Federal Meteorological Handbook #3 (U.S. Dept of Commerce, U.S. Dept. of Defense, 1969).
18. W.P. Menzel (Editor), "1st International TOVS Study Conference," Igls, Autria (1983).
19. H.D. Chang, P.H. Hwang, T.T. Wilheit, and T.C. Chang, "Monthly distributions of precipitable water from Nimbus 7 SMMR data," J. Geophys. Res. **89**, 5328-5334 (1984).
20. S. Ismail and E.V. Browell, "Airborne and Spaceborne Lidar Measurements of Water Vapor Profiles: A Sensitivity Analysis, Appl. Opt. **28**, 3603-3615 (1989).
21. S.A. Vay, B.E. Anderson, T.J. Conway, G.W. Sachse, and J.E. Collins, "Airborne observations of the tropospheric CO_2 distributions and its controlling factors over the South Pacific basin, J. Geophys. Res. **104**, 5663-5676 (1999).
22. Z. Sorbjan, *Structure of the Atmospheric Boundary Layer* (Prentice Hall, Englewood Cliffs, New Jersey, 1989).
23. R.G. Frehlich, "Effects of refractive turbulence on coherent laser radar, "Appl. Opt. **32**, 2122-2131 (1993).
24. US Committee on Extension to the Standard Atmosphere, *US Standard Atmosphere 1976* (available from US Govt. Print. Off., Washington, DC)
25. L.S. Rothman, USF HITRAN-PC, Version 2.51 (Ontar Corporation, North Andover, Mass., 1996).
26. N.P. Barnes and J.C. Barnes, "Injection Seeding I: Theory, IEEE J. Quant. Elect. **29**, 2670-2683 (1993)."
27. S.W. Henderson, E.H. Yuen, and E.S. Fry, "Fast resonance detection technique for single-frequency operation of injection seeded Nd:YAG lasers," Opt. Lett. **11**, 715-717 (1986).
28. L.F. Johnson, G.D. Boyd, and K. Nassau, (1962), Proc. IRE, 50, 86.
29. R.L. Remski, L.T. James, K.H. Gooen, B. Bartolo, A. Linz, "Pulsed Laser Action in $LiYF_4:Er^{3+}$, Ho^{3+} at 77K," IEEE J. Quant. Elect. **QE-5**, (1969).
30. E.P. Chicklis, C.S. Naiman, R.C. Folweiler, D.R. Gabbe, H.P. Jenssen, and A. Linz,"High Efficiency Room-Temperature 2.06 μm Laser Using Sensitized Ho :YLF," Appl. Opt. **19**, 119-121 (1971).
31. H. Hemmati, "2.07 μm cw diode pumped Tm, Ho:YliF4 room temperature laser," Opt. Lett. **14**, 435-437 (1989).
32. T.M. Taczak and D.K. Killinger, "Development of a tunable, narrow-linewidth, cw 2.066-μm Ho:YLF laser for remote sensing of atmospheric CO_2 and H_2O," Appl. Opt. **37**, 8460-8576 (1998).

33. G.J. Koch, J.P. Deyst, and M.P. Storm, "Single-frequency lasing of monolithic Ho,Tm:YLF," Opt. Lett. **18**, 1235-1237 (1993).
34. C.P. Hale, S.W. Henderson, and D.M. D'Epagnier, "Tunable highly-stable master/local oscillator for coherent lidar applications," *in Tenth Biennial Coherent Laser Radar Technology and Applications Conference* (Universities Space Research Association, Huntsville, Ala, 1999), pp. 115-118.
35. B.T. McGuckin, R.T. Menzies, and C. Esporles, "Tunable frequency stabilized diode-laser-pumped Tm,Ho:$YLiF_4$ laser at room temperature," Appl. Opt. **32**, 2082-2084 (1993).
36. J.D. Kmetec, T.S. Kubo, T.J. Kane, and C.J. Grund, "Laser performance of diode-pumped thulium-doped $Y_3Al_5O_{12}$, $(Y,Lu)_3Al_5O_{12}$, and $Lu_3Al_5O_{12}$ crystals," Opt. Lett. **19**, 186-189 (1994).
37. N.P. Barnes, M.G. Jani, and R.L. Hutcheson, "Diode-pumped, room temperature Tm:LuAG laser," Appl. Opt. **34**, 4290-4294 (1995).
38. A.A. Kaminskii, *Laser Crystals* (Springer-Verlag, Berlin, 1990).
39. L.B. Shaw, "Single Crystal Growth of Rare Earth Doped Lithium Fluoride by the Laser Heated Pedestal Growth Method," Master's Thesis, University of South Florida, Tampa, FL (1990).
40. S.M. Sze, *VLSI Technology* (McGraw Hill, New York, 1988).
41. M. Bass (editor), "Chapter 3: Properties of Crystals and Glasses," in *Handbook of Optics Volume II* (McGraw-Hill, Inc., New York, 1995).
42. N.P. Barnes, "A review of tuning and performance of Ho lasers," Recent Res. Devel. In Applied Optics **1**, 47-58 (1996).
43. M. Ashurov, K. Yu, E. Zhorikov, A.A. Kaminskii, U.U. Osiko, A.A. Sobol, M.I. Timosheechikin, V.A. Federov, and A.A. Subaltai, "Structure, Spectroscopy, and Stimulated Emission of Crystals of Yttrium Holmium Aluminum Garnet," Appl. Spectr. 15, 979-983 (1979).
44. A.E. Siegman, *Lasers* (University Science Books, Mill Valley, CA, 1986).
45. J.T. Verdeyen, *Laser Electronics* (Prentice Hall, Englewood Cliffs, New Jersey, 1989).
46. I.G. Podkolzina, A.M. Tkachuk, V.A. Fedorov, and P.P. Feofilov, "Multifrequency Generation of Stimulated Emission of Ho^{3+} ion in $LiYF_4$ Crystals," Opt. Spectrosc. **40**, 111-112 (1976).
47. J.T. Murray and L.K Calmes, *Lasica 1.0* (University of Arizona, 1997).
48. N.P. Barnes, E.D. Filer, C.A. Morrison, and C.J. Lee, "Ho:Tm Lasers I: Theoretical," IEEE J. Quant. Elect. **32**, 104-111 (1996).
49. M.E. Storm, "Holmium YLF amplifier performance and the prospects for multi-joule energies using diode-laser pumping," IEEE J. Quant. Elect. 29, 440-451 (1993).
50. A.N. Dharamsi, "A theory of modulation spectroscopy with applications of higher harmonic detection," J. Phys. D **29**, 540-549 (1996).
51. W. Lenth, IEEE J. Quant. Elect. **20**, 1045- (1984)
52. O.E. Meyers and E.J. Putzer, J. Appl. Phys. 29, 540-549 (1966).
53. J. Reid and D. Labrie, "Second-Harmonic Detection with Tunable Diode Lasers—Comparison of Experiment and Theory," Appl. Phys. B **26**, 203-210 (1981).
54. J.N. Dodd, *Atoms and Light* (Plenum Press, New York, 1991).

55. A.M. Bullock, J.M. Barrington, C.M. Fitzgerald, B. Seavey, and A.N. Dharamsi, "Wavelengt modulation of semiconductor lasers for absorption spectroscopy employing harmonic detection," SPIE Vol. 3945, 133-141 (2000).
56. F.W. Cotton, *Chemical Applications of Group Theory* (Wiley Interscience, New York, 1971).
57. G. Herzberg, *Electronic Spectra of Polyatomic Molecules* (D. Van Nostrand Company, Princeton, New Jersey, 1966).
58. G. Herzberg, *Molecular Spectra and Molecular Structure* (Krieger Publishing, Malabar, Florida, 1988).
59. G.J. Koch, A.L. Cook, C.M. Fitzgerald, and A.N. Dharamsi, "Frequency stabilization of a diode laser to absorption lines of water vapor in the 944-nm wavelength region," Opt. Lett. **40, 525-528** (2001).
60. T. Ikegami, S. Sudo, and Y. Sakai, *Frequency Stabilization of Semiconductor Laser Didoes* (Artech House, Norwood, Mass., 1995).
61. A. Arie, M.L. Bortz, M.M. Fejer, and R.L. Beyer, "Iodine spectroscope and absolute frequency stabilization with the second harmonic of the 1319-nm Nd:YAG lase," Opt. Lett. **18**, 1757-1759 (1993).
62. P. Laporta, S. Taccheo, S. Longhi, C. Svelto, and P. DeNatale, "Frequency locking of tunable Er:Yb microlasers to absorption lines of $^{13}C_2H_2$ in the 1540-1550 nm wavelength interval," Appl. Phys. Lett. **71**, 2271-2733 (1997).
63. G.J. Koch, A.N. Dharamsi, C.M. Fitzgerald, and J.C. McCarthy, "Frequency stabilization of a Ho:Tm:YLF laser to absorption lines of carbon dioxide," Appl. Opt. **39**, 3664-3669 (2000).
64. C.M. Fitzgerald, "Wavelength Modulation Spectroscopy of Water Vapor and Line Center Stabilization at 1.462 μm for Lidar Applications," Master's Thesis, Old Dominion University, 2000.
65. J.L. Lachambre, P. Lavigne, G. Otis, and M. Noel, "Injection locking and mode selection in TEA-CO_2 laser oscillators," IEEE J. Quant. Elect. **12**, 756-764 (1976).
66. J.C. Barnes, N.P. Barnes, L.G. Wang, and W.C. Edwards, "Injection Seeding II: $TiAl_2O_3$ Experiments," IEEE J. Quant. Elect. **29**, 2684-2692 (1993).
67. J. Yu, U.N. Singh, N.P. Barnes, and M. Petros, "125-mJ diode-pumped injection-seeded Ho:Tm:YLF laser," Opt. Lett. **23**, 780-782 (1998).
68. R. Targ, M.J. Kavaya, R.M. Huffaker, and R.L. Bowles, "Coherent lidar airborne windshear sensor: performance evaluation," Appl. Opt. **30**, 2013-2026 (1991).
69. J. Yu, M. Petros, U.N. Singh, J.C. Barnes, and N.P. Barnes, "An Efficient Double Pulsed 2-micron Laser for DIAL Applications," *in 20th Internation Laser Radar Conference* (Institut Pierre Simon Laplace, Vichy, France, 2000).
70. www.conoptics.com
71. www.quantumtech.com
72. www.nmlaser.com
73. R.E. Davis, G.J. Koch, N.P. Barnes, and W.F. Wood, "Optimum H_2O Absorption Lines in the 1.85 to 2.15-μm Spectral Region for DIAL Use at Sea Level Over a Range of Cllimatic Conditions," in preparation, NASA Langley Research Center, 2001.

CURRICULUM VITA
for
GRADY JAMES KOCH

DEGREES:

Doctor of Philosophy (Electrical and Computer Engineering), Old Dominion University, Norfolk, Virginia, May 2001

Master of Science (Electrical and Computer Engineering), University of Illinois at Urbana-Champaign, Urbana, Illinois, January 1995

Bachelor of Science (Electrical Engineering), Virginia Polytechnic Institute and State University, Blacksburg, Virginia, May 1991

PROFESSIONAL CHRONOLOGY:

Laser Systems Branch, NASA Langley Research Center,
Hampton, Virginia
Engineer, June 1991 – Present

NASA Langley Research Center,
Hampton, Virginia
Cooperative Education Student, November 1987 – May 1991

SCIENTIFIC AND PROFESSIONAL SOCIETIES MEMBERSHIP:

Tau Beta Pi (National Engineering Honor Society)
Eta Kappa Nu (Electrical Engineering Honor Society)

HONORS AND AWARDS:

NASA Innovation Award (2000)
NASA Superior Accomplishment Award (1994, 1995, 2000)
NASA Group Achievement Award (1999, 2000)

SCHOLARLY ACTIVITIES COMPLETED:

1. "Frequency Stabilization of a Diode Laser to Absorption Lines of Water Vapor in the 944 nm Wavelength Region," G.J. Koch, A.L. Cook, C.M. Fitzgerald, and A.N. Dharamsi, Opt. Eng. **40**, 525-528 (2001).

2. "Multifunction Lidar: Measurement of Wind, Water Vapor, and Aerosols with an Eye-Safe Coherent Lidar," G.J. Koch, R.E. Davis, C.M. Fitzgerald, A.N. Dharamsi, and M. Petros, 20th International Laser Radar Conference, Vichy, France, July 2000.

3. "Frequency Stabilization of a Ho:Tm:YLF Laser to Absorption Lines of Carbon Dioxide," G.J. Koch, A.N. Dharamsi, C.M. Fitzgerald, and J.C. McCarthy, Appl. Opt. **39**, 3664-3669 (2000).

4. "Wavelength Modulation Spectroscopy of Water Vapor and Laser Line Center Stabilization at 1.462 μm for Lidar Applications," C. Fitzgerald, G. Koch, A. Bullock, and A. Dharamsi, SPIE Conference on Laser Diodes in Industrial Measurement, Imaging, and Sensors Applications, San Jose, CA, January 2000.

5. "Differential Absorption Measurements of Atmospheric Water Vapor with a Coherent Lidar at 2050.532 nm," G.J. Koch, R.E. Davis, A. Dharamsi, M. Petros, and J.C. McCarthy, 10th Conference on Coherent Laser Radar, Mt. Hood, OR, June 1999.

6. "Coherent Pulsed Lidar Sensing of Wake Vortex Position and Strength, Winds and Turbulence in the Terminal Area," (invited) P. Brockman, B.C. Barker, G.J. Koch, D.P.C. Nguyen, C.L. Britt, and M. Petros, 10th Conference on Coherent Laser Radar, Mt. Hood, OR, June 1999.

7. "Pulsed Lidar Measurements of Aircraft Wake Vortices at DFW and JFK," C.L. Britt, D.P.C. Nguyen, and G.J. Koch, AIAA Aviation Environment Conference, Reno, NV, January 1999.

8. "A Simple Overhead Denisyuk Configuration for Making Reflection Holograms with a Diode Laser," G.J. Koch and M. Petros, Am. J. Phys. **66** (10), 933-934 (1998).

9. "An Operational Wake Vortex Sensor Using Pulsed Coherent Lidar," B.C. Barker, Jr., G.J. Koch, and D.C. Nguyen, 19th International Laser Radar Conference, Annapolis, MD, July 1998.

10. "Development of an Operational Wake Vortex Sensor Based on Pulsed Coherent Lidar," 9th Conference on Coherent Laser Radar, G.J. Koch, B.C. Barker, and C.L. Britt, Linkoping, Sweden, June 1997.

11. "A 1000 Hz Pulsed Solid-State Raman Laser for Coherent Lidar Measurement of Wake Vortices," G.J. Koch, J.C. Murray, C.D. Lytle, and C. Nguyen, NASA's First Wake Vortex Dynamic Spacing Workshop, Hampton, VA, May 1997.

12. "Laser Radar Watches the Friendly Skies," B.C. Barker, P. Brockman, and G.J. Koch, Photonics Spectra, Laurin Publications, 94-98, April 1997.

13. "Design Considerations for an Operational Wake Vortex Lidar Sensor," G.J. Koch, L.D. Staton, and D.P.C. Nguyen, 8th Conference on Coherent Laser Radar, Keystone, CO, June 1995.

14. "Atmospheric Thermal Lensing in Laser Resonators," N.P. Barnes, M.E. Thomas, G.J. Koch, and W.D. Marsh, IEEE J. Quant. Elect. **31**, 962-969 (1995).

15. "Tunable Multiple Wavelength External Cavity Diode Lasers for Remote Sensing Applications," G.C. Papen, G.M. Murphy, G.J. Koch, R.Y. Dejule, and R.W. Kaliski, Laser Radar VI Conference, 1994.

16. "Evaluation of an external-cavity diode laser as an injection seed source," G.J. Koch and G.C. Papen, OSA Annual Meeting, Toronto, Canada, October 1993.

17. "Single-frequency lasing of monolithic Ho,Tm:YLF," G.J. Koch, J.P. Deyst, and M.E. Storm, Opt. Let. **18**, 1235-1237 (1993).

18. "Diode-pumped single-frequency Ho:Tm:YLF," J.P. Deyst, G.J. Koch, and M.E. Storm, Conference on Advanced Solid-State Lasers, Memphis, TN, 1993.

19. "Single-Mode Lasing of Ho:Tm:YAG at 2.091 μm in a Monolithic Crystal," M.E. Storm, G.J. Koch, and W.W. Rohrbach, Conference on Advanced Solid-State Lasers, 1991.